ISSN 1451 - 9372(Print)
ISSN 2217 - 7434(Online)
OCTOBER-DECEMBER 2022
Vol.28, Number 4, 255-343

Chemical Industry & Chemical Engineering Quarterly

The AChE Journal for Chemical Engineering,
Biochemical Engineering, Chemical Technology,
New Materials, Renewable Energy and Chemistry
www.ache.org.rs/ciceq

Journal of the
Association of Chemical Engineers of
Serbia, Belgrade, Serbia

Chemical Industry & Chemical Engineering
CI&CEQuarterly

Journal of the
Association of Chemical Engineers of
Serbia, Belgrade, Serbia

Chemical Industry & Chemical Engineering Quarterly

Vol. 28 | Belgrade, October-December 2022 | No. 4

Chemical Industry & Chemical Engineering Quarterly (ISSN 1451-9372) is published quarterly by the Association of Chemical Engineers of Serbia, Kneza Miloša 9/I, 11000 Belgrade, Serbia

Editor:
Vlada B. Veljković
veljkovic@yahoo.com

Editorial Office:
Kneza Miloša 9/I, 11000 Belgrade, Serbia
Phone/Fax: +381 (0)11 3240 018
E-mail: shi@yubc.net
www.ache.org.rs

For publisher:
Ivana T. Drvenica

Secretary of the Editorial Office:
Slavica Desnica

Marketing and advertising:
AChE Marketing Office
Kneza Miloša 9/I, 11000 Belgrade, Serbia
Phone/Fax: +381 (0)11 3240 018

Publication of this Journal is supported by the Ministry of Education, Science and Technological Development of the Republic of Serbia

Subscription and advertisements make payable to the account of the Association of Chemical Engineers of Serbia, Belgrade, No. 205-2172-71, Komercijalna banka a.d., Beograd

Computer typeface and paging:
Marija Tasić

Printed by:
Faculty of Technology and Metallurgy, Research and Development Centre of Printing Technology, Karnegijeva 4, P.O. Box 3503, 11120 Belgrade, Serbia

Abstracting/Indexing:
Articles published in this Journal are indexed in *Thompson Reuters* products: *Science Citation Index - Expanded*™ - access *via Web of Science*®, part of *ISI Web of Knowledge*℠

CONTENTS

Activities of the Association of Chemical Engineers of Serbia are supported by:

- Ministry of Education, Science and Technological Development, Republic of Serbia
- Hemofarm Koncern AD, Vršac, Serbia
- Faculty of Technology and Metallurgy, University of Belgrade, Belgrade, Serbia
- Faculty of Technology, University of Novi Sad, Novi Sad, Serbia
- Faculty of Technology, University of Niš, Leskovac, Serbia
- Institute of Chemistry, Technology and Metallurgy, University of Belgrade, Belgrade, Serbia

CI&CEQ
Chemical Industry & Chemical Engineering Quarterly

Available online at
Association of the Chemical Engineers of Serbia AChE
www.ache.org.rs/CICEQ

Chem. Ind. Chem. Eng. Q. 28 (4) 255–264 (2022) CI&CEQ

VELIZAR STANKOVIĆ[1]
MILAN GORGIEVSKI[1]
DRAGANA BOŽIĆ[2]
GROZDANKA D. BOGDANOVIĆ[1]

[1]University of Belgrade
Technical Faculty in Bor, Serbia

[2]Mining and Metallurgy
Institute Bor, Serbia

MINE WATERS PURIFICATION BY BIOSORPTION COUPLED WITH GREEN ENERGY PRODUCTION FROM WOOD AND STRAW BIOMASS

Article Highlights

- A new process for metal ions removal and recovery from mine waters has been proposed
- The process encompasses heavy metal ions biosorption and green energy production
- The biosorption is performed as two-staged, with cross-flowing of the phases
- Energy production comprises a cogenerative way of burning the loaded biosorbent
- The costs and revenues analysis showed the process's economic sustainability

Abstract

A new process for mine water purification has been proposed, based on biosorption followed by burning the loaded biosorbents. Wheat straw and sawdust of trees are convenient as biosorbents in the proposed process. Biosorption was performed in two stages: a cross-flow regime between the mine water and the biosorbent. The achieved copper adsorption degree was > 95%. Based on the mine water volume and its chemical composition, the estimated amount of the biosorbent was 60.000 t/year. The cogenerative mode of the loaded biosorbent combustion was considered for green energy production. For the recovery of metals concentrated in the ash, they must be processed separately. Several possibilities for ash processing were proposed and discussed. For an annual volume of mine water and the copper content in it, the mass and energy balances of the process were estimated, giving some economic data on the process efficiency. The analysis of the revenues and costs, based only on the energy value produced by the combustion of the biosorbent, has shown that the process can economically be viable regardless of the value of the recovered metal.

Keywords: biosorption, biomass combustion, green energy, heavy metal ions, mine water.

SCIENTIFIC PAPER

UDC 66.067.8.081.3:546.3:662

Metal or coal mines, active or closed, generate larger or smaller amounts of mining water contaminated with soluble organic or inorganic compounds extracted from ore residues, seriously endangering the local environment. In this sense, the waters from heavy metal mines, known as acid mine drainage (AMD), which contain numerous ionic species, are particularly harmful to surface waters, soil, and wildlife near mines [1–5], which is a great concern for mining owners, and communities near the mining area. Therefore, it is imperative to purify AMDs, which may be the cost for both parties.

The process of mine water generation is complex, involving simultaneous chemical, biochemical, and electrochemical reactions, occurring spontaneously in the presence of sulfide minerals, oxygen, water, and bacteria. The sulfide mineral oxidation processes are well described in the relevant literature [1,6-9] and will not be considered here.

Mine water treatment involves various ion separation and concentration techniques existing on an industrial level for a long time [5,6,8,10–13]. However, each possesses a limited ability of metal ion removal from solutions, as illustrated in Figure 1.

Correspondence: V. Stanković, University of Belgrade Technical Faculty in Bor, Vojske Jugoslavije 12, Bor, Serbia.
E-mail: stankovic.velizar@gmail.com
Paper received: 17 June, 2021
Paper revised: 13 December, 2021
Paper accepted: 18 December, 2021

https://doi.org/10.2298/ciceq210617037s

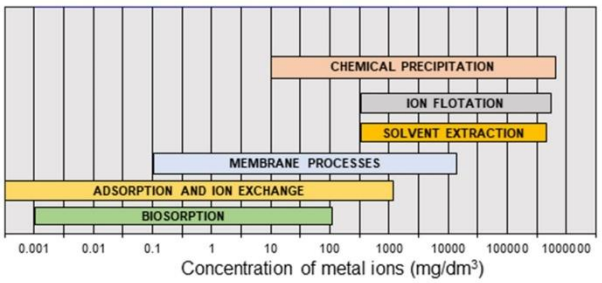

Figure 1. The capability of some methods for metal ions removal from solutions.

Ion adsorption is much more efficient than the other techniques since it can reduce the metal ion concentration well below 1 ppm. On the other hand, biosorption is an emerging version of adsorption that uses natural adsorbents (biosorbents) - a technique not developed on an industrial scale yet, which has shown to be an efficient way of purifying wastewater from metal ions [12,14–17 and literature cited therein]. Various combinations of biosorbents and metal ions were tested through laboratory experiments to determine the adsorption capacity and parameters affecting it; adsorption kinetics and equilibrium. By-products from agriculture and forestry, which show moderate adsorption capacity, have been most frequently tested as biosorbents. Also, their massive production and easy availability make them a good potential for biosorbents. Besides, some of these products are already used as biomass in green energy production [18–22,26,27]. However, despite numerous published papers on biosorption, there is no clear answer to what to do with the loaded biosorbent. Namely, biosorbents change their characteristics after a few adsorption-desorption cycles due to deterioration of their structure, resulting in a reduction of the adsorption capacity, which is a serious drawback of using them on an industrial scale [12,19,22].

Searching for ways to perform metal ions biosorption by omitting desorption, which usually comes after adsorption in conventional processes, led to integrating the two processes – metal ion biosorption from mine waters and green energy production by burning biomass. In this way, three goals would be achieved:

- Mine waters will be purified through adsorption of metal ions from it;
- The charged biosorbent will be burned for energy production without excess CO_2 emission - green energy;
- The adsorbed metals concentrated in the ash will be further processed for metal recovery, thus contributing to a better process economy.

The idea has already been proven on a laboratory scale [12]. The obtained results were encouraging for taking a step towards establishing a process on an industrial scale. That would encompass the following:

- Flowsheet of the copper adsorption process from real mine water;
- Energy and mass balancing;
- Definition of the basic technology units;
- Consideration of the main economic and environmental parameters of the process sustainability.

Mine waters from copper mines, as the aqueous phase, and biomass (either wheat straw or forestry felling), as biosorbent, should serve as a model system in this study.

COPPER IONS BIOSORPTION FOLLOWED BY COMBUSTION OF THE LOADED BIOSORBENT FOR ENERGY PRODUCTION, AND COPPER RECOVERY

Technological aspects of the process

The flow diagram of the newly-proposed process is schematically presented in Figure 2. The process itself consists of four units: the AMDs capturing, collecting, clarifying, and feeding mixture equalizing; preliminary biomass treatment; biosorption and the loaded biomass combustion, the energy production, and the ash treatment; post-treatment of depleted mine water before being discharged into the environment.

Capturing and collecting the AMDs

According to Figure 2, the first operation is to capture all mine water springs and their collection in a collecting pond for equalization. Collecting the AMDs is an engineering issue, which should provide constant initial parameters of the mine water mixture in the collecting pond (chemical composition, flow rate, clarity, and others) entering, as a feeding stream, into the biosorption operation unit. It comprises the design, equipment choice, and provisional costs estimation for capturing the AMD sources, pumping stations, and pipelines for mine water transport to the collecting pond. Eq. (1) can estimate copper concentration in the mixture:

$$C = \frac{1}{Q}\sum_{i=1}^{n} Q_i C_i \qquad (1)$$

where: C, C_i (g/m^3) - metal ion concentration in the mixture and each AMD, respectively, Q and Q_i – total flow rate and flow rate (m^3/h) of each AMD spring, respectively.

Mine waters considered in this study originate from

four AMDs of the two copper mines located close to each other [1]. An approximative chemical composition, annual volume V_m (m^3/year), and copper quantity of the mine waters mixture, G_{Cu}, (t/year), are evaluated from the individual characteristics of the AMDs, by using Eq. (1) and presented in Table 1. The main expected constituents in the feeding mixture are Cu^{2+}, Fe^{2+}/Fe^{3+} ions and H_2SO_4 (pH = 3 to 5). The concentration of other metal ions is much lower and will not affect the biosorption of copper ions. Since an optimal pH value for copper biosorption is about 4.5 to 5 [14,16], adjusting the pH to the required value, if it is necessary, can be done with a solution of lime or caustic soda.

Due to the neutralization reaction, fine solid parti-

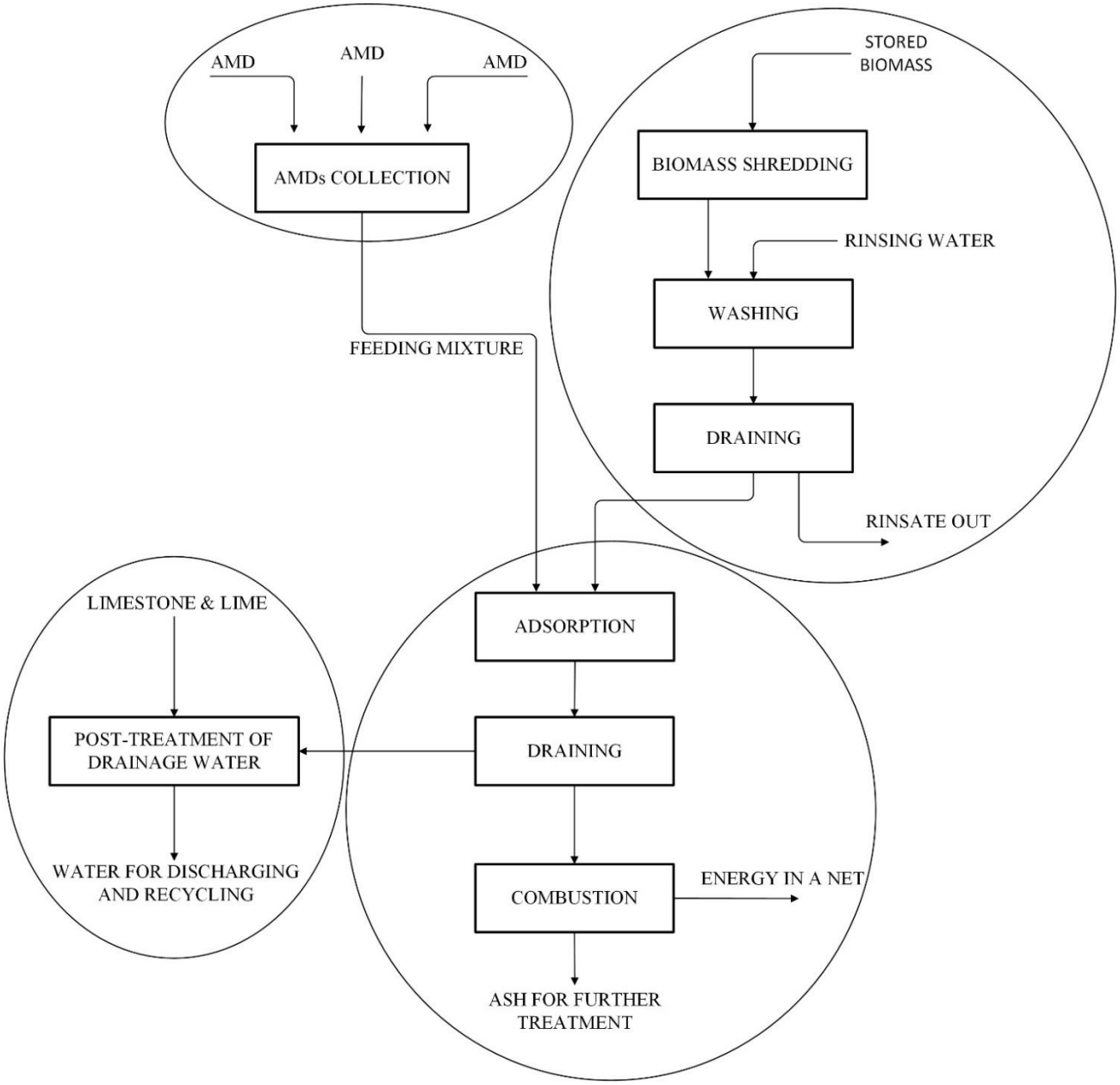

Figure 2. Flowsheet of the process for copper recovery from mine waters by biosorption.

Table 1. Mean values of ion concentration, volume, and copper quantity in the mine water

C_{Cu},mg/dm^3	C_{Fe}, mg/dm^3	C_{Zn}, mg/dm^3	C_{Mn}, mg/dm^3	V_m, m^3/year	G_{Cu}, t/year	pH
93	150	7	<10	2,460.000	222	3 to 5

cles of $Fe(OH)_3$ and $CaSO_4 \cdot 2H_2O$ will be formed in the feeding mixture. Its efficient clarification in the collecting pond is crucial to get a minimum concentration of particles entering the biosorption unit in the mixture. The clarified feeding mixture from the collecting pond enters the biosorption column to contact the biosorbent. Mean residence time between phases must be long enough to achieve an outlet concentration of Cu^{2+} close to equilibrium. Water, depleted in metal ions, leaves the adsorption unit and enters the post-treatment unit, consisting of a pond and a reactive limestone barrier, to neutralize the acid and the remaining metal ions (passive treatment). The purified mine water must fulfill a required quality for being discharged into the nearest watercourse, while the pond size, settling surface, and water hold-up must meet these requests.

Biomass movement through the process

Whether the biosorption will be performed either in a batch stirring tank or a fixed bed adsorption column, stored biomass must be shredded and sieved, obtaining an optimal sieve fraction of 5 to 10 mm. The uniform size of biomass particles contributes to a better carrying out of the biosorption process [12,22]. It was proven that the particles size of straw or sawdust does not affect the biosorption kinetics or the adsorption capacity [14,16,24].

The preparation of the biosorbent comprises washing to remove small particles of dirtiness and leach partly out alkali and alkaline earth metals from it. After drainage and drying, it enters the adsorption unit. The leaching of alkalies refers mainly to straw containing a significantly higher concentration of alkalies than wood residues [22,23]. Besides, the adsorption capacity will be increased by washing approximately 25 to 30% [16,24,25].

The biosorbent, loaded with the adsorbed metal ions, will be separated from the aqueous phase and dried, reaching a natural humidity of 10 to 15% before combustion. The off-gases pass through the heat exchanger, through the gas dedusting unit, before being discharged into the atmosphere. The combustion unit may operate as a heat generation or as a cogeneration unit, in which case the produced electricity will be delivered to a net. Finally, the ash will be disposed of for cooling, further processing, and metal recovery.

MASS AND HEAT BALANCE OF THE PROCESS

Mass balance of metal ions to be adsorbed

Here, the mass balance will relate only to copper ions as the most represented and most valuable ionic specie, which is transferred from the aqueous to the biosorbent phase. Since other ions, such as Zn^{2+} and Mn^{2+}, have a much lower concentration in the feeding mixture and a lower selectivity coefficient, they will be co-adsorbed with copper in a negligible amount. The latter especially relates to Mn^{2+}, which has the smallest selectivity coefficient. Therefore, the adsorption of Fe^{2+}/Fe^{3+}, having the smallest affinity to be adsorbed, can also be considered negligible [12,14,16].

Assuming the process, presented schematically in Figure 2, should work 330 days a year, the flow rate Q, based on data from Table 1, will be:

$$Q = V_m / 330 \cdot 24 \cdot 60 \; m^3/min = 5.18 \; m^3/min \quad Q \approx 5.2 \; m^3/min \tag{2}$$

According to data from Table 1, the copper mass flow G is:

$$G = Q \cdot C_{in} = 0.483 \; kg/min \tag{3}$$

Assuming that the adsorption efficiency in the adsorption unit, defined as:

$$\eta \; \% = (1 - C_{out}/C_{in}) \cdot 100 \geq 95\% \tag{4}$$

the outlet copper concentration should be:

$$C_{out} = C_{in}(1 - 0.95) \leq 4.65 \; g/m^3 \tag{5}$$

The outlet concentration of C_{out} < 4.65 g/m^3 of copper ion is low enough and can be treated with limestone in the passive treatment unit. From the total annual copper content $G_{in} \approx 222$ t (See Table 1):

$$G_{ad} = G_{in} \cdot \eta / 100 = 210.9 \approx 211 \; t/year \tag{6}$$

would be recovered, while an outlet amount, G_{out} <11 t, will be treated in the post-treatment stage.

Mass of the required biosorbent for copper biosorption from the mine water mixture

It was shown that the average adsorption capacity of the washed beech sawdust is 7 to 9 mg/g [12,14 and the references cited therein], and for the wheat straw, 6 to 8 mg/g [16 and the references cited therein].

The definition equation of the adsorption capacity is:

$$q_{av} = \Delta C \cdot Q / m \tag{7}$$

where: $\Delta C = (C_{in} - C_{out})$ – is the difference between inlet and outlet concentration from the adsorption process (g/m^3), Q – flow rate of the mine water mixture passing through the adsorption unit (m^3/h), and m – the mass of the biosorbent (kg).

An annual amount of biosorbent m required to remove ≥ 95% of copper ions from the feeding mixture can be evaluated from Eq. (7). By solving Eq. (7), ac-

cording to the unit mass of biosorbent m, and assuming that an average adsorption capacity is q_{av}= 8 mg/g, the annual amount of biosorbent needed for the yearly total volume V_m is obtained:

$$m = \Delta C \cdot V_m / \ q_{av} = \ 27.060 \ t / year \tag{8}$$

The mass of biosorbent m, added in a surplus of 10% and rounded, gives approximately $m \approx$ 30.000 t/year.

Specific biomass consumption per unit of the adsorbed copper will be:

$$m_{sp} = \ m / G_{ad} = \ 142.2 \ t / t_{Cu} \tag{9}$$

Cross-flow mode of biosorption

Adsorption can be performed in a single pass, or with recirculation of the aqueous phase, in a stirred reactor, but most often in a column with a fixed bed of adsorbent – in one stage or as a multi-staged operation with countercurrent or with cross-flow of the contacted phases.

The published papers on the adsorption kinetics in a batch mixing reactor have shown that biosorption follows a pseudo-second-order kinetic model and rapidly occurs in the first 10 min to 30 min of the contact time. By exceeding this rapid initial period, adsorption enters a period where the adsorption capacity changes very slowly, reaching an adsorption degree of about 80% [12,14,16]. Furthermore, numerous researches have shown that the equilibrium state between Cu^{2+}-ions and both here considered biosorbents can be described quite well by the Langmuir adsorption model [12–17,24 and the references cited therein].

The adsorption process should be carried out at least in two steps, schematically presented in Fig. 3, to achieve the adopted copper removal degree > 95%. By performing the biosorption in a single pass of the aqueous phase through the fixed bed column, the biosorbent will be loaded only about 50% with metal ions before the breakthrough point appearance on the S-curve [12, 28–30]. Therefore, the estimated mass of biosorbent should be doubled to 60,000 t/year, regardless of whether a batch mixing reactor or adsorption column is used. For a deeper understanding, it is necessary to optimize the process. The outlet copper concentration can be even less than the one estimated by Eq. (5): < 0.93 mg/dm^3, performing the biosorption in two stages as a cross-flow of the phases.

Heat balance of the burned biosorbents and the energy to be generated

Some physical characteristics of different types of trees and straws, which would serve as biosorbents, are presented in Table 2. For comparison, the corresponding characteristics of heavy oil are shown in the last row.

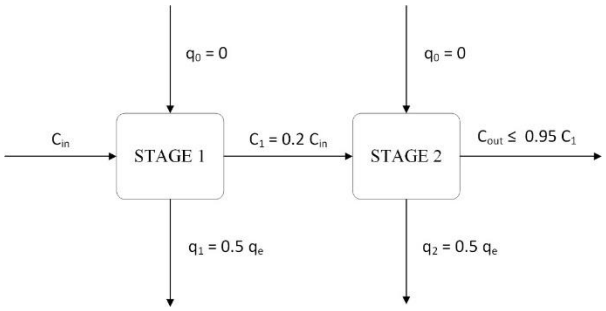

Figure 3. Cross-flow column biosorption of copper ions from mine water mixture.

Table 2. Some physical characteristics of wood and straw biomass

	Moisture, %	Lower heating value, MJ/kg	Ash, %	Remarks
Beech	8 – 22	14.4	0.37	
Oak	13.1	14.1	2	With bark
Poplar	5.5	14.5	< 1	
Felling residue	7–15	15.5	< 1	
Chips	15	15	<1	
Sawdust	5.5–13	17–18.4	<1	
Wheat straw	8.3–14	14	4.5–9	[18, 20]
Barley straw	15	14.2	5–7	
Triticale straw	8–12	15.2	4.6	[31]
Heavy fuel oil	1	min 40	0.2	S < 3 %

Apart from sawdust and triticale straw, the values of lower thermal power (LHV) of other species do not differ significantly and can be considered constant. Oak differs in that it has more than twice the ash content of other deciduous trees. By burning straw, almost 5 to 10 times more ash will be obtained than from the same amount of wood biomass. In this sense, straw biomass seems less suitable as a biosorbent. Based on Table 2, an assumed LHV can be h = 14 to 15 MJ/kg. Combusting the m t/year of the biosorbent, loaded with the adsorbed copper, will generate the energy E:

$$E = h \cdot m = \\ 8.4 \cdot 10^8 MJ / year \ or \ E \approx 23.33 \cdot 10^4 MWh / year \tag{10}$$

The amount of energy E corresponds to an amount of fuel oil of ≈ 21,000 toe/year. According to the average European price, the worth of energy E will exceed many times the value of copper to be recovered, based on the current price at the London Stock Exchange (LSE). Therefore, the cost-effectiveness of the process is based on the cost of energy produced and sold. Thus, the value of the recovered copper will positively affect the economy of the process.

The total input power N_{in}, assuming working time of $\tau \approx 8000$ h/year, is:

$$N_{in} = E / \tau = 29.2\ MW \quad (11)$$

The output power is:

$$N = \eta_{he} \cdot N_{in} = 25.1\ MW \quad (12)$$

where: $\eta_{he} = 0.86$ - plant efficiency for cogeneration of heat and electricity [32].

The output power is a sum of the thermal N_h and electricity N_e power, expressed as:

$$N = N_h + N_e \quad (13)$$

For cogeneration power plants, there is a ratio between thermal and inlet power in a range of $N_h/N_{in} = 0.55$ to 0.7, allowing for the evaluation of the thermal and then electric power [32]. Choosing the ratio value $N_h/N_{in} = 0.62$, it comes out that $N_h = 18.1$ MW. Introducing this value and the value of N in Eq. (13) leads to $N_e = 7$ MW - the power enough for a community of 5 to 8 thousand homes [33]. Therefore, thermal E_h and electrical E_e energy are as follows:

$$E_h = \tau \cdot N_h = 1.45 \cdot 10^5\ MWh / year \quad (14a)$$

$$E_e = \tau \cdot N_e = 5.6 \cdot 10^4\ MWh / year \quad (14b)$$

Produced ash and its processing

Ash amount will depend very much on the burned biomass. Burning 60.000 t/year of felling residue, 220 to 1200 t/year of ash will be produced in extreme cases. By burning wheat straw (see Table 2), the ash mass will be 2 to 24 times greater than that obtained from wood residues. Using blended biomass from wood residues, one can expect < 600 t/year of ash. An amount of copper oxide should be added to this amount, obtained by the oxidation of 211 t/year of the adsorbed copper. It amounts to > 265 t/year or, taking into account oxides of the other adsorbed metals, up to 280 t/year. In total, it amounts to 880—900 t/year of ash. By burning an equal amount of straw, between 2700 and 5400 t/year of ash can be obtained. Adding up the mass of metal oxides, estimated previously, it amounts to about 3000–5700 t/year of ash. Besides the quantity, a kind of biosorbent affects the produced ash quality. An approximate copper concentration in the wood ash will be about 24%, while in the straw ash, the corresponding one is to be 4 to 7%. The smaller amount of ash implies its cheaper storage, transport, and further processing. One more thing, there are fewer technological problems when burning wood than straw [19,22,23].

The ash processing scheme, shown in Figure 4, suggests several ways to produce copper or commercial products based on copper and other metals less represented in it. Based on the mine water quality and volume, it is possible to predict the ash composition and choose an optimal way of its processing.

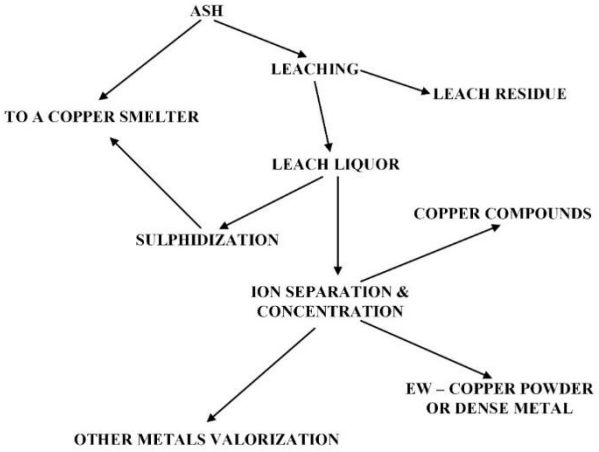

Figure 4. Variants of the ash treatment and metal valorization.

Blending the ash with copper concentrate for charging a copper smelting furnace seems like the shortest and cheapest way for copper recovery as a metal and a way to lose all the other metals in the ash. If there is no copper smelter nearby a copper mine and AMD sources, or if the ash contains other valuable metals in quantities challengeable for recovery, the method of ash processing is leaching and leach liquor processing, as indicated in Figure 4. Such an approach involves a small but complex installation, which could economically be questionable. Because of that, it would be simpler and more cost-effective to sell the ash to a third party that already has a plant for processing similar secondary sources and the market for their products.

ECONOMIC ASPECTS OF THE PROCESS

Biosorbents potential assessment

According to the Ministry of Mining and Energy of Serbia [26], Serbia is a significant producer of various types of biomasses, with a potential of 3.1 Mtoe (expressed as a fuel oil equivalent), having a growing trend. About 1.5 Mtoe is a part of wood biomass from this amount, while 1.6 Mtoe is from agriculture, where

wheat straw and corn stalks make the largest amount. In 2019, for example, wheat straw production was 2.5 Mt. Production of wheat straw in eastern and southeastern Serbia in the same year amounted to 440,000 tons. The price of straw on the market ranges from 30 to 45 €/t. The straw itself participates with less than 30% in that price, while the costs of harvesting, baling, and transport make more than 55%. The rest makes handling and storage. Eastern Serbia has a large forest area, mostly with indigenous deciduous trees. Besides, there are also afforested areas, mainly with acacia and poplar, of which the first one grows well on pyritic substrates near copper mines. Three forest estates from eastern Serbia produce timbers and residues of approximately 124.000 t/year. An approximate price of naturally dried cutting residues (moisture 14%) is c_{bm} = 40 €/t, including transport costs within a radius of 50 km from the place of their production.

To conclude, the annual biomass production from forests and agricultural areas around the copper mines in eastern Serbia is large enough to provide a stable supply of wood or straw in the amount necessary for mine water purification of characteristics as those given in Table 1.

Provisional investment costs and expenditures of the process

Investments in the process, presented in Figure 2, could be provisionally estimated for each unit separately, and the resulting items summed for the whole process. Investments in an ash treatment plant are difficult to estimate due to different possibilities arising from Figure 4 and discussed in subtitle 2.4.

Investment costs

There are different approaches for estimating investment costs for cogenerative power plants burning biomass. The most commonly used method is to apply the coefficient of specific investment costs i_c, defined per installed power unit. According to the literature, the i_c vary in many values - from $0.31 \cdot 10^6$ €/MW to $3.5 \cdot 10^6$ €/MW [19,32–36]. It is worth noting that investments largely depend on the plant size. The larger the plants, the lower the i_c is, and vice versa. The i_c will also vary from country to country, depending on government benefits and credit terms, but very much on the equipment supplier.

Some authors suggest estimating specific investment costs according to a turnkey plant delivery model, including all the preliminary (biomass market research, feasibility studies, ground acquisition, contracting, designing, and others) and post-delivery expenses (training, licensing, etc.) [32].

The chosen $i_c = 1.0 \cdot 10^6$ €/MW will be in this study. According to the output power, estimated from Eq. (12), the approximate investment costs i_c will be:

$$I_c = N \cdot i_c = 25.1 \cdot 10^6 € \tag{15}$$

Investments for the two-staged adsorption unit should be added to this value, including all the auxiliary devices, estimated to be $I_a \approx 7 \cdot 10^6$ € [37], including costs for the energy and fluid supply. The biomass preparation system, which includes transport, shredding and dust removal, a rinsing bath, and a drying platform, can be up to I_p =1,500.000 €, so that the total investments will be:

$$I_c = \Sigma I_i = I_h + I_a + I_p = 34.6 \cdot 10^6 € \tag{16}$$

All the construction costs for two ponds and facilities on the micro location should be added to this sum. These costs will strongly depend on the size of the construction area and the surrounding terrain configuration, which cannot be estimated at this stage. The sum in Eq. (16) does not include costs of the land area, building construction works, or the infrastructure construction - local roads, water supply, electricity, taxes, etc.

Since the plant belongs to objects producing green energy, construction of such kinds of plants is being supported by bank credits, EU funds, “carbon credit,” local government funds, and finally, the company's investment fund, which usually participates up to 50% in the whole financial construction. Supposing that bank loans make approximately one-third of the total investments, with a repayment period of 10 years and interest of 2.5%, the loan repayment will be $1.18 \cdot 10^6$ €/year.

Major operating costs

Using either wood residue or wheat straw as biomass, at their approximate unit price c_{bm} = 40 €/t, it amounts to:

$$M_{bm} = m \cdot c_{bm} = 2{,}400.000 \text{ €} / \textit{year} \tag{17}$$

The number of workers employed at a cogeneration plant can be estimated based on the following empirical equation:

$$n = 0.3 N_{in} \approx 9 \textit{ workers} \tag{18}$$

The number of workers must be doubled for the employees working at the pumping stations, collection ponds, and in the adsorption unit so that the total number of workers is 18. Including the executives, the total number of employees will be 22. An average gross salary in the European countries is set to be: $S_{av} \approx$ 2000 €/month. Therefore, the annual sum of the labor costs will be:

$$L_C = 12n \cdot S_{av} = 528.000\ €/year \quad (19)$$

The maintenance costs M_c can be set from 4% to 10% of the investment costs. For this calculation, the specific m_c = 0.009 €/kWh will check whether the costs are within the relevant range [36]. For the installed power, the M_c will be:

$$M_c = m_c \cdot E = 2{,}100.000\ €/year \quad (20)$$

Checking gave a figure of 6%, which means the chosen specific price was correct.

The specific depreciation rate d_r depends on the output power, and for such kinds of installations, it is 70.000 €/MW [36]. For an assumed service life of ≥ 25 years, D_r will be:

$$D_r = d_r \cdot N = 1{,}380.500\ €/year \quad (21)$$

Incomes and expenditures of the proposed mine water treatment process

Energy price varies depending on the country, the type of energy (hydro- or thermal energy), the subsidization by the government, or some other form of support. Green energy production usually enjoys various benefits and promotions over the energy produced from conventional fuels. Based on the published prices from the renewable energy market, the heat energy supplied to local communities, supported due to *feed-in tariff*, is P_h =43 €/MWh. In contrast, the electricity price is P_e = 82.2 €/MWh [19]. Based on these unit prices, the heat and electricity energy income will be:

$$IN_h = P_h \cdot E_h = 6{,}226.400\ €/year \quad (22a)$$

$$IN_e = P_e \cdot E_e = 4{,}603.000\ €/year \quad (22b)$$

If the current price of copper on the LME is approximately P_{Cu} = 9000 $/t (March 2021), the annual income from copper that would be obtained from mine waters, assuming that the ash is processed in a copper smelter, will be:

$$IN_{Cu} = 0.95 G_{ad} \cdot P_{Cu} / 1.19 = 1{,}515.990\ €/year \quad (23)$$

where: 0.95 is an overall copper removal efficiency, starting from copper concentrate to electrorefining; 1.19 is €/US$ exchange ratio.

The total income is:

$$IN = \Sigma IN_i = 12{,}345.390\ €/year \quad (24)$$

The considered expenditures include VAT, tax for industrial water discharging (WDT), and ash processing costs (*APC*).

The *APCu* is estimated to be 2000 €/t of copper, or:

$$APC = 2000 \cdot G_{ad} = 440.000\ €/year \quad (25)$$

VAT on the income is assumed to be 10%, so that it will be: VAT ≈ $1.23 \cdot 10^6$ €/year on an annual level.

The tax for discharging industrial waters into surface waters, according to the local regulations for the unit *WDTu* = 4.38 c€/m^3. For an annual volume V_m, it is:

$$WDT = 0.0438 \cdot V_m = 107.700\ €/year \quad (26)$$

In Table 3, the estimated main income and expenditure values of the loaded biosorbent combustion plant are summarized. As expected, the revenue from the delivered energy makes up almost 90% of the total income. Also, the main costs are not so high, making the whole cost analysis positive, with a profit P slightly higher than $2.7 \cdot 10^6$ €/year. Therefore, an approximate investment repayment period (IRP) can be estimated as:

$$IRP = I_c / P = 12.6\ years \quad (27)$$

This period will be extended, taking into account taxes on the profit.

Indeed, the value of recovered copper is and always will be much smaller than the produced energy. Even if the copper value does not make a significant contribution to the financial balance, the ecological aspect of the process is much more effective, contributing to a cleaner environment in two ways:

- because of metal ions removal from mine water and their eventual reuse;
- because of a contribution to a greenhouse gas reduction.
- Namely, CO_2 from burned biomass has a neutral impact on the environment.

CONCLUSION

A new approach to mine water purification from copper and other metal ions has been proposed, encompassing two processes: metal ions biosorption and energy production by burning the loaded biosorbent. The biosorption would be carried out in two stages, continuously for the aqueous phase, in the cross-flow mode according to the biosorbent. In this way, 99% of copper ions could be adsorbed from the mine waters mixture. Then, the loaded biosorbent would be burnt - producing heat and electricity. Based on the annual volume of mining water and its copper potential, the required amount of biosorbent was determined. In addition, the balance of mass and energy in the process was estimated, enabling the estimate of the plant size and the required investments. The main revenues and costs have shown the process viability and contribution of the recovered copper value to the overall process

Table 3. Basic economic indicators of the cogeneration plant for combustion of the biosorbent loaded with copper

Item	Income·10^6 €/year	Item	Cost·10^6 €/year
Heat	6.2264	Biomass	2.4
Electricity	4.603	Maintenance	2.1
Copper	1.516	Labour	0.528
ΣIN_i	12.3454	Ash processing costs	0.44
		Vat (10 %)	1.23
		Depreciation	1.38
		Loan repayment	1.18
		Financial insurance	0.236
		Water discharge. Tax	0.108
		ΣCO_i	9.602
Total income:	12,345.400	Total costs:	9,602.000

* Average annual profit: $P = \Sigma IN_i - \Sigma CO_i = 2.7434 \cdot 10^6$ €/year.

economy. Therefore, the process will significantly contribute to a cleaner environment in an economically and ecologically sustainable way, producing purified mine waters, which could be either reused or discharged to the nearest water recipients. In addition, due to the natural carbon cycle, combustion of the loaded biosorbent will have almost zero CO_2 emission, giving an additional contribution to a cleaner environment.

Acknowledgment

The research presented in this paper was done with the financial support of the Ministry of Education, Science and Technological Development of the Republic of Serbia, within the funding of the scientific research work at the University of Belgrade, Technical Faculty in Bor, according to the contract with registration number 451-03-9/2021-14/ 200131, and the Mining and Metallurgy Institute Bor, Grant No. 451-03-9/2021-14/ 200052. Furthermore, the authors express their appreciation to Mrs. Mara Manzalović, an English Lecturer at the Technical Faculty Bor, the University of Belgrade, for her help in editing the manuscript.

REFERENCES

[1] V. Stanković, B. Božić, M. Gorgievski, G. Bogdanović, M. Žikić, J. Min. Metall. A Min. 57 A (1) (2021) 33–42.

[2] D.B. Johnson, K.B. Hallberg, Sci. Total Environ. 338 (2005) 3–14.

[3] H. Egerer, P.C. Sandei, O. Simonett, P. Peck, Mining and Environment in the Western Balkans, 1st Edition January 2010, Editor: C. Stuhlberger; Publisher: UNDP, UNEP, OSCE, NATO, UNECE and REC.

[4] L. Joseph, B.M. Jun, J.R.V. Flora, C.M. Park, Y. Yoon, Chemosphere 229 (2019) 142–159.

[5] D.K. Nordstrom, R.J. Bowell, K.M. Campbell, C.N. Alpers, Challenges in Recovering Resources from Acid Mine Drainage, in Proceeding of 13th International Mine Water Association Congress - Mine Water & Circular Economy, Lappeenranta, Finland (2017), p.1138–1146.

[6] M. Gorgievski, D. Božić, V. Stanković, G. Bogdanović, J. Hazard. Mater. 170 (2009) 716–721.

[7] V. Stanković, V. Milošević, D. Milićević, M. Gorgievski, G. Bogdanović; Chem. Ind. Chem. Eng. Q. 24(4) (2018) 333–344.

[8] I. Park, C.B. Tabelin, S. Jeon, X. Li, K. Seno, M. Ito, N. Hiroyoshi, Chemosphere, 219 (2019) 588–606.

[9] F.A. Habashi, Textbook of Hydrometallurgy, 2nd Ed, Laval University, Quebec City, Canada (1999).

[10] G. Savov, T. Angelov, A. Tsekov, I. Grigorova, I. Nishkov, XXVI IMPC, 2012, New Delhi, India, Ref. number 1026; https://www.academia.edu/5772175 [accessed 22 April 2021].

[11] D.S. Malik, C.K. Jain, A.K. Yadav; Appl. Water Sci. 7 (2016) 2113–2136.

[12] V. Stanković, D. Božić, M. Gorgievski, G. Bogdanović, Chem. Ind. Chem. Eng. Q. 15 (2009) 237–249.

[13] P. M. Biesheuvel, J. E. Dykstra, Physics of Electrochemical Processes, E-Publishing, Part IV, 2020 p.261; http://www.physicsofelectrochemicalprocesses.com [accessed 4 May 2021].

[14] D. Božić, V. Stanković, M. Gorgievski, G. Bogdanović, R. Kovačević, J. Hazard. Mater. 171 (2009) 684–692.

[15] A. Beni, A. Esmaeili, Environ. Technol. Innovation 17 (2020) 100503.

[16] M. Gorgievski, D. Božić, V. Stanković, N. Štrbac, S. Šerbula, Ecol. Eng. 58 (2013) 113–122.

[17] D. Božić, M. Gorgievski, V. Stanković, N. Štrbac, S. Šerbula, N. Petrović, Ecol. Eng. 58 (2013) 202–206.

[18] P. Lauri, P. Havlík, G. Kindermann, N. Forselln, H. Böttcher, M. Obersteiner, Energy Policy 66 (2014) 19–31.

[19] D. M. Urošević, B. D. Gvozdenac-Urošević, Therm. Sci. 16 (2012) 97–106.

[20] W. Li, B. Mu, Y. Yang, Bioresour. Technol. 277 (2019) 157–170.

[21] N. Hossain, M. A. Bhuiyan, B. K. Pramanik, S. Nizamuddin, G. Griffin, J. Clean. Prod. 255 (2020) 120261.

[22] L. Deng, T. Zhang, D. Che, Fuel Process. Technol. 106 (2013) 712–720.

[23] B. M. Jenkins, R. R. Bakker, J. B. Wey, Biomass Bioenergy, 10 (1996) 177–200.

[24] D. Božić, M. Gorgievski, V. Stanković, M. Cakić, S. Dimitrijević, V. Conić, Chem. Ind. Chem. Eng. Q. 27 (1) (2021) 21–34.

[25] V. Stanković, M. Gorgievski, D. Božić, Biomass Bioenergy, 88 (2016) 17–23.

[26] The Republic of Serbia, Republican Bureau of Statistics, Annual report No. 260, LXIX, 25.09.2019; ISSN 0353-9555; SRB260 PO16 250919.

[27] M. Šupín, V. Kaputa, J. Parobek, Wood biomass as a renewable resources market development in the EU, in Proceeding of 10th International Scientific Conference WoodEMA, Prague, Czech Republic (2017), p. 25–32.

[28] A. Kogej, B. Likozar, A. Pavko, Food Technol. Biotechnol. 48 (2010) 344–351.

[29] P. Kojić, V. Vučurović, N. Lukić, M. Karadžić, S. Popović, APTEFF 48 (2017) 127–139.

[30] V. Stanković, Fenomeni prenosa i operacije u metalurgiji 2 (Prenos toplote i mase) (Translated: Transfer Phenomena and Unit Operation in Metallurgy 2 (Heat and Mass Transfer), University of Belgrade Technical Faculty in Bor, Bor, 1998; CIP 669.021.3/.4(075.8).

[31] I. Jansone, Z. Gaile, Res. Rural Dev. 1 (2015) 40–44.

[32] B. Simović, A. S. Anđelković, M. Kljajić, KGH 4 (2018) 357–364.

[33] G. J. Mayhead, Biomass to Electricity, Woody Biomass Utilization; University of California Berkeley, Oct. 2010.

[34] D. R. McIlveen-Wright, Y. Huang, S. Rezvani, D. Redpath, M. Anderson, A. Dave, N. J. Hewitt, Appl. Energy. 112 (2013) 396–404.

[35] Z. Liu, X. Li, International Conference on Education, Management Science and Economics (ICEMSE-16); Advances in Social Science, Education and Humanities Research (ASSEHR), Volume 65 (2016) 255–258.

[36] P. Odavić, V. Zekić, D. Milić, Economics of Agriculture, 64 (2017) 587–599.

[37] SAMCO, How Much Does an Ion Exchange System Cost? https://www.samcotech.com/how-much-ion-exchange-system-cost/ [accessed on 25 May 2021].

VELIZAR STANKOVIĆ[1]
MILAN GORGIEVSKI[1]
DRAGANA BOŽIĆ[2]
GROZDANKA D. BOGDANOVIĆ[1]

[1]Univerzitet u Beogradu, Tehnički fakultet u Boru, Srbija

[2]Institut rudarstva i metalurgije Bor, Srbija

BIOSORPCIJA JONA TEŠKIH METALA IZ RUDNIČKIH VODA NA SLAMI I TRINI I DOBIJANJE ZELENE ENERGIJE SAGOREVANJEM TAKO ZASIĆENE BIOMASE

Predložen je novi proces za prečišćavanje voda rudnika bakra, koji bazira na objedinjavanju dva procesa - biosorpciji iza koje sledi proizvodnja energije sagorevanjem zasićenog biosorbenta. Pšenična slama i trina dobijena mlevenjem sečke drveća se već koriste kao biomasa u proizvodnji energije, a pokazali su i dobre adsorpcione osobine prema jonima bakra. Proces obuhvata biosorpciju, koja se izvodi u dva stupnja, u unakrsnom režimu tokova faza, čime se postiže stepen adsorpcije jona bakra > 95 %. Za razmatranu količinu rudničke vode i njen hemijski sastav, bilo bi potrebno oko 60.000 t/god biosorbenta. Analizirano je sagorevanje ove količine zasićenog biosorbenta i kogenerativna proizvodnja zelene energije, pri čemu bakar i ostali adsorbovani teški metali bivaju koncentrisani u pepelu, koji treba da se posebno procesira. Nekoliko mogućnosti prerade pepela, radi dobijanja bakra, su predložene i razmatrane.

Procenjen je takođe bilans mase i energije predloženog procesa, za tretman određene godišnje zapremine rudničke vode i dobijanja bakra koji ona nosi. Uz to, dati su neki ekonomski pokazatelji efikasnosti procesa, bazirani na procenjenim prihodima i troškovima procesa. Ekonomska analiza je pokazala da bi proces bio održiv čak i samo na bazi energije proizvedene sagorevanjem biosorbenta, te da dobijeni metal predstavlja dodatni prihod, pri čemu je emisija CO_2 gotovo jednaka nuli što, pored prečišćene vode, dodatno doprinosi čistijoj okolini.

NAUČNI RAD

Ključne reči: biosorpcija, sagorevanje biomase, zelena energija, joni teških metala, rudnička voda.

CI&CEQ
Chemical Industry & Chemical Engineering Quarterly

Available online at
Association of the Chemical Engineers of Serbia *AChE*
www.ache.org.rs/CICEQ

Chem. Ind. Chem. Eng. Q. 28 (4) 265–276 (2022) CI&CEQ

ANA BÁRBARA MOULIN CANSIAN
PAULO WALDIR TARDIOLI
FELIPE FERNANDO FURLAN
RUY DE SOUSA JÚNIOR

Federal University of São Carlos, Department of Chemical Engineering

MODELING AND SIMULATION OF THE BIOSURFACTANT PRODUCTION BY ENZYMATIC ROUTE USING XYLOSE AND OLEIC ACID AS REAGENTS

Article Highlights

- Simulation of sugar ester production by immobilized lipase using oleic acid and xylose as reagents
- Product separation is performed using precipitations by adding ethanol, water, and methyl ethyl ketone
- Simulation performed using EMSO software (Environment for Modeling, Simulation, and Optimization)
- Development of mathematical models that successfully described the process
- Presentation of economic analysis for the biosurfactant production

Abstract

The biosynthesis of sugar esters, molecules with biosurfactant properties, can occur through the esterification of sugars with fatty acids by enzymatic catalysis. An alternative to reduce the impact of raw materials on the final biosurfactant production cost and the reuse of industrial waste is to use residues from vegetable oil industries as a source of free fatty acids, such as oleic acid, and lignocellulosic residues of 2G ethanol as a source of sugar (xylose). In this scenario, the present work aimed at modeling the biosurfactants production via heterogeneous biocatalysis using lipase, oleic acid, and xylose. Product separation and purification were performed using a sequence of precipitations (adding ethanol, water, and methyl ethyl ketone). The simulation was performed using the equation-oriented software EMSO (Environment for Modeling, Simulation, and Optimization), CAPE-OPEN compliant. The percentage of biosurfactants in the product was around 86%, with a recovery of 88% in the purification. Regarding the study of energy expenditure, a value of -604.1 kW of heat associated with cooling and a value of 137.6 kW associated with heating was observed. Developed mathematical models successfully described the process. The initial economic analysis of the process indicates a minimum biosurfactant selling price of US$ 72.37/kg.

Keywords: biosurfactants, esterification, modeling and simulation, purification, precipitation.

SCIENTIFIC PAPER

UDC 544.47:66:54

Biosurfactants are amphipathic molecules obtained by enzymatic or microbiological routes. Like surfactants, they have amphiphilic structures, which means the molecules have hydrophobic and hydrophilic regions [1]. This duality generates interfaces with different degrees of polarity, bringing the substance adsorption characteristic [2]. Emulsification capability, reduction of viscosity and surface tension, stabilizing effect, and solubilizing ionic strength are the main characteristics of these molecules [3]. Based on these characteristics, biosurfactants can be applied in the pharmaceutical, oil, textile, food, and cosmetics industries, among others [4]. However, despite low toxicity, good degradability, thermal stability, specific bioactivity, and other advantages, biosurfactants still lose market share to synthetic surfactants due to their

Correspondence: R. de Sousa Júnior, Federal University of São Carlos, Department of Chemical Engineering, Rod. Washington Luís, km 235 - CEP 13565-905, São Carlos, SP.
E-mail: ruy@ufscar.br
Paper received: 21 June, 2021
Paper revised: 8 January, 2022
Paper accepted: 7 February, 2022

https://doi.org/10.2298/CICEQ210621001C

high production cost [5].

It is important to note that the cost-benefit ratio in applying biosurfactants can be valued for processes that require a lower degree of purity since the separation and purification steps represent about 60% of the final operational cost of production [6]. Another important point that impacts production costs is the choice of reagents, which can reach 50% [7].

The literature reports different studies on the production of sugar esters (biosurfactants) by microbiological route, involving steps of purification using solvent extraction, acid precipitation, centrifugation, filtration, gel filtration chromatography, and lyophilization [8–11]. For enzymatic biosurfactants production, several studies focus on the development or immobilization of catalysts. The synthesis process can occur through the esterification of sugars with fatty acids, with lipase as the main enzyme that catalyzes the reaction [12]. Lipases are part of a group of hydrolytic enzymes found in animals or produced from fermentation using some species of microorganisms. They can catalyze interesterification, transesterification, and esterification reactions [13]. In particular, the immobilization of enzymes appears as a solution for the structural conformation of lipases in environments not conducive to them. In this way, they become stable for catalysis with their active sites exposed [14]. Another advantage of immobilization is the insolubilization of the enzyme in the liquid phase. Depending on the system, it facilitates their separation and reuses for long periods, contributing to reducing process costs. The work [15] achieved a good conversion in the production of glucose esters under specific enzymatic reaction conditions. Some other studies also use enzymes to produce sugar esters, but none focuses on the separation/purification process of the product obtained [16–19].

Several possibilities of employing less costly alternatives to the process exist regarding the used reagents and the biosurfactants' integration within a biorefinery concept. More specifically, within the framework of a biodiesel-bioethanol biorefinery, using by-products such as SODD (Soybean Oil Deodorization Distillate), obtained in the refining stage of soybean oil, and biomass residues, obtained in the production of bioethanol [20–23].

Brazil has geographic and climatic factors that favor the cultivation of various oleaginous species that can be used to produce oils. These species include pine nuts, castor beans, palm kernels, babassu coconuts, sunflower seeds, cotton, peanuts, linseeds, canola seeds, soybeans, corn, etc. On the other hand, residual vegetable oils result from domestic or industrial processes, citing examples of frying oils, industrial wastewater, or by-products originating from refining stages, such as SODD [24, 25]. Vegetable oils and their residues are mainly composed of mono, di, triglycerides, and fatty acids, justifying their use as raw material in the production of esters [26].

Process residues involving biomass (such as sugarcane bagasse), in turn, have a high potential for conversion into renewable products with high commercial value [27]. In particular, it is possible to obtain xylose from these residues. Lignocellulosic biomass needs pretreatment to disorganize the lignocellulosic complex and increase its surface area [20]. Following the pretreatment, hydrolysis occurs. Cellulose and hemicellulose are hydrolyzed and generate several products. Cellulose produces glucose, while hemicellulose is broken down into hexoses, pentoses (like xylose), glucuronic acid, and acetic acid [28].

Thus, to contribute to the study of the production of biosurfactants in the context of a biodiesel-bioethanol biorefinery, the present paper aimed at modeling and simulating biosurfactants production via heterogeneous biocatalysis with immobilized lipases using oleic acid and xylose as reagents. The work was modeled and simulated in an EMSO environment (Environment for Modeling, Simulation, and Optimization). The EMSO simulator is an equation-oriented process simulator for modeling steady-state and dynamic processes. It is the CAPE-OPEN standard compliant. Pre-built models are available in the EMSO Modeling Library (EML). Besides, new models can be written in the EMSO modeling language. The behavior of the variables for the route under development was verified, and the energy costs were assessed throughout the process. Furthermore, the work aimed to simulate a separation/purification process as an alternative to the more complex and costly steps mentioned in the literature. Such an alternative for the separation/purification of the product is a sequence of precipitation processes.

MATERIAL AND METHODS

The main equipment used for computational simulations was a desktop with an Intel 7700K core I7 4.20 GHZ processor, 32 GB of RAM. In addition, a notebook with an Intel 3210M core I5 2.5 GHZ, 4 GB of RAM was also employed in the project. The software used was EMSO academic beta version 0.10.9.

The route evaluated in this work encompasses the process of producing biosurfactants via heterogeneous biocatalysis using immobilized lipases. Oleic acid and xylose were used directly as reagents. The process fol-

lows the lipase recovery and reuse and the product separation and purification by a sequence of precipitations. This production route is presented in detail in Figure 1.

Modeling

For the simulation of the process to be possible, it is necessary to model each equipment unit and specify the operating conditions and considerations used in the models. The main equations on which the models are based will be presented. Table 1 shows the components used throughout the modeling and simulation processes.

MIXER: The mixers used in this work were assumed

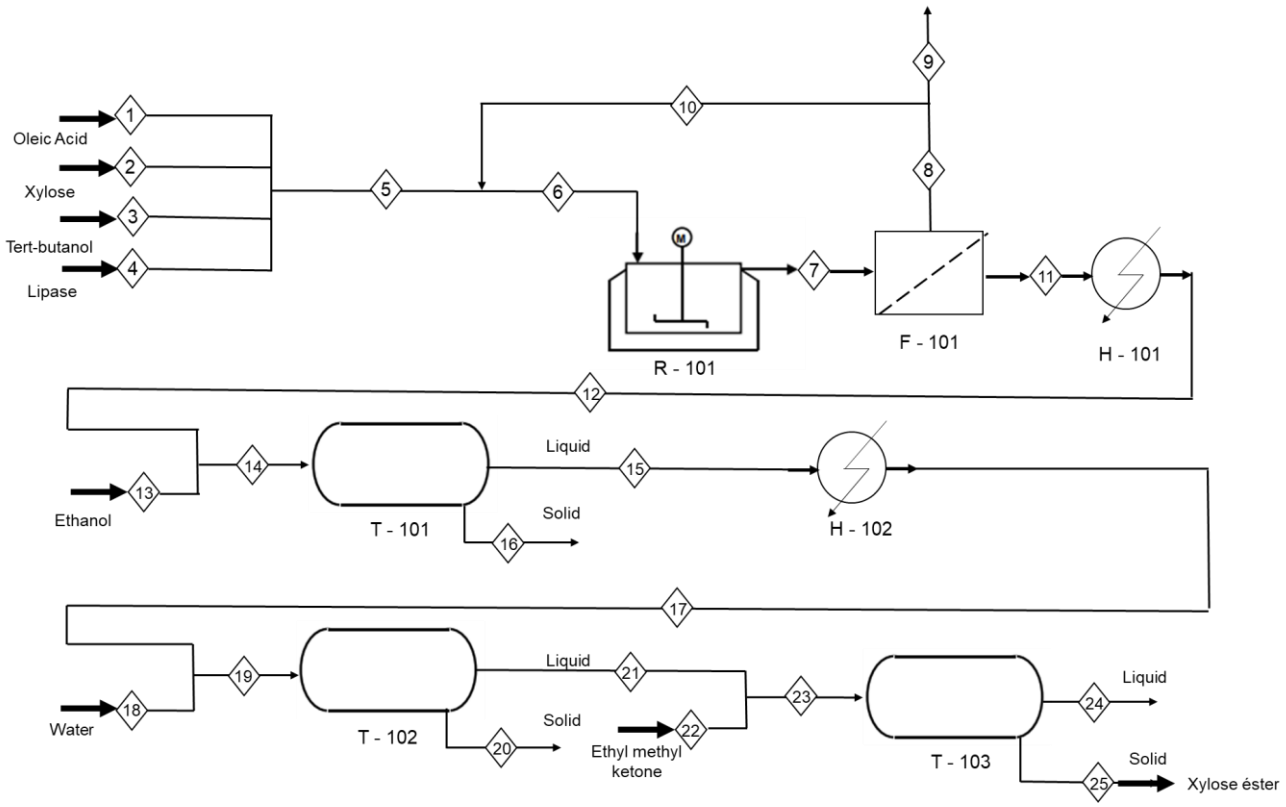

Figure 1. Representation of the production process of biosurfactants by the enzymatic route.

Table 1. Components phase used in the simulation

Components in the liquid phase	Components in the solid phase
Xylose	Immobilized Lipase
Oleic Acid	Xylose
Xylose Ester	Oleic Acid
Tert-butanol	Xylose Ester
Ethanol	
Water	
Ethyl Methyl Ketone	

to be static and adiabatic. This equipment has two inputs and one output, and the solid and liquid phases are considered. Thus, each balance is carried out for both phases.

"Global molar balance"

$$Inlet1.F + Inlet2.F = Outlet.F \quad (1)$$

where, *Inlet1.F* - the molar flow of the input 1 of the equipment (kmol/h); *Inlet2.F* - the molar flow of the input 2 of the equipment (kmol/h); *Outlet.F* - the molar flow of the equipment outlet (kmol/h).

"Molar balance per component"

$$Inlet1.F \times Inlet1.z + Inlet2.F \times Inlet2.z = Outlet.F \times Outlet.z \quad (2)$$

where, *Inlet1.z* - molar composition of the input 1 of the equipment (kmol of component/kmol total); *Inlet2.z* - molar composition of the input 2 of the equipment (kmol of component/kmol total); *Outlet.z* - molar composition of the output of the equipment (kmol of component/kmol total).

“Consideration for pressure”

$$Outlet.P = \min[(Inlet1.P, Inlet2.P)] \quad (3)$$

where, *Outlet.P* - pressure of the outlet stream of the equipment (kPa); *Inlet1.P* - pressure of the input stream 1 of the equipment (kPa); *Inlet2.P* - pressure of the input stream 2 of the equipment (kPa).

"Energy balance"

$$Outlet.F \times Outlet.h = Inlet1.F \times Inlet1.h + Inlet2.F \times Inlet2.h \quad (4)$$

where, *Outlet.h* - enthalpy of the output stream of the equipment (kJ/kmol); *Inlet1.h* - enthalpy of the input stream 1 of the equipment (kJ/kmol); *Inlet2.h* - enthalpy of the input stream 2 of the equipment (kJ/kmol).

ESTERIFICATION REACTOR: The reactor was assumed to be stoichiometric and steady-state, with the conversion specified based on the reaction limiting reagent. This equipment has a single input and one output. The solid and liquid phases are considered, so each balance is carried out for both phases.

“Reaction rate”

$$r = stoic \times conv \times z(\text{limit}) \quad (5)$$

where, *r* - reaction rate (dimensionless); *stoic* - matrix of stoichiometric coefficients (dimensionless); *conv* - reaction conversion (dimensionless); *z(limit)* - molar fraction of the limiting reagent for each reaction (dimensionless).

“Molar balance per component”

$$Outlet.F \times Outlet.z = Inlet.F \times Inlet.z + F \times r \quad (6)$$

where, *F* - total molar flow of the equipment inlet (kmol/h).

"Energy balance"

$$Outlet.F \times Outlet.h = Inlet.F \times Inlet.h + Q - F \times sum(h_R \times conv \times z(\text{limit})) \quad (7)$$

where, *Q* - heat removed from the reactor so that the temperature is maintained (kW or kJ/h); h_R - enthalpy of reaction (kJ/kmol).

“Reactor pressure”

$$Inlet.P = Outlet.P \quad (8)$$

FILTER: The filtration employed separates the solids present from the liquid phase in steady-state and adiabatic conditions. This equipment has a single inlet and two outlets, one with a higher concentration of solids and the other of liquids. The solid and liquid phases are considered, so each balance is carried out for both phases.

“Global molar balance”

$$Inlet.F = OutletS.F + OutletL.F \quad (9)$$

where, *OutletS.F* - the molar flow of solids output from the equipment (kmol/h); *OutletL.F* - the molar flow of liquids output from the equipment (kmol/h).

"Efficiency of liquid separation"

$$OutletL.Fluid.Fw = Inlet.Fluid.Fw \times frac\_liq \quad (10)$$

where, *OutletL.Fluid.Fw* - mass flow of the fluid in the liquid outlet stream (kg/h); *Inlet.Fluid.Fw* - mass flow of the fluid in the equipment inlet stream (kg/h); *frac_liq* - fraction of liquids from the inlet leaves the equipment in the liquid stream (kg of liquids/kg total).

“Efficiency of solid separation”

$$OutletS.Solid.Fw = Inlet.Solid.Fw \times frac\_sol \quad (11)$$

where, *OutletS.Solid.Fw* - mass flow of solids in the equipment solids outlet (kg/h); *Inlet.Solid.Fw* - mass flow of solids in the equipment entrance (kg/h); *frac_sol* - fraction of solids from the inlet leaves the equipment in the solid stream (kg of solids/ kg total).

“Humidity in the solid stream”

$$humidity = \frac{OutletS.Fluid.Fw}{OutletS.Total.Fw} \quad (12)$$

where, *humidity* - fraction of liquids in the equipment solids outlet (kg of liquids/kg total).

“Impurities in the liquid stream”

$$OutletL.Solid.Fw = impurity \times (OutletL.Total.Fw) \quad (13)$$

where, *OutletL.Solid.Fw* - mass flow of solids in the liquid outlet of the equipment (kg/h); *Impurity* - fraction of solids in the liquid outlet of the equipment (kg of solids/kg total); *OutletL.Total.Fw* - total mass flow of the equipment liquid outlet (kg/h).

"Thermal balance"

$$OutletS.T = Inlet.T \quad (14)$$

$$OutletL.T = Inlet.T \quad (15)$$

"Mechanical balance"

$$OutletS.P = Inlet.P \quad (16)$$

$$OutletL.P = Inlet.P \quad (17)$$

“Enthalpy of the streams”

$$OutletS.h = Inlet.h \quad (18)$$

$$OutletL.h = Inlet.h \quad (19)$$

COOLER: The cooler was used to cool the process stream in a steady-state and with no heat loss to the environment. This device has a single input and one output without changing the stream mass. The solid and liquid phases are considered, so each balance is carried out for both phases.

“Molar balance”

$$Inlet.F = Outlet.F \tag{20}$$

"Composition"

$$Outlet.z = Inlet.z \tag{21}$$

“Pressure Delta”

$$Outlet.P = Inlet.P - Pdrop \tag{22}$$

where, *Pdrop* - head loss in the heat exchanger (kPa).

“Heat exchanged”

$$Q = U \times A \times lmtd \tag{23}$$

$$lmtd = \frac{\Delta T_1 - \Delta T_2}{\ln\left(\frac{\Delta T_1}{\Delta T_2}\right)} \tag{24}$$

where, *Q* - heat exchanged in the equipment (kW); *U* - global coefficient of thermal exchange (kW/m²/K); *A* - heat exchange area (m²); *lmtd* - logarithmic mean temperature difference (K).

SPLITTER: The separators used in this work were assumed to be static and adiabatic. This equipment has a single input and two outputs. The solid and liquid phases are considered, so each balance is carried out for both phases.

“Global molar balance”

$$Inlet.F = Outlet1.F + Outlet2.F \tag{25}$$

“Molar balance per component”

$$Inlet.F \times Inlet.z = Outlet1.F \times Outlet1.z + Outlet2.F \times Outlet2.z \tag{26}$$

“Consideration for pressure”

$$Outlet1.P = Inlet.P \tag{27}$$

$$Outlet2.P = Inlet.P \tag{28}$$

"Energy balance"

$$Outlet1.F \times Outlet1.h + Outlet2.F \times Outlet2.h = Inlet.F \times Inlet.h \tag{29}$$

PUMP: The pump operates in a steady-state to correct a particular pressure drop. The equipment has a single entrance and a single exit. Therefore, there is no heat exchange with the environment, and, again, all balances occur for liquid and solid phases.

“Molar balance for the liquid phase”

$$Inlet.Fluid.F = Outlet.Fluid.F \tag{30}$$

“Molar balance for the solid phase”

$$Inlet.Solid.F = Outlet.Solid.F \tag{31}$$

“Molar fraction for the liquid phase”

$$Outlet.Fluid.z = Inlet.Fluid.z \tag{32}$$

“Molar fraction for the solid phase”

$$Outlet.Solid.z = Inlet.Solid.z \tag{33}$$

"Head loss"

$$Outlet.P = Inlet.P + Pln \tag{34}$$

where, *Pin* - pressure delta.

"Energy balance"

$$Inlet\_p.W = Inlet.Fluid.F \times (Outlet.Fluid.h - Inlet.Fluid.h) + Inlet.Solid.F \times (Outlet.Solid.h - Inlet.Solid.h) \tag{35}$$

“Work”

$$Inlet\_p.W = (Inlet.Fluid.Fw + Inlet.Solid.Fw) \times \frac{Pln}{n \times density} \tag{36}$$

where, *n* - pump efficiency (dimensionless).

Simulation

According to Figure 1, the process starts by mixing the reactants (oleic acid and xylose), the solvent (tert-butanol), and the enzyme (lipase) to form stream 5, which is mixed to the system recycle and enters the bioreactor. Next, the reactor outlet, stream 7, goes downstream to filtration, where part of the immobilized enzyme is recycled (a fraction is removed from the process (stream 9) while another is reinserted (stream 10)). Afterward, the enzyme-free stream goes to the purification process, where stream 11 is cooled and mixed with ethanol in a separation tank. As a result, a solid-liquid equilibrium is formed, and the solid phase is removed from the process. In the sequence, stream 15 is cooled, and water is added to the stream to create a new solid-liquid equilibrium in a tank where the solid formed is removed. Soon after, ethyl methyl ketone is inserted into the process in a way that the formed precipitated contains the product of interest, xylose ester (stream 25).

The process simulation occurs to approximate the operating conditions of a given operational scheme and verify the behavior of some variables. Thus, the EMSO software was used to solve the equations describing the process based on the previously presented modeling. Tables 2 and 3 show the main specifications for the process simulation. As the simulated process has 2554 variables and 2419 equations, 135 specifica-

tions are needed. Thus, the remaining specifications are found in the supplementary material (Table A1).

It is worth mentioning that the value of 1 10^{-6} present throughout the tables refers to the value zero and is used to avoid convergence problems. The information present in [29] was used for the reaction conditions, with the xylose to free fatty acids (FFA; here represented by the Oleic Acid) molar ratio of 1:5, so for every 2.16 mmoles of xylose-FFA, there is 6 mL of tert-butanol (as organic solvent) and 0.6 g of lipase, the temperature of 60 °C and conversion of 70%. As detailed elsewhere [29], a suspension containing octyl-silica and enzyme solution was used for the immobilization. The reaction of esterification of xylose with FFA follows the stoichiometry of Equation 37.

In the second stage of the process, there are precipitation tanks to purify the biosurfactant (Figure 1). Wagner *et al.* [30] presented a method for separating and purifying sugar esters based on the precipitation of compounds. That method consisted of adding ethanol, water, and ethyl methyl ketone to purify the ester (a sucrose ester, in the specific case addressed by the authors [30]). The first tank aims to precipitate the xylose (by adding ethanol), removed from the process, following Eq. (38). The next two tanks (the second and the third) are intended to precipitate/purify the xylose ester. In the second tank, the ester precipitation occurs with the presence of water, but part of the FFA is precipitated together with the ester. The last precipitation tank uses ethyl methyl ketone, which solubilizes part of the FFA, leaving the xylose ester more concentrated in the solid phase to achieve a higher level of purification. The second process separation tank has three equations to represent what happens in precipitations and solubilizations. Equation 39 is the representation of the xylose ester precipitation. Equation 40 represents the precipitation of the FFA, and Equation 41 the solubilization of xylose in water. The third and last separation tank aims to solubilize the FFA and thus increase the concentration of ester in the product. Equation 42 represents the solubilization of FFA in ethyl methyl ketone.

Table 2. Variables specified in the process input streams

Stream	Phase	Variable	Name	Unit	Value
Streams 1, 2,3 and 4	All	T	Temperature	K	333.15
Streams 1, 2,3 and 4	All	P	Pressure	atm	1
Streams 1, 2 and 3	Solid	F	Molar flow	kmol/h	1 10^{-6}
Stream 1	Liquid	F	Molar flow	kmol/h	50
Stream 2	Liquid	F	Molar flow	kmol/h	10
Stream 3	Liquid	F	Molar flow	kmol/h	175
Stream 4	Liquid	F	Molar flow	kmol/h	1 10^{-6}
Source 4	Solid	F	Molar flow	kmol/h	79.6
Stream 1	Solid	z(1)*	Composition	dimensionless	1
Stream 1	Solid	z(2–4)*	Composition	dimensionless	0
Stream 1	Liquid	z(1)*	Composition	dimensionless	0
Stream 1	Liquid	z(2)*	Composition	dimensionless	1
Stream 1	Liquid	z(3–7)*	Composition	dimensionless	0
Streams 2, 3 and 4	Solid	z(1)*	Composition	dimensionless	1
Streams 2, 3 and 4	Solid	z(2–4)*	Composition	dimensionless	0
Stream 2 and 4	Liquid	z(1)*	Composition	dimensionless	1
Stream 2 and 4	Liquid	z(2–7)*	Composition	dimensionless	0
Stream 3	Liquid	z(1–2)*	Composition	dimensionless	0
Stream 3	Liquid	z(3)*	Composition	dimensionless	0
Stream 3	Liquid	z(4)*	Composition	dimensionless	1
Stream 3	Liquid	z(5–7)*	Composition	dimensionless	0

* Component number: Liquids: 1-Xylose; 2-Oleic Acid; 3-Xylose Ester; 4-Tert-butanol, 5-Ethanol; 6-Water; 7-Ethyl Methyl Ketone. Solid: 1-Immobilized Lipase; 2-Xylose; 3-Oleic Acid; 4-Xylose Ester.

Table 3. Variables specified for the equipment

Equipment	Variable	Name	Unit	Value
Reactor 101	conv	Conversion	dimensionless	0.7
Reactor 101	T	Temperature	K	333.15
Filter 101	frac_sol	Fraction of solids in the liquid stream	dimensionless	0.99
Filter 101	humidity	Fraction of liquid in the solid stream	dimensionless	0.10
Splitter between streams 8 and 9	frac	Fraction of the stream that will be removed from the process	dimensionless	0.10
Cooler 101	Pdrop	Pressure loss	atm	0
Cooler 101	Outlet.T	Output temperature	K	323.15
Cooler 101	U	Global heat exchange coefficient	kW/m²/K	0.6945

$$C_5H_{10}O_5(l) + C_{18}H_{34}O_2(l) \Leftrightarrow C_{23}H_{42}O_6(l) + H_2O(l) \quad (37)$$
$$(Xylose)\ (Oleic\ Acid)\ (Xylose\ ester)\ (Water)$$

$$C_5H_{10}O_5(l) \Leftrightarrow C_5H_{10}O_5(s) \quad (38)$$
$$(Liquid\ xylose)\ (Solid\ xylose)$$

$$C_{23}H_{42}O_6(l) \Leftrightarrow C_{23}H_{42}O_6(s) \quad (39)$$
$$(Liquid\ xylose\ ester)\ (Solid\ xylose\ ester)$$

$$C_{18}H_{34}O_2(l) \Leftrightarrow C_{18}H_{34}O_2(s) \quad (40)$$
$$(Liquid\ FFA)\ (Solid\ FFA)$$

$$C_5H_{10}O_5(s) \Leftrightarrow C_5H_{10}O_5(l) \quad (41)$$
$$(Solid\ xylose)\ (Liquid\ xylose)$$

$$C_{18}H_{34}O_2(s) \Leftrightarrow C_{18}H_{34}O_2(l) \quad (42)$$
$$(Solid\ FFA)\ (Liquid\ FFA)$$

RESULTS AND DISCUSSION

Simulation

Table A2 presented in the supplementary material presents the data for stream 7, found immediately after the reactor output. It is noticed that there is recovery and recycling of enzymes in the process. The flow rate of the lipase source (line 8 of Table 2) was adjusted so that the flow of the enzyme into the esterification reactor (line 15 of Table A2) was in accordance with the literature since 10% of this current is removed from the process. It is important to note that the lipase loses activity during the reactions. Therefore, the splitter is present in the simulation, representing a fraction of the enzyme stream removed from the process. In the study by Vescovi *et al.* [29], the immobilized enzyme loses its total activity in about 100 h of reactions. The results for the recycle stream (Stream 10) and the stream that removes lipase from the process (Stream 9) are shown in Table A2. In the simulation, it was necessary to add a pump to correct the numerical errors inserted in the pressures. As in some cases of mechanical equilibrium, the pressure at the output of the equipment was given by the minimum between the pressures of the inlet streams, and the solution of the set of equations subtly modified these pressures and, consequently, the minimum pressure. This phenomenon led to the numerical non-convergence of the simulation. After countless tests and verifications to identify the problem, a loss of pressure was noticed throughout the process, resulting from the numerical solution. A pump was used in the recycle to circumvent this problem. The pump is located before the reactor, just after the separator (Stream 10).

After the esterification reaction and the filtration for reuse of the enzymes, the stream has the composition shown in Table 4. Notice that FFA is in greater quantity since it was placed in excess to get the degree of conversion of 70%.

Mass balances are consistent with the results presented by Vescovi *et al.* [29], obtaining the production described by the authors. However, as the mass fraction of xylose ester in the stream is approximately 10.3%, some purification steps are necessary to achieve higher biosurfactant concentrations in the product. Therefore, the reaction followed by the enzyme filtration step alone is insufficient for this process.

The purification of the xylose ester consists of consecutive steps of the precipitant addition followed by precipitation. Figure 2 shows a graph of the composition of the streams after each purification step. The product enters this process at 10.3% (step 1: reactor exit after enzyme removal) in mass composition and reaches 10.4% in the first precipitation process (step 2: first precipitation process with ethanol). In the second precipitation, it reaches 37.6% (step 3: second

Table 4. Results for stream 12

Phase	Variable	Name	Unit	Value
Liquid	Fw	Mass flow	kg/h	28408.4
Solid	Fw	Mass flow	kg/h	166.793
All	T	Temperature	K	323.15
All	P	Pressure	atm	1
Liquid	zw(1)*	Composition	dimensionless	0.0154
Liquid	zw(2)*	Composition	dimensionless	0.4236
Liquid	zw(3)*	Composition	dimensionless	0.1030
Liquid	zw(4)*	Composition	dimensionless	0.4537
Liquid	zw(5)*	Composition	dimensionless	0
Liquid	zw(6)*	Composition	dimensionless	0.0045
Liquid	zw(7)*	Composition	dimensionless	0
Solid	zw(1)*	Composition	dimensionless	1
Solid	zw(2–4)*	Composition	dimensionless	0

* Component number: Liquids: 1-Xylose; 2-Oleic Acid; 3-Xylose Ester; 4-Tert-butanol, 5-Ethanol; 6-Water; 7-Ethyl Methyl Ketone**.** Solid: 1-Immobilized Lipase; 2-Xylose; 3-Oleic Acid; 4-Xylose Ester.

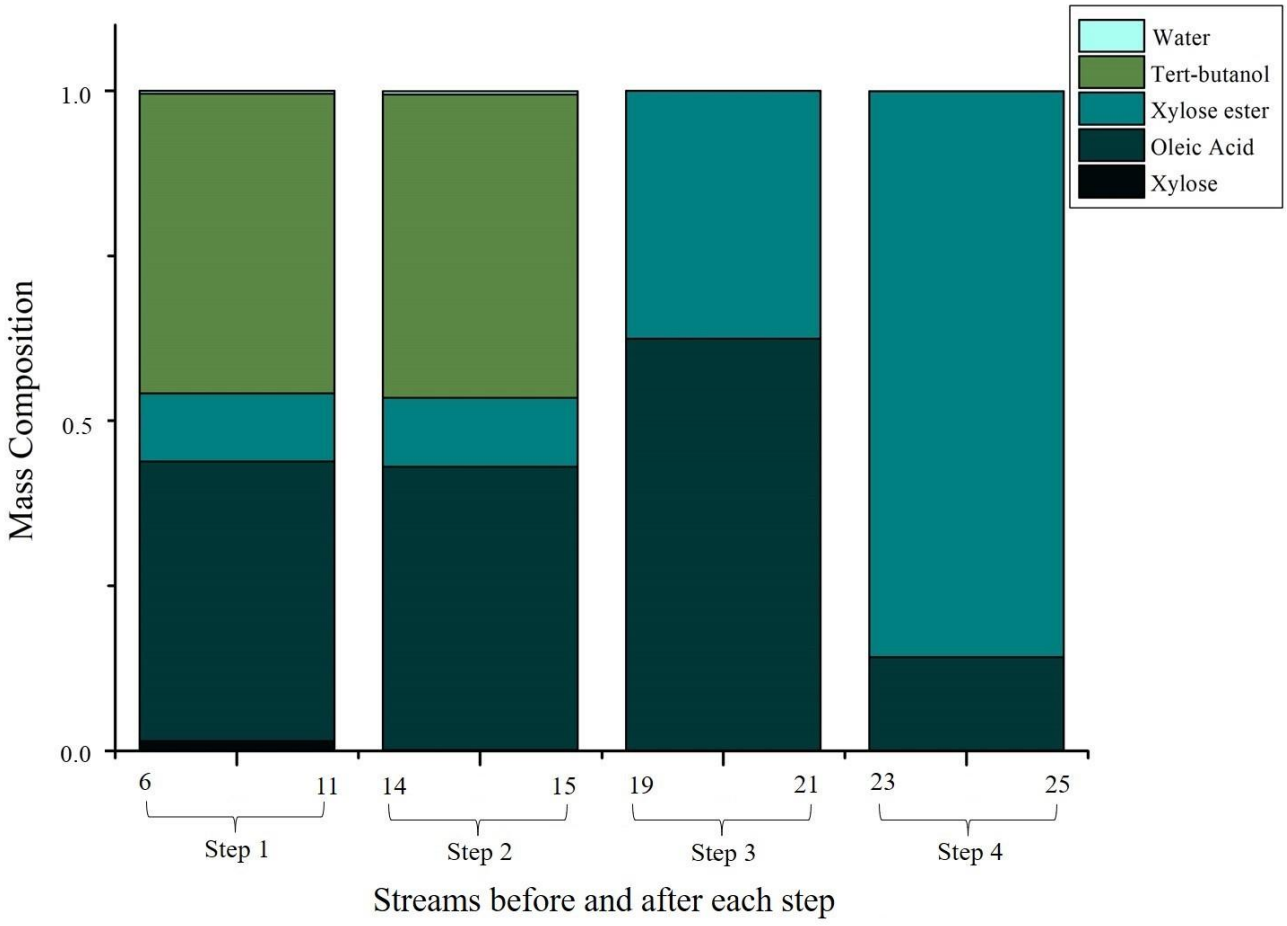

Figure 2. Mass composition of the streams after each stage (1, 2, 3, and 4) and streams identification (associated with each step, before and after them).

precipitation process with water), and in the third (last) precipitation process, it reaches 85.7% (step 4: third precipitation process with ethyl methyl ketone, Table 5).

Thus, the purification process indicates an overall efficiency of 88% ((0.857-0.103)/0.857). The literature does not report purification processes for obtaining biosurfactants by enzymatic route, using oleic acid and xylose as reagents. However, Mukherjee *et al.* [8] reported purification for biosurfactants obtained by the microbiological route. The separation proceeds from several complex steps (acidification, cooling, gel filtration chromatography, and lyophilization) to reach a lyophilized product with high purity. Regarding the degree of complexity of the proposed steps, the present work has reached a satisfactory purity using simpler equipment.

Energy costs throughout the process are shown in Table 6, separated by equipment.

Table 5. Results for stream 25

Phase	Variable	Name	Unit	Value
Liquid	Fw	Mass flow	kg/h	367.413
Solid	Fw	Mass flow	kg/h	3306.72
All	T	Temperature	K	298.15
All	P	Pressure	atm	1
Liquid	zw(1)*	Composition	dimensionless	0.0004
Liquid	zw(2)*	Composition	dimensionless	0.8860
Liquid	zw(3)*	Composition	dimensionless	0.0002
Liquid	zw(4)*	Composition	dimensionless	0.1037
Liquid	zw(5)*	Composition	dimensionless	0.0002
Liquid	zw(6)*	Composition	dimensionless	0.0011
Liquid	zw(7)*	Composition	dimensionless	0.0084
Solid	zw(1)*	Composition	dimensionless	0.0005
Solid	zw(2)*	Composition	dimensionless	0
Solid	zw(3)*	Composition	dimensionless	0.1424
Solid	zw(4)*	Composition	dimensionless	0.8571

* Component number: Liquids: 1-Xylose; 2-Oleic Acid; 3-Xylose Ester; 4-Tert-butanol, 5-Ethanol; 6-Water; 7-Ethyl Methyl Ketone. Solid: 1-Immobilized Lipase; 2-Xylose; 3-Oleic Acid; 4-Xylose Ester.

Table 6. Energy costs of the simulated process

Equipment	Heat (kW)
Esterification reactor	137.58
Cooler 101	- 178.74
Cooler 102	- 425.39

In general, greater heat is associated with cooling (coolers 101 and 102, -604.14 kW) than heating (esterification reactor, 137.58 kW), with total heat of - 466.56 kW. The energy expenditure figures exposed do not consider an energy integration of the process. If a possible energy integration is evaluated to feedback heat into the process, expenses can significantly reduce operating costs. However, when assessing global energy costs, the used equipment requires less heat than equipment used in producing biosurfactants by microbiological routes [8].

Finally, to demonstrate the potential of the developed tool, a simple sensitivity analysis was carried out, showing the effect of the conversion of the esterification reactor on the mass composition of the final product.

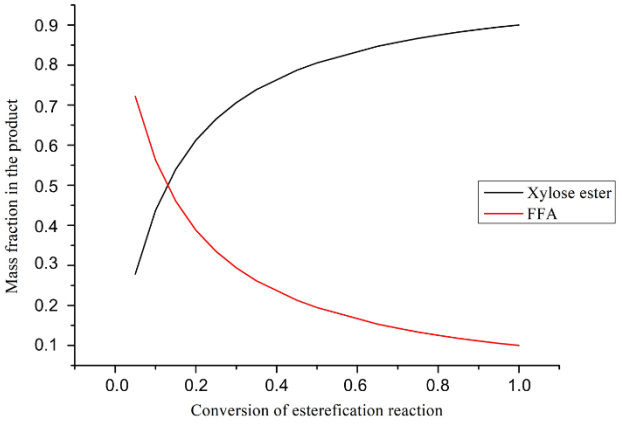

Figure 3. Ester/FFA fraction in the final stream of process versus conversion of the reactor.

From Figure 3, the gain of purity of xylose ester in the final product increases according to the conversion

of reagents to ester in the reactor. Note that the behavior of the final product concentration has an exponential correlation with the conversion of the esterification reaction. For values around 15% conversion, the concentration of esters is greater than FFA in the final stream. It is worth mentioning that the final product concentration increases subtly at conversion values close to 100%. Therefore, there is no need for further research to increase the conversion above 70% to impact the final purity of the product.

Economic analysis

The process simulated in this work was calculated and analyzed for capital and operating costs. All the details of the calculations for this analysis are in the supplementary material (Appendix B). For equipment costs, the methodology from [31] was used. Their parameters are shown in Table 7. The capacity of the equipment units and their calculated costs are shown in Table 8.

For the operating costs evaluated in the economic analysis of the process, the raw material, labor, utility, operating supervision, and maintenance costs were considered. These costs are presented in Table 9. Table 10, in turn, shows the cash flow for the process.

Table 7. Equipment cost parameters to be used in economic analysis

Equipment	K_1	K_2	K_3	FBM or (B1 and B2)	LF_B	A_{min}	A_{max}	Unit
Esterification reactor (Jacketed agited)	4.1052	-0.4680	-0.0005	4.00	1.14	0.1	35	m³
Filter (Gravity)	4.2756	-0.648	0.0714	1.65	1.14	0.5	80	m²
Heat exchanger (Fixed tube)	4.3247	-0.3030	0.1634	1.63 1.66	1.14	10	1000	m²
Process Vessel (Horizontal)	3.5565	0.3776	0.0905	1.49 1.52	1.14	0.1	628	m³

* Adapted from [31].

Table 8. Equipment capacity according to process simulation and associated costs obtained

Equipaments	Capacity	Cost
Esterification reactor (Jacketed agited)	1451.87 m³ (Volume)	MUS$ 0.7931
Filter (Gravity)	39.75 m² (Area)	MUS$ 0.0086
Heat exchanger 1 (Fixed tube)	25.74 m² (Area)	MUS$ 0.1077
Heat exchanger 2 (Fixed tube)	61.26 m² (Area)	MUS$ 0.1303
Process Vessel 1 (Horizontal)	28.43 m³ (Volume)	MUS$ 0.1169
Process Vessel 2 (Horizontal)	27.99 m³ (Volume)	MUS$ 0.1158
Process Vessel 3 (Horizontal)	0.89 m³ (Volume)	MUS$ 0.0204
Total	-	MUS$ 1.2927
Total plant installation	-	MUS$ 1.5254

* MUS$ = Million US$.

Table 9. Operating costs

Raw material costs	MUS$ 1.0240 10³/year
Labor costs	MUS$ 0.5119/year
Utility costs	MUS$ 0.0197/year
Operating supervision costs	MUS$ 0.0256/year
Maintenance costs	MUS$ 0.0763/year
Total operating costs	MUS$ 1.0243 10³/year

The cash flow presented in Table 10 refers to the case of a null net present value, which represents the minimum biosurfactant selling price (MBSP). The value obtained for a minimum attractive rate of return of 11% per year and project life of 25 years was US$ 72.37/kg. This price is coherent with some references presented in the literature [32, 33].

Table 10. Process cash flow

Total operation cost	MUS$ 1.0243 10³/year
Total revenue	MUS$ 1.0338 10³/year
Cash flow	MUS$ 9.5703/year

A sensitivity analysis was also performed regarding the process scale (Figure 4).

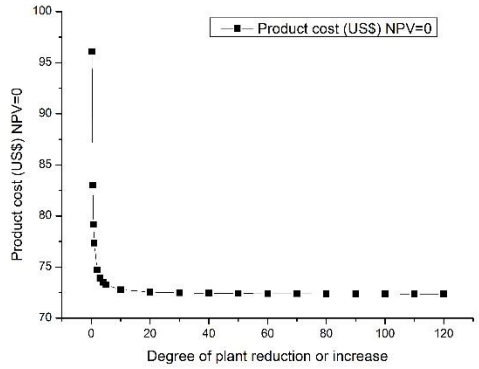

Figure 4. Product sales value depending on the degree of reduction or increase of the original plant (100%), with NPV = 0.

No gain in the MBSP is observed for scales between 20% and 120% of the base case. Also, a rapid increase in MBSP is seen for scales below 20% of the base case.

CONCLUSION

For the proposed esterification process, by the immobilized lipase of oleic acid with xylose, recovery and reuse of enzymes, and separation/purification of the product, it was possible to develop mathematical models that successfully described the process. The simulation of the purification steps indicated a product with 86% in biosurfactants, which increased their recovery by 88%. It was also possible to obtain estimates of energy costs for the process. Compared to the works reported in the literature, the proposal presents itself as a more energy-efficient and less complex alternative that uses cheaper equipment to purify biosurfactants. In addition, it is a suggested use for co-products from soy oil and 2G ethanol productions. It is worth mentioning that energy expenditure does not yet consider the integration of the process. Therefore, energy integration analysis can still significantly reduce these in future works. The initial economic analysis of the process indicates a minimum biosurfactant selling price of US$72.37/kg for a minimum attractive rate of return of 11%.

Acknowledgment

This study was financed in part by the Coordenação de Aperfeiçoamento de Pessoal de Nível Superior - Brasil (CAPES) - Finance Code 001. The authors would also like to thank CNPq, for the financial support in the GM category and process number 132826 / 2018-6. And finally, to São Paulo Research Foundation (FAPESP) for the financial support given through insertion in the Thematic Project with process number 2016 / 10636-8.

REFERENCES

[1] D.K.F. Santos, R.D. Rufino, J.M. Luna, V.A. Santos, L.A. Sarubbo, Int. J. Mol. Sci. 17 (2016) 401–432.

[2] P.R.F. Marcelino, Ph.D. Thesis, Lorena School of Engineering at the University of São Paulo (2016).

[3] L.A. Sarubbo, J.M. Luna, G.M. Campos-Takaki, Electron. J. Biotechnol. 9 (2006) 400–406.

[4] A.I. El-Sheshtawy, M.E. Osman, A.A. Abo-ELnasr, A.S. Kobisy, Egypt. J. Pet. 24 (2015) 155–162.

[5] R.M.A. Díaz, I.M. Banat, B. Dolman, J. Winterburn, P.J. Martin, New Biotechnol. 32 (2015) 720–726.

[6] L.A. Sarubbo, J.M. Luna, R.D. Rufino, Chem. Eng. Trans. 43 (2015) 295–300.

[7] R.D. Rufino, J.M. Luna, G.M. Campos-Takaki, L.A. Sarubbo, Electron. J. Biotechnol. 17 (2014) 34–38.

[8] S. Mukherjee, P. Das, C. Sivapathasekaran, R. Sen, Lett. Appl. Microbiol. 48 (2009) 281–288.

[9] S.K. Satpute, I. M Banat, P.K. Dhakephalkar, A.G. Banpurkar, B.A. Chopade, Biotechnol. Adv. 28 (2010) 436–450.

[10] S.J. Varjani, D.P. Rana, S. Bateja, M.C. Sharma, V.N. Upasani, Int. J. Innovative Res. Sci. Eng. Technol. 3 (2014) 9205–9213.

[11] S.J. Varjani, V.N. Upasani, Bioresour. Technol. 221 (2016) 510–516.

[12] A.V. De Paula, J.C.S. Barboza, H.F. Castro, Quím. Nova. 28 (2005) 792–796.

[13] P.O. Carvalho, P.R.B. Campos, M.D.A. Noffs, J.G. Oliveira, M.T. Shimizu, D.M. Silva, Quím. Nova. 26 (2003) 75–80.

[14] R. Dalla-vecchia, M.G. Nascimento, V. Soldi, Quím. Nova. 27 (2004) 623–630.

[15] H.G. Dong, J. Zi, S.X. Yan, W. Ping, L. Ying, Y.H. Shuang, P.Z. Sui, Enzyme Microb. Technol. 75 (2015) 30–36.

[16] S.H. Ha, N.M. Hiep, Y.M. Koo, Biotechnol. Bioprocess Eng. 15 (2010) 126–130.

[17] U.H. Zaidan, M.B. A. Rahman, S.S. Othman, M. Basri, E. Abdulmalek, R.N.Z. Rahman, A.B. Salleh, Food Chem. 131 (2012) 199–205.

[18] N.L. Mai, K. Ahn, S.W. Baem, D.W. Shin, V.K. Morya, Y.M. Koo, Biotechnol. J. 9 (2014) 1565–1572.

[19] A.C.L. Torres, L.N. Lima, P.W. Tardioli, R. Sousa Jr, Reaction Kinetics, Mechanisms and Catalysis: React. Kinet. Mech. Catal. 130 (2020) 699–712.

[20] R.T. Hirales, R.M. Dionízio, S.S. Muñoz, C.A. Prado, R. Sousa Jr, S.S. Silva, J.C. Santos, Ultrason. Sonochem. 63 (2020) 1–9.

[21] B. Pratto, M.S.R. Santos-Rocha, A.A. Longati, R. Sousa Jr, A.J.G. Cruz, Bioresour. Technol. 297 (2020) 1–38.

[22] J. Ranković, J. Dodić, S. Dodić, S. Popov, Chem. Ind. Chem. Eng. Q. 15 (2009) 13–16.

[23] C. Marzo, A.B. Díaz, I. Caro, A. Blandino, Bioethanol Prod. Food Crops. (2019) 61–79.

[24] C.M.B. Moraes, Master Thesis, Campinas State University (2003).

[25] E.J. Parente, Tecbio. 1 (2003) 1–66.

[26] K.J.N. Ferreira, Master Thesis, Federal University of Maranhão (2014).

[27] B.P. Lavarack, G.J. Griffin, D. Rodman, Catal. Today. 63 (2000) 257–265.

[28] B. Girisuta, K. Dussan, D. Haverty, J.J. Leary, M.H.B. Hayes, Chem. Eng. J. 217 (2013) 61–70.

[29] V. Vescovi, J.B.C. Santos, P.W. Tardioli, Biocatal. Biotransform. 35 (2017) 298–305.

[30] F.W.W. Wagner, M.A. Dean, R.S. Motte, United States Patent, 4,983,731 (1991).

[31] R. Turton, R. C. Bailie, W. B. Whiting, J. A. Shaeiwitz, United States, 3 (2009).

[32] Sigma Aldrich. https://www.sigmaaldrich.com/BR/pt/search/lauryl- sulfat?focus=products&page=1&perPage=30&sort=relevance&term=lauryl%20sulfat&type=product [accessed 02 December 2021].

[33] R. C. F. Soares da Silva, D. G. de Almeida, P. P. F. Brasileiro, R. D. Rufino, J. M. de Luna, L. A. Sarubbo, Biodegradation. 30 (2018) 191–201.

ANA BÁRBARA MOULIN CANSIAN

PAULO WALDIR TARDIOLI

FELIPE FERNANDO FURLAN

RUY DE SOUSA JÚNIOR

Federal University of São Carlos, Department of Chemical Engineering

NAUČNI RAD

MODELOVANJE I SIMULACIJA ENZIMSKE PROIZVODNJE BIOSURFAKTANTA KORIŠĆENJEM KSILOZE I OLEINSKE KISELINE

Biosinteza estara šećera, molekula sa svojstvima biosurfaktanata, može se izvesti enzimski katalazovanom esterifikacijom šećera sa masnim kiselinama. Alternativa za smanjenje uticaja sirovina na konačnu cenu proizvodnje biosurfaktanata i ponovnu upotrebu industrijskog otpada je korišćenje ostataka iz industrije biljnih ulja kao izvora slobodnih masnih kiselina, kao što je oleinska kiselina, i lignoceluloznih ostataka iz proizvodnje etanola kao izvor šećera (ksiloza). U ovom scenariju, ovaj rad je imao za cilj modelovanje proizvodnje biosurfaktanata putem heterogene biokatalize korišćenjem lipaze, oleinske kiseline i ksiloze. Razdvajanje i prečišćavanje proizvoda izvršeno je korišćenjem niza taloženja (dodavanje etanola, vode i metil etil ketona). Simulacija je izvedena korišćenjem softvera EMSO (Environment for Modeling, Simulation, and Optimization) orijentisanog na jednačine, usklađenog sa CAPE-OPEN-om. Procenat biosurfaktanata u proizvodu je bio oko 86%, sa prinosom od 88% posle prečišćavanja. Što se tiče studije utroška energije, uočene su vrednosti od -604,1 kW i 137,6 kW toplote povezane sa hlađenjem i grejanjem, redom. Razvijeni matematički modeli uspešno su opisali proces. Početna ekonomska analiza procesa ukazuje na minimalnu prodajnu cenu biosurfaktanta od 72,37 USD/kg.

Ključne reči: biosurfaktanti, esterifikacija, modelovanje i simulacija, prečišćavanje, precipitacija.

CI&CEQ
Chemical Industry & Chemical Engineering Quarterly

Available online at
Association of the Chemical Engineers of Serbia AChE
www.ache.org.rs/CICEQ

Chem. Ind. Chem. Eng. Q. 28 (4) 277–286 (2022) CI&CEQ

DRAGOLJUB CVETKOVIĆ[1]
OLJA ŠOVLJANSKI[1]
ALEKSANDRA RANITOVIĆ[1]
ANA TOMIĆ[1]
SINIŠA MARKOV[1]
DRAGIŠA SAVIĆ[2]
BOJANA DANILOVIĆ[2]
LATO PEZO[3]

[1]University of Novi Sad, Faculty of Technology, Novi Sad, Serbia

[2]University of Niš, Faculty of Technology, Leskovac, Serbia

[3]Institute for General and Physical Chemistry, Belgrade, Serbia

SCIENTIFIC PAPER

UDC 582.282.23:66:519.87

AN ARTIFICIAL NEURAL NETWORK AS A TOOL FOR KOMBUCHA FERMENTATION IMPROVEMENT

Article Highlights

- A novel process modeling approach in kombucha production is conducted
- Box-Behnken experimental design was conducted based on three operating factors
- The ANN model showed to be adequate for the prediction of output kombucha factors

Abstract

Kombucha as a tea-based fermented beverage has become progressively widespread, mainly in the functional food market, because of health-improving benefits. As part of a daily diet for adults and children, kombucha was a valuable non-alcoholic drink containing beneficial mixtures of organic acids, minerals, vitamins, proteins, polyphenols, etc. The influence of the specific surface area of the vessel, the inoculum size, and the initial tea concentration as operating factors and fermentation time as output variable on the efficiency of kombucha fermentation was examined. The focus of this study is optimization and standardization of kombucha fermentation conditions using Box-Behnken experimental design and applying an artificial neural network (ANN) predictive model for the fermentation process. The Broyden-Fletcher-Goldfarb-Shanno iterative algorithm was used to accelerate the calculation. The obtained ANN models for the pH value and titratable acidity showed good prediction capabilities (the r^2 values during the training cycle for output variables were 0.990 and 0.994, respectively). Predictive ANN modeling has been proven effective and reliable in establishing the optimum kombucha fermentation process using the selected operating factors.

Keywords: experimental design, fermentation improvement, kombucha production, mathematical modeling.

High beverage consumption worldwide has opened the opportunity to develop different traditional drinks as part of the functional food concept. In recent years, scientific and industrial focus on the extremely valuable functional drink has further developed and improved kombucha fermentation [1]. The worldwide trends in kombucha production have focused on developing health-improving beverages based on different types of tea that contain an advantageous number of promising bioactive compounds. Optimization of the kombucha production process became the main topic of several researchers because of its large importance from the definition of the chemical composition of this functional beverage but also from an industrial point of view [2–5].

Kombucha is typically prepared by fermenting sweetened (with sucrose) black or green tea inoculated with tea fungus pellicle or previously fermented broth at 100-200 mL/L. During kombucha fermentation, the formation of a floating pellicle of microbial cellulose is expected and very typical [3]. As a result, reduced cholesterol levels and blood pressure, influenced weight loss, improved liver and gastric functions, reduced kidney calcification, and increased vitality can be some health-improving benefits attributed to kombucha consumption [4–6].

The tea fungus is a consortium of acetic acid bac-

Correspondence: A. Ranitović, University of Novi Sad, Faculty of Technology Novi Sad, Bulevar cara Lazara, 1, 21000 Novi Sad, Serbia.
E-mail: a.ranitovic@uns.ac.rs
Paper received: 13 October, 2021
Paper revised: 4 February, 2022
Paper accepted: 3 March, 2022

https://doi.org/10.2298/CICEQ211013002C

teria (AAB) (*Gluconacetobacterxylinum*, previously known as *Acetobacter xylinus* and, more recently, as *Komagataeibacter xylinus*, is the primary and best-studied bacteria in kombucha) and yeasts (species of the genera *Saccharomyces*, *Torulopsis*, *Pichia*, *Brettanomyces*, *Zygosaccharomyces*, *Candida*, and *Saccharomycoides*) [7–11]. It is well known that the microbial community may vary between different kombucha cultures across the globe depending upon the source of the inoculum used. The role of yeasts in kombucha fermentation is to hydrolyze sucrose from the cultivation medium to glucose and fructose and metabolize these monosaccharides to ethanol, which is further oxidized to acetic acid by AAB. However, AAB cannot uptake sucrose alone because of the lack of enzymes for the extracellular hydrolysis of sucrose or its transport into the cell. Also, AAB uses yeast-derived glucose to synthesize gluconic acid and bacterial cellulose in the form of a pellicle, commonly described as the "fungus" [7,12].

Kombucha fermentation requires around seven days statically under aerobic conditions at temperatures between 25 °C and 30 °C [13]. The initial phase of this fermentation process is reflected in high sucrose levels but low acidity. On the other hand, further steps include a gradual decrease in oxygenation. This occurrence results from forming a cellulose layer on top of the cultivation liquid, the oxygen consummation, and the accumulation of organic acids (acetic acid, gluconic acid, etc.) produced by tea fungus [14–15]. At the end of kombucha fermentation, the system can be described with a well-structured cellulose layer on the top, high concentration of yeasts and AAB (106–108 CFU/mL), lower substrate concentration, and high acidity [16]. Creating a more controllable fermentation process and optimizing the operating factors require examining the diversity and role of each microbial group, the dynamics of the microbial population, and all changes in the system reflected through the quality of the final product [3]. Microbial interactions during kombucha fermentation strongly impact substrate consumption and metabolic production (e.g., ethanol produced by yeasts can harm the growth of some microorganisms, organic acids production by AAB can induce acidic stress of other microbiota, the pH changes from 5-7.0 to 2-4.0 after 7 days of fermentation, etc.) [15].

Although the type of tea is recognized as one of the essential factors in kombucha production, the most significant impact of the fermentation process is operating factors. The key factor of kombucha fermentation is assumed to be the oxygen amount in the culture medium, which is necessary for AAB proliferation. The dimensions of the fermentation vessel and the specific interfacial area can influence the oxygen level during fermentation which is a crucial operating parameter [17]. Furthermore, under static conditions, the amount of dissolved oxygen is inevitably the function of the size of the interfacial surface [18]. In the condition of a low oxygen concentration and the acid production by AAB, the pH value is above 4, which can induce lactic acid bacteria (LAB) growth and lactic acid production [3]. De Filippis *et al*. [18] reported that incubation time and temperature also influence the product's microbial activity and chemical characteristics.

The effect of many operating factors and conditions and the interaction between them on the efficiency of the fermentation process can be analyzed by different mathematical tools. For example, response surface methodology (RSM) and other experimental designs (e.g., Box-Behnken, Plackett-Burman, Taguchi design, etc.) can be effective tools for optimizing the targeted process and explaining the individual and combined effect of the independent variables [19-20]. Using adequate mathematic analysis can determine and simultaneously explain the optimization of kombucha fermentation and set up further steps during the scale-up of kombucha production [21]. Only a few scientific studies and craft production deal with scale-up and more controllable fermentation processes during kombucha production. It is necessary to optimize operating factors and create the next generation of kombucha as part of the functional food field. In this way, kombucha fermentation will be more predictable and economical for industrial production [3].

The objective of this study was to investigate the possibility of predicting pH value and titratable acidity based on the specific surface area of the vessel (SSAV), the inoculum size (Inn), and the initial concentration of tea (ICT) using artificial neural network modeling. In addition, Time was an additional output, as one of the variables defined after achieving optimal pH value and titratable acidity and used for further mathematical modeling.

MATERIAL AND METHODS

Tea fungus

Fermentation was performed using the local household tea fungus culture. Previous studies showed that it contained at least five yeast strains (*Saccharomycodes ludwigii*, *S. cerevisiae*, *S. bisporus*, *Torulopsis* spp., and *Zygosaccharomyces* spp.) and two bacteria of the *Acetobacter* genera [22–23].

Fermentation conditions

The cultivation medium uses sweetened black tea

(70 g sucrose/L of tap water). Briefly, 0.15%, 0.3%, or 0.45% (w/v) of black tea ("Fructus," Bačka Palanka, Republic of Serbia) was added to boiled tap water and removed after 15 min by filtration. After reaching room temperature, the tea base was inoculated with 2.5%, 5%, or 10% (v/v) of the fermentation broth from the previous fermentation (five-day fermentation until optimal acid content of 4– 4.5 g/L is reached) obtained at 28 ± 1 °C without stirring. The cultivation medium was transferred into cylindrical glass vessels whose geometric characteristics are shown in Table 1. To get different values of the specific surface area of the vessel, the volume of the cultivation medium in the vessels was varied. The specific surface area of the vessel presents the ratio of the free area (cross-sectional area of the vessel) and the volume of the substrate. The sterile gauze was placed on a glass vessel to prevent contamination during cultivation. The medium was incubated at 28 ± 1 °C without stirring. All experiments were performed in three independent replicates, and all obtained values are represented as the arithmetic values of individual measurements.

Table 1. Characteristics of cylindrical glass vessels and specific surface area of the vessel (SSAV)

Vessel characteristics		The volume of cultivation medium	SSAV*
Volume	Diameter		
(L)	(cm)	(L)	(cm^{-1})
0.72	8	0.17	0.30
0.72	8	0.33	0.15
5	16	3.30	0.06

* The ratio of the free area (cross-sectional area of the vessel) and the volume of the substrate.

Sampling

A sampling of the fermentation medium was performed every day until the selected output (pH value and TA) did not show the optimal acid content until the end of fermentation. Sampling was done only once in the specified time to avoid the potential contamination during a further fermentation process. During the fermentation process, pH value and TA were determined.

Methods of Analysis

The pH values were measured using an electronic pH meter (HI 99181, HANNA Instruments, Woonsocket, USA) calibrated at pH 4.0 and 7.0. The titratable acidity (TA) was determined according to Jacobson [24]. After removing CO_2 (during 30-second treatment in an ultrasound bath, B-220, Branson Company, Shelton, USA) from the fermentation broth, an aliquot was taken and titrated with 0.1M NaOH. The TA was expressed in grams of acetic acid per liter of the sample.

Experimental design

The pH value and titratable acidity were predicted based on three operation factors: the SSAV, the Inn, and the ICT. These three operating factors (X1 – SSAV, X2 – Inn, and X3 – ICT) were independent factors in the selected Box-Behnken experimental design. The pH value and titratable acidity were chosen as the dependent factors. The experimental design is given as % in Table 2 with three levels for each independent factor, coded as -1, 0, and +1, corresponding to the lower, middle, and higher levels, respectively. The response surface method was used to evaluate the influence of the MATH operating factors on the kombucha fermentation process. The impact of the examined factors and their interaction was studied using response surface plots to present the influence of fermentation time and initial tea concentration on pH value and TA of kombucha during fermentation. Time was an additional output as one of the variables defined after achieving optimal pH value and titratable acidity and used for further mathematical modeling.

ANN modeling

A multi-layer perceptron model (MLP), which consisted of three layers (input, hidden, and output), was used for modeling an artificial neural network model (ANN) for the prediction of pH value and TA based on three input variables: SSAV, Inn, ICT, as well as on one output, i.e., Time which values defined achieving optimal acidity for kombucha production. In the known literature, the ANN model was proven as quite capable of approximating nonlinear functions [25–27]. Before the calculation, both input and output data were normalized to improve the behavior of the ANN. During this iterative process, input data were repeatedly presented to the network [28–29]. Broyden -Fletcher-Goldfarb-Shanno (BFGS) algorithm was used as an iterative method for solving unconstrained nonlinear optimization during the ANN modeling.

The experimental database for ANN was randomly divided into training, cross-validation, and testing data (with 70%, 15%, and 15% of experimental data, respectively). The training data set was used for the learning cycle of the ANN and the evaluation of the optimal number of neurons in the hidden layer and the weight coefficient of each neuron in the network. A series of different topologies

were used, in which the number of hidden neurons varied from 5 to 20, and the training process of the network was run 100,000 times with random initial values of weights and biases. The optimization process was performed based on validation error minimization. It was assumed that successful training was achieved when learning and cross-validation curves approached zero.

Coefficients associated with the hidden layer (weights and biases) were grouped in matrices W_1 and B_1. Similarly, coefficients related to the output layer were grouped in matrices W_2 and B_2. It is possible to represent the neural network by using matrix notation (Y is the matrix of the output variables, f_1 and f_2 are transfer functions in the hidden and output layers, respectively, and X is the matrix of input variables [30]:

$$Y = f_1(W_2 \cdot f_2(W_1 \cdot X + B_1) + B_2) \quad (1)$$

Weight coefficients (elements of matrices W_1 and W_2) were determined during the ANN learning cycle, which updated them using optimization procedures to minimize the error between the network and experimental outputs [28, 30–32], according to the sum of squares (SOS) and BFGS algorithm, used to speed up and stabilize convergence [33]. Finally, the coefficients of determination were used as factors to check the performance of the obtained ANN model. Statistical analyses were done using Statistica software v. 13.2 (Dell, Round Rock, Texas, USA).

Sensitivity analysis

Yoon's interpretation method was applied based on the connection weights partitioning of the developed ANN to determine the relative influence (RI) of the SSAV, Inn, ICT, and Time on pH value and titratable acidity. The following equation developed by Yoon et al. [34] was used:

$$RI_{ij} = \frac{\sum_{k=0}^{n}\left(w_{ik} \cdot w_{kj}\right)}{\sum_{i=0}^{m}\left|\sum_{k=0}^{n}\left(w_{ik} \cdot w_{kj}\right)\right|} \cdot 100\% \quad (2)$$

where RI_{ij} is the relative importance of the i-th input variable on the j-th output, w_{ik} is the weight between the i-th input and the k-th hidden neuron, and w_{kj} is the weight between the k-th hidden neuron and the j-th output.

The accuracy of the model

The numerical verification of the developed model was tested using the coefficient of determination (r^2), reduced chi-square (χ^2), mean bias error (MBE), root mean square error (RMSE) and mean percentage error (MPE). These commonly used parameters can be calculated as follows [35]:

$$\chi^2 = \frac{\sum_{i=1}^{N}(x_{\exp,i} - x_{pre,i})^2}{N - n},$$
$$RMSE = \left[\frac{1}{N} \cdot \sum_{i=1}^{N}(x_{pre,i} - x_{\exp,i})^2\right]^{1/2}, \quad (3)$$
$$MBE = \frac{1}{N} \cdot \sum_{i=1}^{N}(x_{pre,i} - x_{\exp,i}),$$
$$MPE = \frac{100}{N} \cdot \sum_{i=1}^{N}\left(\frac{\left|x_{pre,i} - x_{\exp,i}\right|}{x_{\exp,i}}\right)$$

where $x_{exp,i}$ stands for the experimental values and $x_{pre,i}$ are the predicted values calculated by the model, N and n are the number of observations and constants, respectively.

RESULTS AND DISCUSSION

Kombucha fermentation was studied to determine the influence of the SSAV, the Inn, and ICT on the efficiency of kombucha fermentation through pH value and titratable acidity (TA). Additionally, an important factor was also final Time, which was observed after achieving optimal acidity in the system. Namely, to obtain a pleasantly sour beverage, fermentation should be terminated when TA of fermentation broth reaches 4-4.5 g/L, which is confirmed by kombucha consumers [17]. The reason for the selection of incubation time is that an optimum fermentation time is required for the production of kombucha with pleasant flavor and taste, as well as further scaling-up and potential industrialization of kombucha production. Furthermore, longer fermentation produces high levels of acids (like mild vinegar) that may pose potential risks when consumed [36]. For this purpose, Box Behnken design was performed for all mentioned operating factors of the fermentation process. Table 2 summarizes the used experimental design and the obtained results.

Before further mathematical analysis, it can be observed based on the obtained results that the specific interfacial surface area of the vessel has a particular influence on acetic acid synthesis during kombucha fermentation. Furthermore, in the vessels with a specific interfacial surface area is 0.3 cm^{-1}, an optimal acidity of kombucha was achieved practically twice as faster compared to vessels with a specific area of 0.06 cm^{-1} under the same other experimental factors (by comparing experiments 5 and 6, as well as 7 and 8 in Table 2). Cvetković *et al.* [37] previously established a mathematical model to ensure the scaling-up process of kombucha fermentation, which can be quite complex and should consider the specific interfacial area as the main variable. Similar conclusions are reported by Junker [38] and Villarreal-Soto *et al.* [39], which demonstrated the same behavior during the variability

of this operating parameter. Furthermore, without agitation and aeration, the kombucha fermentation process in cylinder vessels strongly depends on the specific surface area, which is indicative of this study's obtained results. Therefore, it can be concluded that an effective process can ensure vessels with a specific surface area greater than 0.15 cm^{-1} provide a sufficient oxygen supply by diffusion through the medium surface area.

The influence of the inoculum size on the fermentation process is primarily observed in the slightly increased acidity of the medium after inoculation. A higher concentration of total acids was recorded in the cultivation medium with a larger inoculum size by studying fermentation processes through the Box-Behnken experimental design. As a result, the time required to obtain the beverage of optimal acidity was shorter. However, slightly higher acidity in the fermentation broth has a beneficial effect on the physiological activity of yeasts and AAB [3]. Acid's presence stimulates yeasts to produce ethanol, which is then used by acetic acid bacteria to grow and produce more acetic acid [40]. Lončar *et al.* [41] reported that fermentation rate was slightly affected by inoculums concentrations ranging between 10 and 15% (v/v). Therefore, although increasing inoculum size can positively affect the productivity of kombucha fermentation, it can be concluded that there is also a negative impact on the economy of kombucha production at the same time. According to the obtained results, it can be summarized that the initial tea concentration had a specific influence since the fermentation will be finalized using any of the tested concentrations of herbal. On the other hand, the fermentation will be finalized at different points in time using a different combination of tested inputs. Briefly, the fermentation time can be shortened on 4 incubation days by applying optimized values of SSAV, Inn, and ICT.

ANN modeling

Based on experimental results obtained from the experimental design, the final fermentation time to reach optimal acidity was included as one of the data for further statistical analysis. This step provided another aspect of examination of operating factors of kombucha fermentation. There have been no published results on the application of ANNs for predictive modeling of kombucha production based on the pH and TA values. Despite the lack of results in this field, ANN models are recognized in bioprocesses as a good modeling tool. They offer an empirical explanation of the problems from experimental data and can conduct complex systems with nonlinearities and interactions between decision variables [20]. The ANN model is developed to accurately predict pH and TA values based on the selected factors. The obtained number of hidden neurons in the network was 8 (network MLP 4-8-2). In this way, very high values of r^2 (during the training cycle, the r^2-values for the output variables were: above 0.99) were gained, shown in Table 3. The acquired optimal neural network model showed a good generalization capability for the tested experimental data. However, the obtained ANN model for the prediction of output variables was complex (58 weights-biases) because of the high nonlinearity of the observed system [42].

The three-dimensional surface plots were created (Figure 1) to present the influence of fermentation time and initial tea concentration on pH value and TA of kombucha fermentation. It can be observed that minimal initial tea concentration (0.15%) provided sufficient nitrogen compounds and mineral elements necessary for kombucha fermentation under stationary fermentation conditions. However, further tests should confirm whether this concentration of tea is the final minimal amount that ensures the efficiency of kombucha fermentation. As the time and temperature of fermentation are used in kombucha production, the tea and sugar proportions can vary according to each region or consumer preferences (2017).

According to Jayabalan *et al.* [4], the standard procedure for kombucha production implies the use of 50 g sucrose and 5 g tea leaves with 1 L boiled tap water. The tea is removed by filtration after 5 min, and after cooling to room temperature, the medium is inoculated with 24 g of the tea fungus culture. Kallel *et al.* [42] used even 12 g/L of green or black tea with 5 min of infusion to prepare the kombucha cultivation medium. After 15 days of fermentation, the TA for green tea kombucha was 5.4 g/L and 8.0 g/L for black tea kombucha. Generally, the same differences in TA, process duration, and cell counts in kombucha beverages obtained in different studies are expected because of inoculums (tea fungus culture) from other locations. The variations could be due to geographic, climatic, and cultural conditions and local species of wild yeasts and bacteria or, possibly, cross-contamination between cultures [8]. Based on the unattainable adequate TA and pH values, it can also be concluded that, despite the high contents of C and N sources, the fermentation process with a high tea concentration can be slower and, therefore, economically less acceptable.

The fermentation time in kombucha production is a variable parameter demonstrated in this study (Table 2, Figure 1). Based on the obtained results (Figure 1a), it is evident that the adequate pH value was achieved

Table 2. Box-Behnken design with three independent factors (SSAV - Specific surface area of the vessel (cm^{-1}), Inn - Inoculum size (v/v), and ICT - Initial concentration tea (w/v) and the obtained results for pH and titrable acidity (TA, g/L)

	Coded factor level			Varied factor value			Output	Fermentation time, days								
	X_1	X_2	X_3	SSA	Inn	ITC		0	1	2	3	4	5	6	7	8
1	-1	-1	0	0.06	2.5	0.3	pH	6.05±0.01	5.08±0.02	4.26±0.0	3.46±0.01	3.17±0.00	3.14±0.0	3.04±0.00	-	-
							TA	0.00±0.0	0.15±0.0	0.55±0.07	1.83±0.07	3.27±0.12	4.18±0.04	5.06±0.01	-	-
2	1	-1	0	0.3	2.5	0.3	pH	5.86±0.03	5.34±0.01	4.51±0.01	3.94±0.00	3.34±0.0	3.16±0.1	-	-	-
							TA	0.00±0.0	0.04±0.2	0.14±0.04	0.57±0.03	1.96±0.04	2.77±0.3	-	-	-
3	-1	1	0	0.06	10	0.3	pH	4.61±0.03	3.93±0.04	3.34±0.0	3.14±0.06	2.99±0.00	2.90±0.01	-	-	-
							TA	0.00±0.0	0.43±0.01	1.91±0.04	3.53±0.00	4.86±0.00	6.56±0.03	-	-	-
4	1	1	0	10	0.3	10	pH	4.5±0.0	4.21±0.0	3.42±0.0	2.99±0.01	2.78±0.02	-	-	-	-
							TA	0.00±0.0	0.12±0.03	1.23±0.01	3.47±0.11	8.58±0.04	-	-	-	-
5	-1	0	-1	0.06	5	0.15	pH	4.70±0.01	4.27±0.01	4.20±0.01	3.61±0.2	3.38±0.10	3.13±0.00	-	-	-
							TA	0.00±0.0	0.04±0.2	0.26±0.31	1.06±0.01	1.97±0.09	3.94±0.01	-	-	-
6	1	0	-1	0.3	5	0.15	pH	5.15±0.06	4.56±0.01	3.88±0.0	3.29±0.00	2.89±0.02	-	-	-	-
							TA	0.00±0.0	0.10±0.04	0.49±0.27	2.65±034	6.99±0.81	-	-	-	-
7	-1	0	1	0.06	5	0.45	pH	4.70±0.04	4.09±0.01	4.26±0.0	3.79±0.00	3.46±0.01	3.12±0.00	-	-	-
							TA	0.00±0.0	0.12±0.14	0.26±0.06	0.89±0.31	1.98±0.22	3.99±0.01	-	-	-
8	1	0	1	0.3	5	0.45	pH	5.14±0.11	4.57±0.0	3.88±0.07	3.28±0.00	2.89±0.10	-	-	-	-
							TA	0.00±0.0	0.10±0.13	0.49±0.11	2.65±0.06	6.99±0.81	-	-	-	-
9	0	-1	-1	0.15	2.5	0.15	pH	5.53±0.01	5.17±0.0	435±0.0	3.44±0.0	3.10±0.00	2.84±0.00	2.72±0.03	-	-
							TA	0.00±0.0	0.03±0.2	0.15±017	0.72±0.2	2.53±1.24	6.84±0.51	9.94±0.67	-	-
10	0	1	-1	0.15	10	0.15	pH	5.53±0.04	5.31±0.0	4.81±0.0	4.37±0.0	3.55±0.04	3.29±0.00	3.17±0.00	3.00±0.00	2.94±0.00
							TA	0.00±0.0	0.10±0.09	0.16±0.01	0.47±0.02	1.10±0.07	2.65±0.03	2.69±0.16	4.11±0.01	5.78±0.23
11	0	-1	1	0.15	2.5	0.45	pH	6.05±0.01	6.02±0.00	5.08±0.01	4.43±0.0	3.99±0.06	3.09±0.07	2.86±0.00	-	-
							TA	0.00±0.0	0.002±0.0	0.04±0.2	0.14±0.04	0.44±0.07	3.44±0.10	6.91±0.40	-	-
12	0	1	1	0.15	10	0.45	pH	4.46±0.03	4.32±0.01	3.56±0.03	2.89±0.06	2.81±0.09	2.74±0.00	2.60±0.05	-	-
							TA	0.0±0.0	0.033±0.1	0.62±0.27	2.03±0.1	5.15±0.01	8.69±0.21	11.09±0.2	-	-
13	0	0	0	0.15	5	0.3	pH	4.70±0.11	4.24±0.05	4.35±0.0	3.81±0.0	3.48±0.03	3.13±0.0	-	-	-
							TA	0.00±0.0	0.12±0.02	0.24±0.07	0.69±0.11	1.89±0.02	3.05±0.02	-	-	-
14	0	0	0	0.15	5	0.3	pH	4.70±0.01	4.24±0.0	4.35±0.0	3.81±0.1	3.48±0.00	3.13±0.01	-	-	-
							TA	0.00±0.0	0.12±0.06	0.24±0.1	0.69±0.03	1.89±0.13	3.05±0.06	-	-	-
15	0	0	0	0.15	5	0.3	pH	4.70±0.04	4.24±0.01	4.35±0.01	3.81±0.05	3.5±0.01	3.13±0.00	-	-	-
							TA	0.00±0.0	0.12±0.02	0.24±0.03	0.69±0.05	1.9±0.03	3.05±0.07	-	-	-

Table 3. Artificial neural network model summary (performance and errors)

Network name	Performance*			Error			Training algorithm	Error function	Hidden activation	Output activation
	Train.	Test.	Valid.	Train.	Test.	Valid.				
MLP 4-8-2	0.992	0.902	0.990	0.053	0.723	0.052	BFGS 56	SOS	Tanh	Logistic

* Performance term represents the coefficients of determination, while error terms indicate a lack of data for the ANN model.

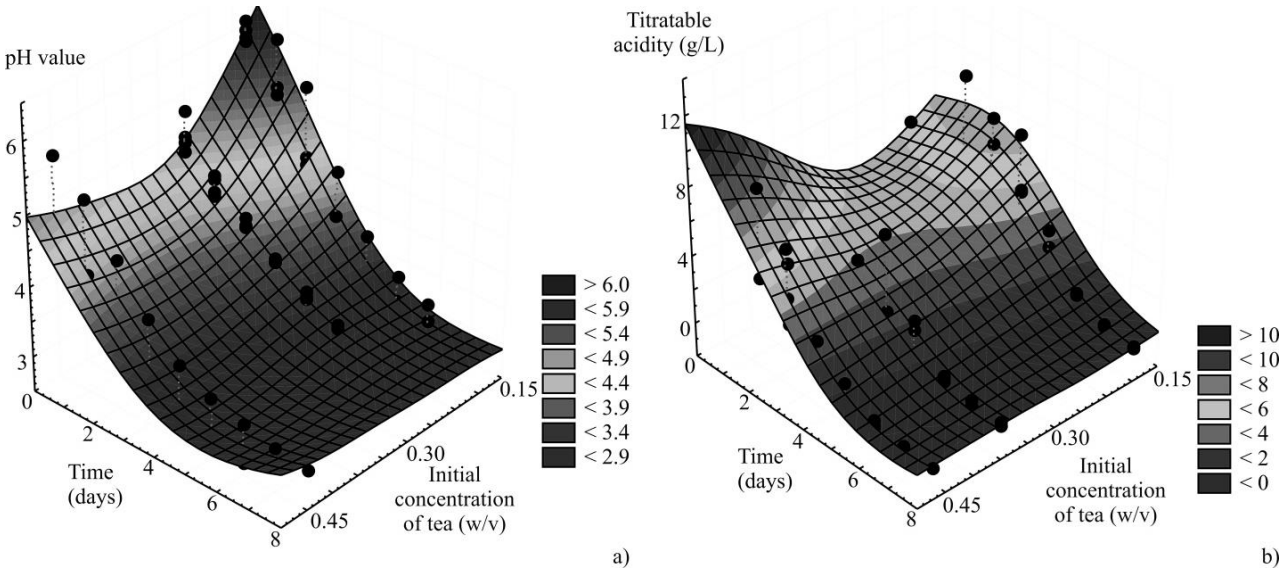

Figure 1. The influence of time (days) and initial concentration of tea on the pH value and titratable acidity (g/L) (3D surfaces - predicted values, black dots - experimental values).

after 4 days of fermentation and at any value of initial tea concentration. According to the results presented in the three-dimensional plot (Figure 1b), it can be concluded that the TA value is equally achieved at medium values of fermentation time and any values of tea concentration. The obtained result for pH and TA correlated with the results of Cvetković *et al.* [37], which suggested that after three days of incubation, the pH value of 3.21 and TA value of 4.32 g/L can be achieved. The accuracy of the ANN model could be visually assessed by the dispersion of points from the diagonal line in the graphics presented in Figure 2. For the ANN model, the predicted values were very close to the measured values in most cases, in terms of r^2 values. Therefore, SOS obtained with the ANN model were of the same order of magnitude as experimental errors for the pH value and TA. Table 4 presents the elements of matrix W_1 and vector B_1 (shown in the bias column) and the elements of matrix W_2 and vector B_2 (bias) for the hidden layer used for Eq. (2). The goodness of fit between experimental measurements and model-calculated outputs, represented as ANN performance (sum of r^2 between measured and calculated output variables), during training, testing, and validation steps, are shown in Table 5.

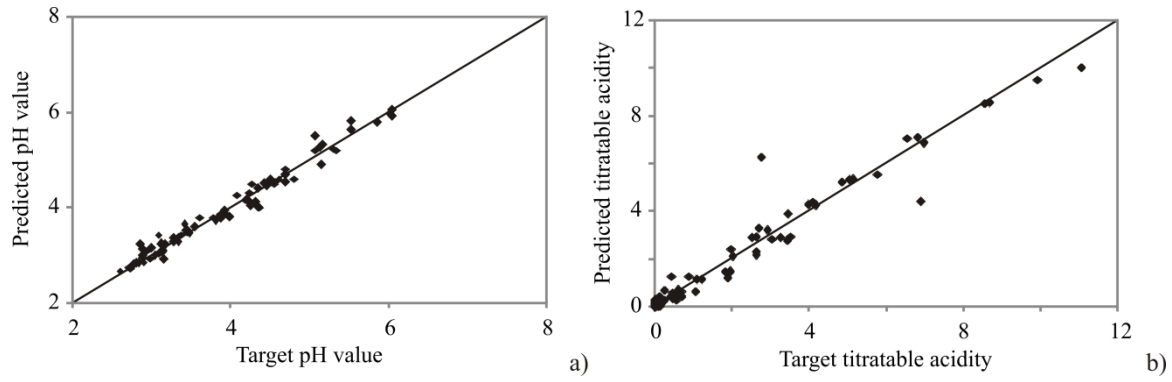

Figure 2. Comparison between experimental and calculated pH values and titratable acidity (g/L).

Table 4. Elements of matrix W_1 and vector B_1 (presented in the bias column)

Inputs	1	2	3	4	5	6	7	8	
SSAV	-0.912	2.235	-0.674	0.279	1.357	-5.377	-0.295	0.545	
Inn	-0.538	-3.939	-1.484	6.261	-3.636	1.385	1.628	0.344	
ICT	1.231	-0.655	-0.325	-1.273	0.818	2.114	-1.333	0.690	
Time	0.242	-3.318	0.025	4.048	-2.839	-1.876	0.176	-2.758	
Bias	-0.297	0.046	-0.272	0.786	3.328	3.201	-1.161	0.457	
Outputs	1	2	3	4	5	6	7	8	Bias
pH value	0.381	1.503	-1.098	-3.438	2.105	1.092	3.240	0.808	2.962
Titratable acidity	0.808	-3.533	0.334	1.703	-2.594	-2.677	-3.506	-1.880	-5.347

Table 5. The "goodness of fit" tests and residual analysis for the developed ANN model

Output variable	χ^2	RMSE	MBE	MPE	SSE	AARD	r^2	Skew	Kurt	Mean	StDev	Var
pH value	0.02	0.15	-0.004	2.73	1.96	13.05	0.97	0.06	1.08	-0.004	0.15	0.02
Titratable acidity	0.29	0.53	0.007	38.75	26.66	25.51	0.96	-1.91	23.88	0.007	0.54	0.29

A high r^2 is indicative that the variation was accounted for and that the data fitted the proposed model satisfactorily [43]. The residual analysis of the developed model is presented in Table 5. The ANN model reasonably predicted experimental variables for a broad range of process variables. For the ANN model, the predicted values were very close to the measured values in most cases, in terms of r^2 values. SOS values obtained with the ANN model were of the same order of magnitude as experimental errors for output variables reported in the literature [28, 32]. The ANN model had an insignificant lack of fit tests, which means the model satisfactorily predicted output variables. A high r^2 indicates that the variation was accounted for and that the data adequately fitted the proposed model [44–45].

Global sensitivity analysis- Yoon's interpretation method

This section studied the influence of SSAV, Inn, ICT, and Time on the relative importance (RI) of pH value and TA. According to Figure 3, Time and Inn were the most influential factors with the relative importance of -47.26% and -44.08%, respectively, for the pH value calculation. In comparison, the relative influence of the mentioned factors was 55.32% and 35.59%.

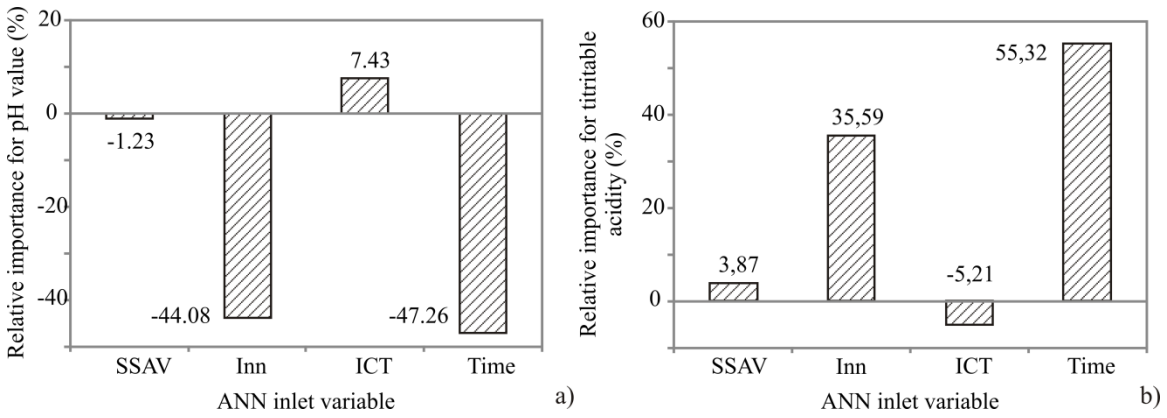

Figure 3. The relative importance of operating parameters on pH value and titratable acidity determined using the Yoon interpretation method.

CONCLUSION

An investigation of the kombucha fermentation optimization was performed to determine the possibility of predicting the pH value and TA based on three input variables: SSAV, Inn, ICT, as well as one output, i.e., Time which was defined as achieving the optimal acidity in the system, using the ANN model. The ANN model was shown to be adequate for predicting output variables (the r^2 values during the training cycle for these variables were: 0.990 and 0.994, respectively). In summary, Box Benhken's experimental design was applied, and predictive ANN modeling was developed to establish the optimum kombucha fermentation process to achieve the effective fermentation of the kombucha beverage. Effective kombucha fermentation can be performed using vessels with a specific surface area greater than 0.15 cm^{-1}, which provides sufficient oxygen supply by diffusion through the medium surface area. The final product can be obtained after 4 days of fermentation and at any tested value of initial tea concentration. Furthermore, the scale-up process from a laboratory scale to a commercial product is a challenge because of the difficulty of optimizing the factors which may influence the scaling process during fermentation. Therefore, more scientific research in the optimization of the operating factors should be done to establish effective fermentation and production of a functional beverage.

In the following steps of this investigation, other essential factors for monitoring kombucha fermentation have to be tested in the same way as reported in this study. For example, the selection of additional factors can be directed to a concentration of residual sugar and alcohol and the evolution of carbon dioxide. In addition, testing as many characteristics of the fermented product and determining their correlation with operation factors leads to obtaining functional beverages that consumers will quickly accept. Furthermore, understanding the type and number of microbiota present in the tea fungus culture can explain specific influence on kombucha fermentation and tested factors in this research.

Acknowledgment

The Ministry of Education, Science, and Technological Development of the Republic of Serbia (contract no. 451-03-68/2022-14/200134) is gratefully acknowledged.

REFERENCES

[1] J. Kim, K. Adhikari, Bevarages 6 (2020) 1–19.

[2] J. Islam, Y. Kabir, Yects and Mechanisms of Antioxidant-Rich Functional Beverages on Disease Prevention, Woodhead Publishing: Duxford, UK (2019) p. 118.

[3] D. Laureys, S. Britton, J. De Clippeleer, J. Am. Soc. Brew. Chem.78 (2020) 165–174.

[4] R. Jayabalan, R.V. Malbaša, M. Sathishkumar, Kombucha Tea: Metabolites. In Fungal Metabolites. Springer International Publishing (2017) p. 965–978.

[5] M. Coton, A. Pawtowski, B. Taminiau, G. Burgaud, F. Deniel F, FEMS Microb. Ecol.93 (2017) 1–16.

[6] J.M. Kapp, W. Sumner, A. Ann. Epidemiol.30 (2019) 66–70.

[7] C.J. Greenwalt, K.H. Steinkraus, R.A. Ledford, J. Food Prot.63 (2000) 976–981.

[8] Al. Teoh, G. Heard, J. Cox, Int. J. Food Microbiol.95 (2004) 119–126.

[9] S.C. Chu, C. Chen, Food Chem.98 (2006) 502–507.

[10] Y. Yamada, P. Yukphan, Int. J. Food Microbiol.125 (2008) 15–24.

[11] Y. Yamada, P. Yukphan, H.T. Lan Vu, Y. Muramatsu, D. Ochaikul, S. Tanasupawat, Y. Nakagawa, J. Gen Appl. Microbiol.58 (2012) 397–404.

[12] C.P. Kuerzman, C.J. Robnett, E. Basehoar-Powers, FEMS Yeast Res.1 (2001) 133–138.

[13] S. Chakravorty, S. Bhattacharya, D. Bhattacharya, S. Sarkar, R. Gachhui, Kombucha: A Promising Functional Beverage Prepared from Tea, Sawston, Cambridge (2019).

[14] Z.W. Yang, B.P. Ji, F. Zhou, B. Li, Y. Luo, L. Yang, T. Li, J. Sci. Food Agric.89 (2009) 150–156.

[15] K. Neffe-Skocinska, B. Sionek, I. Scibisz, D. Kolozyn-Krajewska, Cyta J. Food 15 (2017) 601–607.

[16] A.J. Marsh, O. O'Sullivan, C. Hill, R.P. Ross, P.D. Cotter, Food Microbiol.38 (2014) 171–178.

[17] D. Cvetković, S. Markov, M. Djurić, D. Savić, A. Velićanski, J. Food Eng.85 (2008) 387–392.

[18] F. De Filippis, A.D. Troise, P. Vitaglione, D. Ercolini, Food Microbiol.73 (2018) 11–16.

[19] A. Vidaković, O. Šovljanski, A. Ranitović, D. Cvetković, S. Markov, Acta Period. Technol.48 (2017) 295–305.

[20] O. Šovljanski, A. Tomić, L. Pezo, A. Ranitović, S. Markov, J. Serb. Soc. Chem.85 (2020) 1417–1427.

[21] P. Manivasagan, J. Venkatesan, K. Sivakumar, S. Kim, Microb. Res.169 (2020) 262–278.

[22] S. Markov, R. Malbaša, M. Hauk, D. Cvetković, Acta Period. Technol. 32 (2001) 133–138.

[23] A. Velićanski, D. Cvetković, S. Markov, Rom. Biotechnol. Lett. 18 (2012) 8034–8042.

[24] J.L. Jacobson, Introduction to Wine Laboratory Practices and Procedures. Springer Science, New York (2006).

[25] D.P. Johnson, A. Stanforth, V. Lulla, G. Luber, Appl. Geogr. 35 (2012) 23–31.

[26] T.S. Yun, Y.J. Jeong, T.S. Han, K.S. Youm, Energ. Buildings 61 (2013) 125–132.

[27] J.P.C. Kleijnen, Design and Analysis of Simulation Experiments. Springer Proceedings in Mathematics and Statistics, Italy (2018).

[28] T. Kollo, D. von Rosen, Advanced Multivariate Statistics with Matrices, Springer, Berlin (2005).

[29] L. Pezo, B.Lj. Ćurčić, V.S. Filipović, M.R. Nićetin, G.B. Koprivica, N.M. Mišljenović, Lj.B. Lević, Hem. Ind.67 (2013) 465–475.

[30] C.I. Ochoa-Martínez, A.A. Ayala-Aponte, LWT40 (2007)

638–645.
[31] L.A. Berrueta, R.M. Alonso-Salces, K. Héberger, J. Chromatogr. A1158 (2007) 196–214.
[32] M. Doumpos, C. Zopounidis, Eur. J. Oper. Res. 209 (2011) 203–214.
[33] B.J. Taylor, Methods and Procedures for the Verification and Validation of Artificial Neural Networks, Springer Science and Business Media, New York (2006).
[34] Y. Yoon, G. Swales, T.M. Margavio, J. Oper. Res. Soc.44 (1993) 51–60.
[35] O. Šovljanski, L. Pezo, A. Tomić, A. Ranitović, D. Cvetković, S. Markov, J. Basic Microb.61 (2021) 835–848.
[36] G. Sreeramulu, Y. Zhu, W. Knol, J. Agri. Food Chem.48 (2000) 2589–2594.
[37] D. Cvetković, A. Ranitović, D. Savić, N. Joković, A. Vidaković, L. Pezo, S. Markov, Pol. J. Food Nutr. Sci. 69 (2019) 407–415.
[38] B.H. Junker, J. Biosci. Bioeng. 97 (2004) 347–364.
[39] S. Villarreal-Soto, S. Beaufort, J. Bouajila, J.P. Souchard, T. Renard, S. Rollan, P. Taillandier, Process Biochem. 83 (2019) 44–54.
[40] M.J. Santos, Kombucha: Caracterizaçao da microbiota e desenvolvimento de novos produtos alimentares para uso em restauraçao. Universidade Nova de Lisboa, Lisboa (2016).
[41] E. Lončar, K. Kanurić, R. Malbaša, M.S. Đurić, S.D. Milanović,.CICEQ 20 (2014) 345–352.
[42] L. Kallel, V. Desseaux, M. Hamdi, P. Stocker, E.H. Ajandouz, Food Res. Int. 49 (2012) 226–232.
[43] D.C. Montgomery, Design and Analysis of Experiments, John Wiley and Sons, New York (1984).
[44] T. Turanyi, A.S. Tomlin, Analysis of Kinetics Reaction Mechanisms. Springer, Berlin (2004).
[45] Z. Erbay, F. Icier, J. Food Eng. 91 (2009) 533–541.

DRAGOLJUB CVETKOVIĆ[1]
OLJA ŠOVLJANSKI[1]
ALEKSANDRA RANITOVIĆ[1]
ANA TOMIĆ[1]
SINIŠA MARKOV[1]
DRAGIŠA SAVIĆ[2]
BOJANA DANILOVIĆ[2]
LATO PEZO[3]

[1]Univerzitet u Novom Sadu, Tehnološki fakultet Novi Sad, Novi Sad, Srbija
[2]Univerzitet u Nišu, Tehnološki fakultet, Leskovac, Srbija
[3]Institut za opštu i fizičku hemiju, Beograd, Srbija

NAUČNI RAD

VEŠTAČKA NEURONSKA MREŽA KAO ALAT ZA POBOLJŠANJE KOMBUHA FERMENTACIJE

Kombuha je fermentisani napitak na bazi čaja, koji postaje sve rasprostranjeniji uglavnom na tržištu funkcionalne hrane, zbog koristi za poboljšavaju zdravlja. Kao deo svakodnevne ishrane odraslih i dece, kombuha se izdvojila kao bezalkoholno piće koje sadrži smešu korisnih sastojaka: organskih kiselina, minerala, vitamina, proteina, polifenola i dr. U radu je ispitan uticaj specifične površine suda, veličine inokuluma i početne koncentracije čaja kao radnih parametara, i trajanja fermentacije kao izlazne promenljive na efikasnost kombuha fermentacije. Fokus ovog rada je optimizacija i standardizacija uslova kombuha fermentacije korišćenjem Box-Behnken eksperimentalnog dizajna i primenom modela predviđanja veštačke neuronske mreže (ANN) za proces fermentacije. Za unapređenje proračuna korišćen je iterativni algoritam Broiden-Fletcher-Goldfarb-Shanno. Dobijeni ANN modeli za pH vrednost i titrabilnu kiselost pokazali su dobre mogućnosti predviđanja (vrednosti r^2 tokom ciklusa treninga za izlazne varijable bile su 0,990 i 0,994, respektivno). Prediktivno ANN modelovanje pokazalo se efikasnim i pouzdanim u uspostavljanju optimalnog procesa kombuha fermentacije koristeći odabrane radne parametre.

Ključne reči: eksperimentalni dizajn, poboljšanje fermentacije, proizvodnja kombuhe, matematičko modelovanje.

CI&CEQ
Chemical Industry & Chemical Engineering Quarterly

Available online at
Association of the Chemical Engineers of Serbia AChE
www.ache.org.rs/CICEQ

Chem. Ind. Chem. Eng. Q. 28 (4) 287–296 (2022) CI&CEQ

IDA BALCZÁR
ADRIENN BOROS
ANDRÁS KOVÁCS
TAMÁS KORIM

Department of Materials Engineering, Faculty of Engineering, University of Pannonia, Veszprém, Hungary

FOAMED GEOPOLYMER WITH CUSTOMIZED PORE STRUCTURE

Article Highlights

- By varying the concentration of H_2O_2 and surfactant, the porosity can be designed optionally
- It is possible to produce closed-pore thermal insulating materials or open-pore catalyst supports
- Foams with thermal conductivity in the range of 0.130-0.054 W/mK were produced using only H_2O_2
- The use of sodium oleate as a surfactant increased the chance of open-cell formation
- For catalyst support, foams with 75-80 vol% total porosity and >1 MPa strength were achieved

Abstract

Due to their favorable production conditions and promising properties (e.g., low shrinkage after foaming, mechanical and chemical stability, high-temperature resistance), geopolymer foams are suitable for heat- and sound insulating refractory building materials. Another promising field of application may be their use as catalyst supports in water treatment. Metakaolin-based foams were prepared by a direct foaming process with high total porosity (> 75 vol%), low bulk density (< 500 kg/m^3), approximately 1 MPa compressive strength, and low thermal conductivity (0.095 W/mK). By varying the concentration of foaming agent (H_2O_2 solution) and stabilizing agent (sodium oleate), it is possible to produce foams with designed porosity and pore size distribution. Foams with mainly closed pores are suitable for thermal insulation, while those with significantly open pores can use as catalyst supports. The computed tomography images showed that the concentration of stabilizing agent is a key parameter in forming a homogeneous pore structure and open pores; up to 24 vol% open porosity can be achieved without significantly affecting other properties. The physical properties of the foams are equally influenced by the thickness of cell walls and the size of the cells themselves.

Keywords: catalyst support, geopolymer, heat insulator, mechanical property, porous material, thermal conductivity.

SCIENTIFIC PAPER

UDC 666.952:66.017/.018

Cellular materials, especially foamed inorganic solids, have rapidly growing importance in the field of filters, thermal insulators, and catalyst supports. Proper thermal insulation is crucial to avoid wasting energy, whereas inorganic insulators have a great advantage over organic ones: require less hazardous substances for production and have better recycling potential. On the other hand, wastewater treatment is a global environmental problem, where photocatalysis can provide a clean solution, and durable catalyst supports are required. Porosity plays an important role in both cases, and the cell structure must be carefully controlled to achieve the expected properties. Three factors considerably define the cellular material: the properties of the raw material, the topology and shape of the cells, and their bulk density [1].

Foamed inorganic solids can be prepared easily by mixing a cementitious binder with a foaming agent. Although foams made of ordinary Portland cement (OPC) have good thermal insulation properties, the en-

Correspondence: A. Boros, Department of Materials Engineering, Faculty of Engineering, University of Pannonia, H-8201 Veszprém, Egyetem Street 10., P.O. Box 158, Hungary.
E-mail: boros.adrienn@mk.uni-pannon.hu
Paper received: 7 October, 2021
Paper revised: 1 February, 2022
Paper accepted: 11 April, 2022

https://doi.org/10.2298/CICEQ211007003B

vironmental effects of cement production (e.g., high energy demand, CO_2 emissions, landscape destruction, etc.) give serious cause for concern [2].

Binders with lower environmental impact, such as alkali-activated types of cement (and geopolymers), can be good alternatives, proven to have superior physical properties in versatile applications [3,4]. Geopolymers are a significant section of alkali-activated cements and are obtained by mixing a low-calcium natural material (e.g., metakaolin or clay) or an industrial by-product (e.g., fly ash) with a strongly alkaline solution. The resulting cement paste sets at room temperature and has excellent physical properties even at an early age (high compressive strength, good thermal resistance, low shrinkage, etc.) [4].

Production of foams is one of the fastest-growing research fields in recent years of geopolymer applications [5]. Three main methods can achieve the desired porosity (or by their combination):

method 1 mixing gas-releasing agents such as hydrogen peroxide (H_2O_2) [6–12] or fine aluminum powder [7,12–14] with the geopolymer paste/mortar,

method 2 mechanically introducing a substantial volume fraction of air bubbles into the paste [15,16], usually through the use of an organic surfactant which plays a stabilizing agent role,

method 3 mixing a highly porous aggregate with the matrix (for example perlite [16], EPS [17,18], microspheres [18], aggregate from recycled lightweight blocks [19,20]).

In some cases, due to deteriorating mechanical strength, fiber reinforcement is also applied in the geopolymer foams [13,20].

H_2O_2 solution and aluminum powder are used in the largest quantities as chemical foaming agents, which decompose to O_2 and generate H_2 gas, respectively, by the following equations [7,21]:

$$H_2O_{2_{(l)}} \rightarrow 2H_2O_{(l)} + O_{2_{(g)}} \quad (1)$$

$$Al_{(s)} + 3H_2O_{(l)} + OH^-_{(aq)} \rightarrow Al(OH)^-_{4_{(aq)}} + 3/2H_{2_{(g)}} \quad (2)$$

The foaming process can serve a dual purpose: making thermally insulating materials [6–14,17–19,21–25] or foamed inorganic solids for catalyst support applications [15,16,26–28]. In recent studies, the investigated parameters were the chemical composition of the alkali activator solution (for example sodium silicate/sodium hydroxide mass ratio) [6,9,14], the activator/binder mass ratio [6,11,14,23], and the foaming agent concentration [6,7,11,14,21,24,28]. In some references, the foaming agent is also combined with a stabilizing component (surfactant) [21,24], but only Korat and Ducman [21] have investigated the effect of the surfactant concentration. In some cases, surfactants were formed through in-situ saponification of vegetable oils, resulting in a high volume of open porosity [26–28].

Generally, foams derived from fly ash [6,7,14,22,24,25] or metakaolin [9,10,15,26,27] have good thermal insulation properties, with lower than 1000 kg/m^3 bulk density and < 0.1 W/mK heat conductivity and a compressive strength between 1–4 MPa. By foaming, ground granulated blast furnace slag also provides porous structures with slightly higher bulk density and heat conductivity [11]. Still, these foams are mainly made using highly porous materials according to the third method described above [20].

According to the literature, the activator/binder mass ratio needs to be around 0.8 and the sodium silicate/sodium hydroxide mass ratio around 2.5 to achieve the lowest thermal conductivity (< 0.1 W/mK) [6,9,14]. Likewise, a high concentration of sodium hydroxide in the activating solution leads to an unstable H_2O_2 decomposition, while the presence of more sodium silicate in the activating solution results in a more controlled H_2O_2 decomposition rate during foaming [9]. Using a low, 0.55 solid/liquid mass ratio (high activating solution content) and Al powder results in relatively low density (430 kg/m^3) and low thermal conductivity (0.079 W/mK) [23].

Researchers have also shown that the concentration of the foaming agent has a strong effect on bulk density, compressive strength, and heat conductivity. Al powder was applied between 0.01 and 0.2 wt% [10,23,24], while the H_2O_2 content was varied between 0.1 and 20 wt% [6,7,9,24,26,27], depending on the concentration of the solution. Ducman and Korat [7] have shown that using Al powder in the range of 0.07–0.2 wt% resulted in bulk densities between 0.64 and 0.74 g/cm^3 with compressive strengths within the range of 3.3 and 4.3 MPa, while samples prepared from 0.2–2 wt% H_2O_2 had densities between 0.61 and 1.00 g/cm^3 and compressive strengths in the range of 2.9 and 9.3 MPa. Hajimohammadi *et al.* [9] have found that producing foams with homogenously small pore sizes leads to low bulk density and helps gain more strength while providing better thermal insulation capability. Korat and Ducman [21] have established that the stabilizing agent performs best when its amount is adjusted to the amount of the foaming agent. It is difficult to compare the results because of the lack of a consistent definition of foaming agent concentration in the literature.

The current study presents the link between the

composition of the foam (concentration of the foaming agent and surfactant) and the cell structure of the foamed specimens. In addition, the most important physical properties such as bulk density, total and open porosity, water absorption, compressive strength, and thermal conductivity were also studied. By clarifying the relationship between cell structure and physical properties, the aim was to produce geopolymer foams with controlled properties that could act as thermal insulators or catalyst supports.

MATERIAL AND METHODS

Materials

Metakaolin, obtained from New-Zealand kaolin by calcination at 750 °C for 8 h, was used for geopolymer production. The original clay contained mainly kaolinite and halloysite phases and quartz and cristobalite as minor constituents (identified using a Philips PW 3710 X-Ray powder diffractometer – reported in a previous article [29]). The chemical composition of the metakaolin was determined by wet chemical analysis, resulting in SiO_2 56.3, Al_2O_3 38.0, TiO_2 0.2, Fe_2O_3 0.9, CaO 0.5, MgO 0.5, Na_2O 0.4, K_2O 1.0, LOI 2.2 wt%. The mean particle size was 15.8 μm (determined by a Fritsch Laser Particle Sizer).

The alkali activator solution was produced using commercially available sodium silicate solution (SiO_2 28.6, Na_2O 6.8, H_2O 64.5 wt%, ANDA) and laboratory-grade sodium hydroxide pellet (Scharlab). In addition, H_2O_2 solution with 30 wt% (Reanal) was applied as a chemical foaming agent and sodium oleate powder (Sigma) as a stabilizing agent.

Sample preparation

Metakaolin-based foamed geopolymers (FG) were made. An alkali activator solution was first prepared during the experiments by dissolving the required amounts of sodium hydroxide pellets in sodium silicate solution (and in distilled water as needed). Then the specified amount of H_2O_2 solution and sodium oleate powder was added to the activating solution (Table 1). After this mixture cooled down to room temperature, it was mixed with the metakaolin powder for 1 min. Next, the slurry was cast into cylindrical molds of dimensions Ø36 mm × 36 mm. One hour after the final setting (195-240 min depending on composition), the "cup" (the excess amount of foamed sample) was removed with a sharp knife to prevent cracking, which may occur due to the shrinkage of the sample. The specimens were demolded at 1 day of age and stored at ambient conditions (21-23 °C and RH = 50 ± 10%) until 7 days. Large-size samples were prepared in a wooden mold with 200 mm × 200 mm × 15 mm.

The composition of the geopolymer paste applied in the experiments was as follows: SiO_2/Al_2O_3 = 3.4, Na_2O/Al_2O_3 = 1.0, the sodium silicate modulus of the alkali activator solution = 1.4, the amount of Na_2O in relation to the dry metakaolin was 23.1 wt%, the mass ratio of the sodium silicate and sodium hydroxide pellets was 5.4, while that of the activator solution and metakaolin powder was 1.3.

In stage I, the concentration of the chemical foaming agent was varied as 0.0, 0.8, 1.6, 2.3, 3.1, 4.5, 6.0, 11.3 wt% H_2O_2 solution relative to the mass of metakaolin. In stage II, compositions with the most favorable physical properties were compared with the mixtures supplemented with a fixed amount of sodium oleate surfactant (1.4 wt% relative to the mass of metakaolin). Finally, in stage III, the surfactant concentration was applied as 0.1, 0.3, 0.5, 1.0, 1.4, 2.1, and 2.8 wt% relative to the mass of metakaolin with a fixed amount of chemical foaming agent. The investigated mixtures are presented in Table 1.

Table 1. Foaming agent contents of the specimens

Series	Foaming agent concentration, wt%	
	H_2O_2 solution	Sodium oleate
I	0.0, 0.8, 1.6, 2.3, 3.1, 4.5, 6.0, 11.3	0.0
II	3.1, 4.5, 6.0	0.0
	3.1, 4.5, 6.0	1.4
III	4.5	0.1, 0.3, 0.5, 1.0, 1.4, 2.1, 2.8

According to the following system, Samples were named FG (foamed geopolymer) H_2O_2 solution concentration/sodium oleate concentration; "Δ" indicates the varied parameter. For example, FG Δ/0.0 means a foamed geopolymer sample with various H_2O_2 solutions without sodium oleate content.

Characterization

A Controls 5 universal testing machine performed compressive strength tests with a loading rate of 2400±1 N/s according to EN 196-1. However, the sample sizes differed from the standard (Ø 36 × 36 mm cylindrical samples were tested). Three samples of each formulation were tested, and the average data were reported at the age of 7 days. The sample surfaces were polished flat and parallel before testing if it was necessary.

The bulk density of geopolymer samples was obtained by measuring the mass to volume ratios in foamed samples (0.0 wt% < H_2O_2 content (ρ_b)).

The porosities and water absorption were determined by Archimedes' method.

The samples were placed in distilled water for 2 hours and weighed on a hydrostatic balance. Water absorption was calculated by the following equation (Eq. (3)):

$$w_A(wt\%) = 100 \cdot (m_2 - m_1) / m_1 \quad (3)$$

where m_1 is the weight of the dry sample, m_2 is the weight of the sample after 2 hours of water absorption. The apparent porosity was obtained by the Eq. (4):

$$P_A(vol\%) = \rho_B \cdot w_A \quad (4)$$

where ρ_b is the bulk density. Total porosity was calculated using the true density and bulk density of samples with the following equation (Eq. (5)):

$$P_T(vol\%) = 100 \cdot (1 - \rho_B / \rho_T) \quad (5)$$

where ρ_b is the apparent density of the foamed samples, while ρ_t is the true density of the geopolymer matrix (1961 kg/m^3), determined by the pycnometer method.

Heat conductivity (λ) was measured using the MTPS (Modified Transient Plane Source) method with a C-Therm TCi equipment. Before characterization, the bottom of the samples was polished and the powder removed from the exposed pores; no contact agent was used for measurement. The larger (200 mm × 200 mm × 15 mm) samples were examined using the heat flow meter method with NETZSCH HFM 436/3/1 Lambda equipment. Before measurement, the surface of samples was polished parallel.

The MTPS technique is a fast thermal conductivity measuring method. It does not require large-sized specimens, but the thermal conductivity value obtained is lower than the one measured with a heat flow meter, which is generally used to determine the thermal resistance of insulators. For this reason, the MTPS method was used to compare the thermal conductivity values of the differently foamed specimens and investigate the tendency in thermal conductivity during the series of experiments. Based on the series II and III results, two compositions were chosen; a: using only H_2O_2 (FG3.4/4.5/0.0) and b: combination of H_2O_2 and surfactant (FG3.4/4.5/1.4). Large-sized samples (200 x 200 x 15 mm) were prepared from these compositions as described at the beginning of the Sample preparation section. Their thermal conductivity was measured by the heat flow meter method.

Samples were prepared separately for cell structure investigation, where the top of the specimens was not removed. The cell structure was characterized by a NIKON XT H 225 ST X-ray tomography, which was also used to assess the distribution of different pores (type, size) in the samples. It is important to notice that this method is non-destructive, which is essential in the case of such fine structures. The pore size distribution and pore wall thickness values were measured by a KEYENCE VHX 2000 digital microscope. Before the examination, the cross-section of the samples was polished flat and coated with gold/palladium films to a thickness of 2-3 nm (using a BALZERS SCD020 type unit) for better contrast. Pore size distribution and pore wall thickness values were obtained by taking the average of 100 pore diameters and 50 pore wall thicknesses.

RESULTS AND DISCUSSION

Effect of foaming agent concentration

One must note that the water content of the chemical foaming agent, H_2O_2 solution, was not compensated. Consequently, with the increase in H_2O_2, the water content of the geopolymer paste also raised from 28.9 wt% (0.0 wt% H_2O_2) to 31.1 wt% (11.3 wt% H_2O_2).

The compressive strength and bulk density results of the stage I tests can be seen in Figure 1a. The values of the dense samples (0.0 wt% H_2O_2) were outstandingly high (61.3 MPa and 1631 kg/m^3, respectively) and therefore are not depicted in this figure. Compressive strength rapidly falls from ~60 MPa below 10 MPa by applying 1.6 wt% of H_2O_2, but further addition of foaming agent causes a slower decline in strength. A similar trend can be observed for bulk density results. For instance, a higher foaming agent concentration does not lead to a proportionately lower bulk density, while the smallest attainable bulk density was around 500 kg/m^3. In addition, Ducman and Korat [7] report similar results with 2.9 MPa and a bulk density of 0.61 g/cm^3. Their higher strength result can result from a different loading rate, applying 5 N/s 480 times lower than the loading rate used in the present study.

Porosity and water absorption results (Figure 1b) indicate a change in structure when the foaming agent concentration exceeded 3.1 wt%. Total porosity did not change considerably even if the H_2O_2 concentration was raised from 3.1 to 11.3 wt% (the highest total porosity was ~75 vol%). In contrast, water absorption rapidly rose from 6–10 wt% to 36 wt%, and a similar but less remarkable tendency can be seen in the case of open porosity (from ~10 vol% to 18 vol%). These two properties are closely related: more water can enter the sample due to the higher number of open pores.

The thermal conductivity of the dense sample was 1.280 W/mK, determined by the MTPS method.

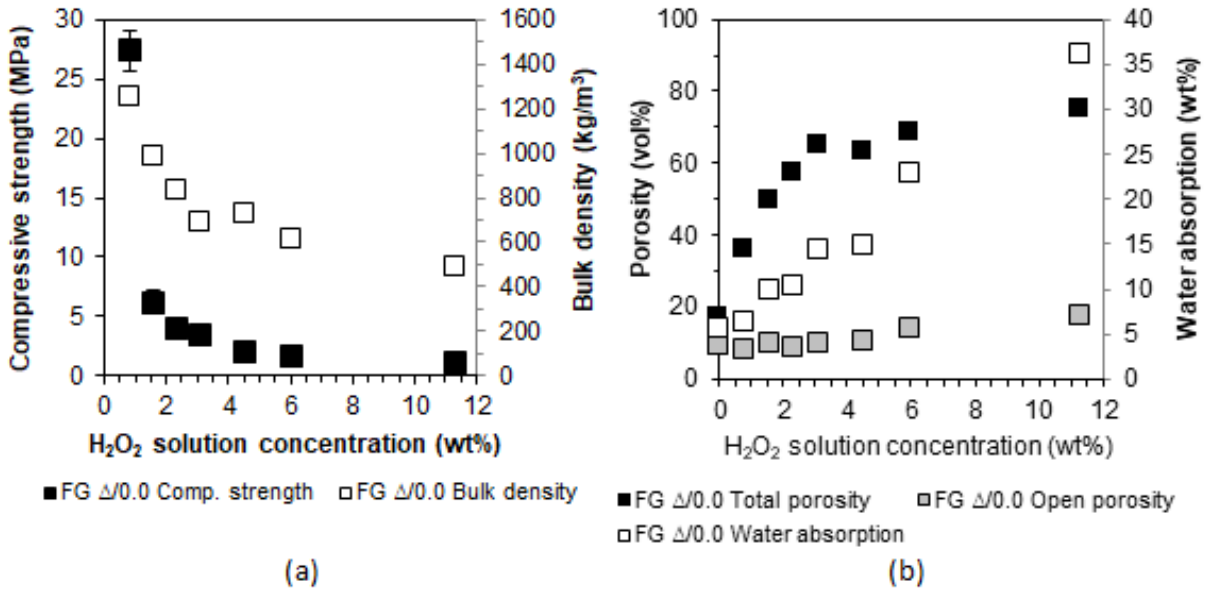

Figure 1. Compressive strength, bulk density (a), total porosity, open porosity, and water absorption (b) results in stage I testing at 7 days of age.

On the other hand, thermal conductivity for foamed samples was 0.130-0.060 W/mK (Table 2). The lowest result was achieved with 4.5 wt% of H_2O_2 and got slightly higher (0.070 W/mK) with the increase of foaming agent.

Table 2. Thermal conductivity results in stage I testing at 7 days of age

Sample name	Thermal conductivity (W/mK)
FG 0.0/0.0	1.280 ± 0.009
FG 0.8/0.0	0.130 ± 0.019
FG 1.6/0.0	0.090 ± 0.001
FG 2.3/0.0	0.066 ± 0.003
FG 3.1/0.0	0.080 ± 0.001
FG 4.5/0.0	0.067 ± 0.002
FG 6.0/0.0	0.070 ± 0.001
FG 11.3/0.0	0.070 ± 0.006

According to CT images (Figure 2) and pore characteristics (Table 3), the concentration of H_2O_2 solution has a subtle effect on cell size, cell wall thickness, and pore size distribution. For example, using only H_2O_2 as a foaming agent leads to a heterogeneous pore structure, which, based on light microscopic images (Figure 3), consists of macrocells larger than 250–350 μm diameter, and the space between them being populated with much smaller ones, causing increased cell wall thicknesses (Table 3). Bai *et al.* [27] experienced similar phenomena when making foams using a mixture of H_2O_2 and oil as surfactants.

Table 3. Cell diameters and cell-wall thicknesses of the foam samples using H_2O_2 as a foaming agent

Sample name	Average cell diameter (μm)	Average cell wall thickness (μm)
FG 1.6/0.0	516 ± 158	215 ± 135
FG 4.5/0.0	703 ± 661	709 ± 476
FG 6.0/0.0	1546 ± 532	592 ± 382
FG 3.1/1.4	140 ± 31	47 ± 36
FG 6.0/1.4	427 ± 84	38 ± 26
FG 4.5/0.5	392 ± 60	35 ± 32

Increasing the amount of the H_2O_2 solution leads to larger pore sizes (1.6 wt%, 4.5 wt%, and 6.0 wt% to around 520 μm, 700 μm, and 1550 μm, respectively). It can be explained by the release of a larger amount of O_2, as well as the larger water contents. A higher O_2 concentration means that cell walls need to withstand increased oxygen pressure. A higher water content (due to the higher H_2O_2 concentration) and thus lower viscosity of the geopolymer paste may also weaken the cell walls. Increasing the foaming agent content causes the cell size distribution to become heterogeneous in any given volume and the cross-section of the sample, meaning that the bottom of the sample is populated with much smaller cells than the top. Due to their buoyancy, the larger pores are likely to rise in the plastic sample (before the setting). The most significant cells are found directly under the sample cap, which may be trapped

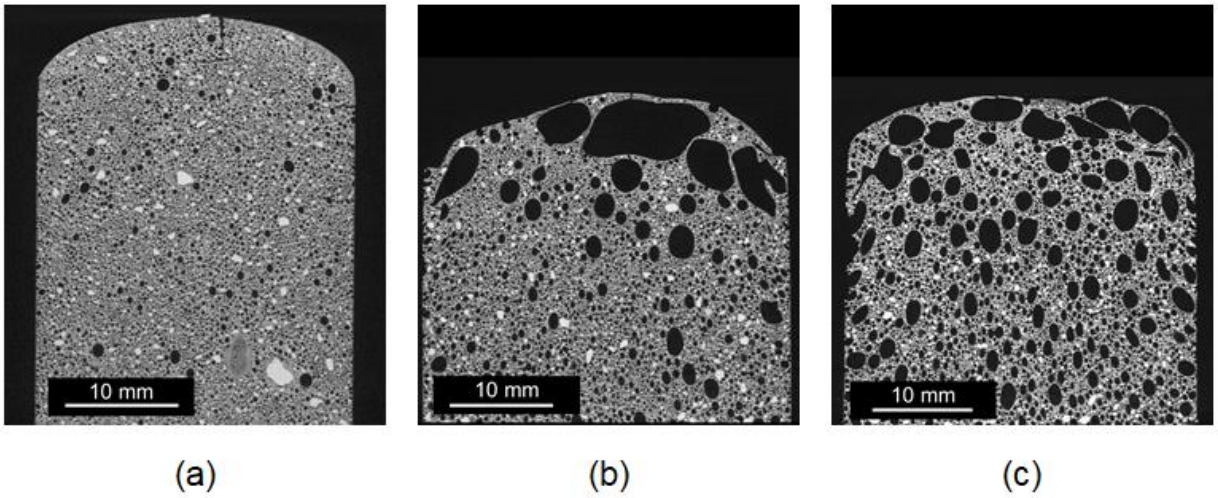

Figure 2. The pore structure of the foam samples in stage I testing using H_2O_2 as a foaming agent (selected samples were the following: a = FG 1.6/0.0, b = FG 4.5/0.0, and c = 6.0/0.0).

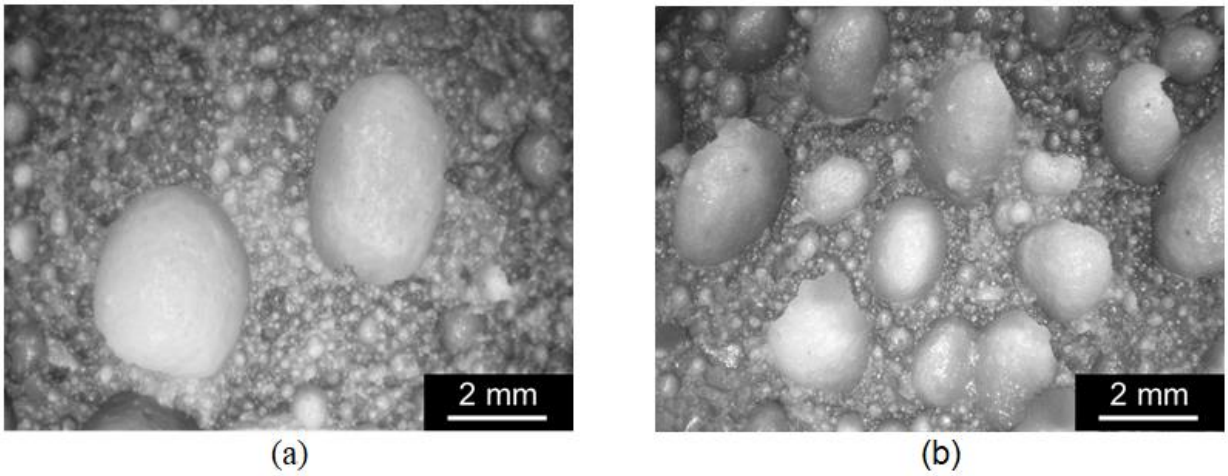

Figure 3. The cell wall structure of foamed samples in stage I testing using H_2O_2 (selected samples were the following: a = FG 4.5/0.0 and b = FG 6.0/0.0).

because geopolymer samples tend to have a thin, rapidly setting layer on their top. It is due to the reaction between CO_2 in the air and water glass in the activator solution. The white particles on the CT images, indicating a higher X-ray absorbance in the rendering mode, are undissolved metakaolin particles. Their amount also decreases with increasing H_2O_2 contents.

The microstructure development explains many phenomena in changing physical properties (Figure 2). Higher than 1.6 wt% H_2O_2 concentration leads to heterogeneous cell size and thicker cell walls. The paste cannot hold the higher concentration of released oxygen, and the foaming gas "escapes" from it, which causes the collapse of the foam. Therefore, a higher concentration of H_2O_2 results in unpredictable properties instead of the expected lower bulk density or higher total porosity. The rupturing pores also cause more open cells, increasing water absorption (Figure 1). The thicker cell walls explain the moderate compressive strength and the slight increase in thermal conductivity (Tables 2 and 3).

Effect of surfactant concentration

A foam stabilizer was used to avoid the pore coalescence and collapse of the pore structure in stages II and III. Figure 4a shows the compressive strength and bulk density results of geopolymer foams where sodium oleate was applied as a commonly used surfactant (1.4 wt%), the results are compared to those of samples prepared with H_2O_2 only. The surfactant used has a strong effect on physical properties. A much lower bulk density (with the minimum value of ~360 kg/m^3) can be achieved with considerable strength loss. In addition, a surfactant concentration

even as low as 0.1 wt% remarkably reduces bulk density (from 724 kg/m^3 to 512 kg/m^3), with a further increase in sodium oleate level impairing compressive strength, causing it to drop from ~2.0 MPa (0.1 wt% sodium oleate) to ~1.2 MPa (≥ 1.0 wt% sodium oleate), (Figure 4b).

It was already noticeable from the bulk density results but even more apparent when considering porosity and water absorption data that in the case of 3.1 wt% H_2O_2, there is no significant difference between the properties of samples made with or without surfactant (Figure 5a). However, with the rise of H_2O_2 concentration, bulk density, and compressive strength drop remarkably, but there is also a sharp rise in porosities and water absorption.

Varying the amount of surfactant showed that (Figure 5b), similarly to bulk density results, 0.1 wt% is sufficient for the highest achievable total porosity (~75 vol%). Further increase in the sodium oleate content leads to a higher proportion of open porosity (from ~10 vol% to ~20 vol%), with greater water absorption.

The lower bulk density and greater porosity

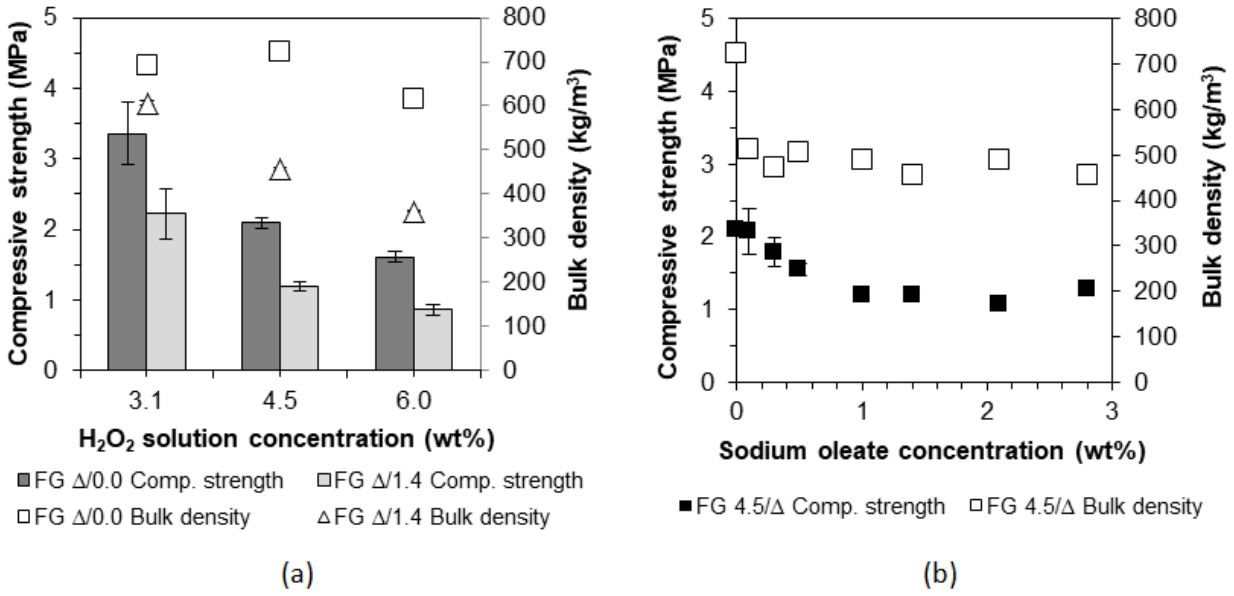

Figure 4. Compressive strength and bulk density results in stage II (a) and stage III (b) testing at 7 days of age.

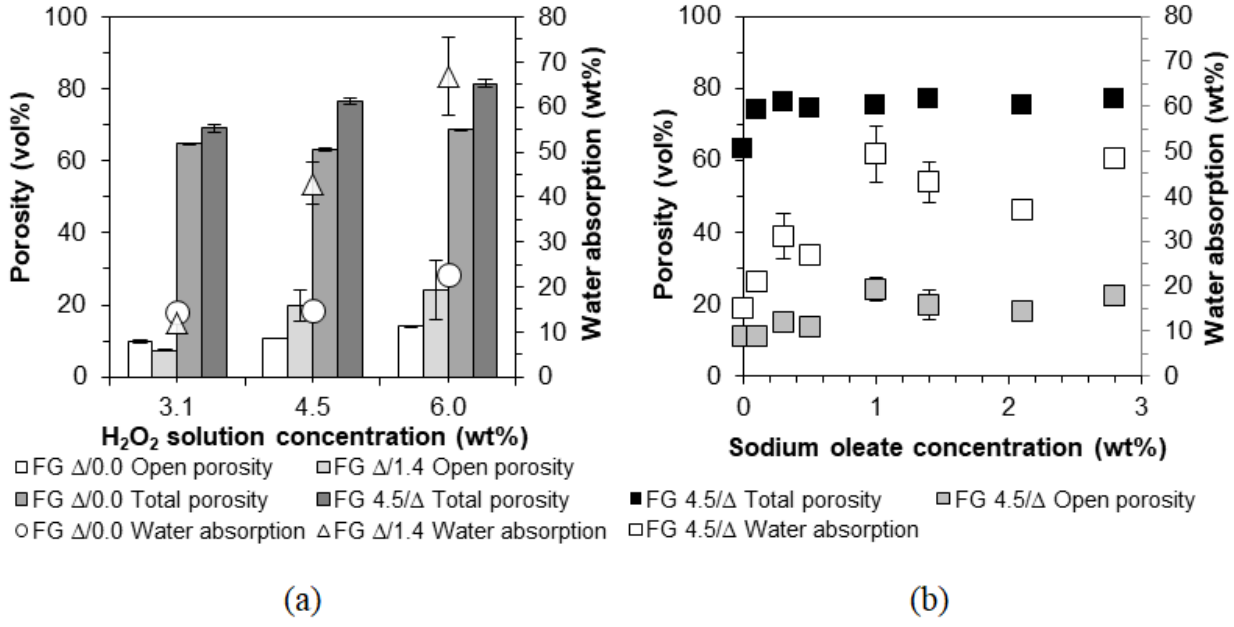

Figure 5. Total, apparent porosity and water absorption results in stage II (a) and stage III (b) testing at 7 days of age.

caused lower thermal conductivity when applied surfactant (Figure 6a). Nevertheless, the MTPS method is moderately accurate in such a small thermal conductivity data range. It may be why there is no significant difference between samples prepared with varying amounts of H_2O_2. It can also be stated that a surfactant content higher than 0.5 wt% does not affect the insulating properties significantly (Figure 6b).

Large-size samples with the composition of FG 4.5/0.0 and FG 4.5/1.4 were also prepared, and their thermal conductivities were determined by the heat flow meter method at 7 days of age:

- FG3.4/4.5/0.0: λ = 0.159 W/mK
- FG3.4/4.5/1.4: λ = 0.095 W/mK

It can be established that the surfactant notably influenced the thermal conductivity of the foams, and samples can be prepared with lower than 0.1 W/mK thermal conductivity.

The application of a surfactant makes significant changes in the pore structure, even with the smallest amount of surfactant (0.1 wt% sodium oleate). It influences pore distribution, size, and thickness of pore walls. Namely, pore sizes decrease from the range of 500–1500 μm to 150–450 μm, the pore structure becomes more homogeneous (the standard deviation of pore size is around 40–60 μm), and the thickness of the pore walls also decreases to 25–40 μm (Table 3). The small voids and homogeneous pore structure explain the lower bulk density, higher porosity (Figures 4a and 5a), and better insulating abilities (lower thermal conductivity, Figure 6a). Still, the thin pore walls weaken the structure, leading to lower compressive strength (Figure 4a) than using a foaming agent alone with the same concentration. Wide cracks can also be seen because of the increased shrinkage of the samples, but they can be avoided if the tops of the samples are removed shortly after the final set as described in the Sample preparation.

It is also an important observation that if the pore structure is homogeneous, then compressive strength and thermal conductivity are more dependent on the thickness of pore walls than on the diameter of cells (Figure 7).

Sodium oleate concentration has a limited impact on physical properties (compressive strength, thermal conductivity), which implies that the amount of foaming agent has a greater influence on cell size and cell wall thickness than has the surfactant content. Surfactant affects only the water absorption and thus the open porosity. Higher amounts of surfactant increase the chance of the formation of open cells. Therefore, the concentration of the surfactant needs to be carefully selected, depending on the application. For insulation, a sufficient quantity is required (in the case of this research, ~0.5 wt%); for catalyst support applications, however, an even higher surfactant concentration is needed.

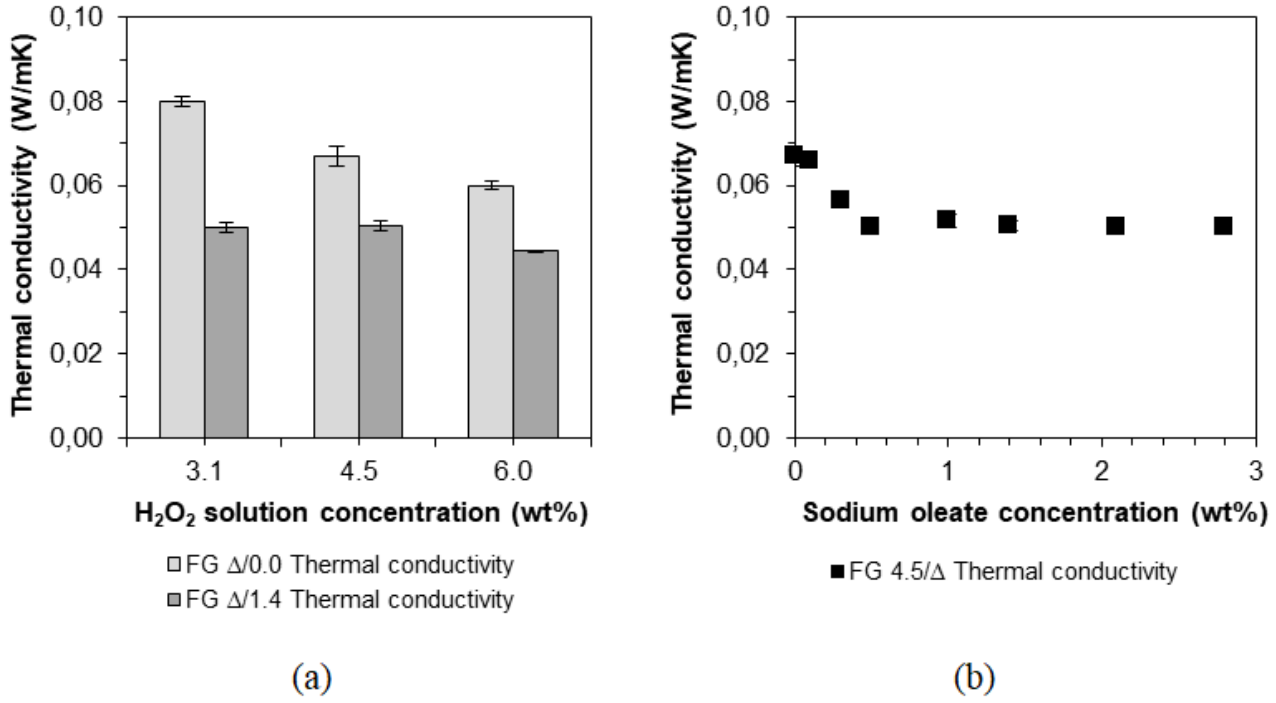

Figure 6. Thermal conductivity results in stage II (a) and stage III (b) testing at 7 days of age.

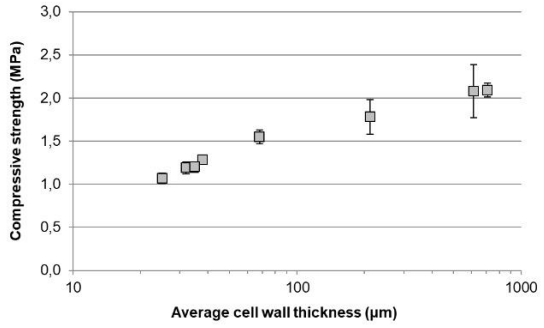

Figure 7. The relationship between compressive strength and average cell wall thickness for samples with a homogeneous pore size distribution.

CONCLUSION

This paper aimed to investigate the effect of the foaming agent (H_2O_2) and surfactant (sodium oleate) concentrations on the physical properties of foamed geopolymers. As a result, it can be concluded that foams with a customized pore structure can be produced.

Favorable insulating properties can be achieved by combining H_2O_2 and sodium oleate: 75–80 vol% total porosity, < 500 kg/m^3 bulk density, > 1 MPa compressive strength, 0.095 W/mK thermal conductivity (heat flow meter method).

Homogeneous cell structure can be achieved by using only H_2O_2 up to the amount of 3 wt%. Above this threshold, the cell walls start to collapse due to the increased pressure by O_2 formation, leading to a heterogeneous cell structure with a higher proportion of open cells.

A sodium oleate concentration of 0.5 wt% is sufficient for forming fine, homogeneous pores. Higher surfactant levels lead to a higher proportion of open cells. The surfactant plays a key role in producing satisfactory catalyst support with a high specific surface area.

Based on the experiments performed, it can be said that in the case of a homogeneous pore structure, cell wall thickness has a greater impact on the physical properties of geopolymers than the pore size itself.

Acknowledgment

The authors acknowledge financial support from Széchenyi 2020 Fund under project codes EFOP-3.6.1-16-2016-00015 and GINOP-2.3.2-15-2016-00016. The present work is also supported by the ÚNKP-17-3-II-PE-3 New National Excellence Program of the Hungarian Ministry of Human Resources.

Nomenclature

Ø	Sample diameter, mm
EN 196-1	Methods of testing cement – Part 1: Determination of strength
m_1	Weight of the dry sample, g
m_2	Weight of the sample after 2 hours of water absorption, g
min.	Minute
P_A	Apparent porosity, vol%
P_T	Total porosity, vol%
vol%	Volume %
w_A	Water absorption, wt%
wt%	Weight %
Greek	
Δ	Varied parameter during the foaming process
λ	Thermal conductivity, W/mK
ρ_b	Bulk density, kg/m^3
ρ_t	True density, kg/m^3
Subscripts	
aq.	Aqueous solution
g	Gas
l	Liquid
s	Solid
Abbreviations	
CT	Computed tomography
EPS	Expanded polystyrene
FG	Foamed geopolymer
LOI	Loss on ignition
MTPS	Modified Transient Plane Source

REFERENCES

[1] M. Scheffler, C. Paolo, Cellular ceramics: structure, manufacturing, properties and applications, Wiley-VCH, Weinheim (2006).

[2] M. Nodehi, Innov. Infrastruct. Solut. 6 (2021) 231.

[3] C. Shi, D. Roy, P. Krivenko, Alkali-activated cements and concretes, CRC press, Boca Raton (2003).

[4] I. Garcia-Lodeiro, A. Palomo, A. Fernández-Jiménez, in Handbook of alkali-activated cements, mortars and concretes, F. Pacheco-Torgal, J.A. Labrincha, C. Leonelli, A. Palomo, P. Chindaprasirt, Woodhead Publishing, Cambridge (2015), pp. 19–47.

[5] Z. Zhang, J.L. Provis, A. Reid, H. Wang, Constr. Build. Mater. 56 (2014) 113–127.

[6] Z. Abdollahnejad, F. Pacheco-Torgal, T. Félix, W. Tahri, J.B. Aguiar, Constr. Build. Mater. 80 (2015) 18–30.

[7] V. Ducman, L. Korat, Mater. Charact. 113 (2016) 207–213.

[8] V. Vaou, D. Panias, Miner. Eng. 23 (2010) 1146–1151.

[9] A. Hajimohammadi, T. Ngo, P. Mendis, T. Nguyen, A. Kashani, J.S. van Deventer, Mater. Des. 130 (2017) 381–391.

[10] A. Hajimohammadi, T. Ngo, P. Mendis, J. Sanjayan, Mater. Des. 120 (2017) 255–265.

[11] M. Şahin, S.T. Erdoğan, Ö. Bayer, Constr. Build. Mater. 181 (2018) 106–118.

[12] Z. Liu, N.N. Shao, T.Y. Huang, J.F. Qin, D.M. Wang, Y. Yang, Int. J. Miner., Metall. Mater. 21 (2014) 620–626.

[13] W.D. Rickard, L. Vickers, A. Van Riessen, Appl. Clay Sci. 73 (2013) 71–77.

[14] J.G. Sanjayan, A. Nazari, L. Chen, G.H. Nguyen, Constr. Build. Mater. 79 (2015) 236–244.

[15] M.S. Cilla, M.R. Morelli, P. Colombo, Ceram. Int., 40 (2014) 13585–13590.

[16] M.S. Cilla, M.R. Morelli, P. Colombo, J. Eur. Ceram. Soc. 34 (2014) 3133–3137.

[17] F. Colangelo, G. Roviello, L. Ricciotti, V. Ferrándiz-Mas, F. Messina, C. Ferone, O. Tarallo, R. Cioffi, C.R. CheesemanCem. Concr. Compos. 86 (2018) 266–272.

[18] P. Duan, L. Song, C. Yan, D. Ren, D., Z. Li, Ceram. Int. 43 (2017) 5115–5120.

[19] P. Posi, C. Teerachanwit, C. Tanutong, S. Limkamoltip, S. Lertnimoolchai, V. Sata, P. Chindaprasirt, Mater. Des. 52 (2013) 580–586.

[20] M. Mastali, P. Kinnunen, H. Isomoisio, M. Karhu, M. IllikainenConstr. Build. Mater. 187 (2018) 371–381.

[21] L. Korat, V. Ducman, Cem. Concr. Compos. 80 (2017) 168–174.

[22] L. Zhang, F. Zhang, M. Liu, X. Hu, Chem. Eng. J. 313 (2017) 74–82.

[23] R.M. Novais, G. Ascensão, N. Ferreira, M.P. Seabra, J.A. Labrincha, Ceram. Int. 44 (2018) 6242–6249.

[24] G. Masi, W.D.A. Rickard, L. Vickers, M.C. Bignozzi, A. Van Riessen, Ceram. Int. 40 (2014) 13891–13902.

[25] M. Łach, K. Korniejenko, J. Mikuła, Procedia Eng. 151 (2016) 410–416.

[26] C. Bai, G. Franchin, H. Elsayed, A. Conte, P. Colombo, J. Eur. Ceram. Soc. 36 (2016) 4243–4249.

[27] C. Bai, T. Ni, Q. Wang, H. Li, P. Colombo, J. Eur. Ceram. Soc. 38 (2018) 799–805.

[28] C. Bai, G. Franchin, H. Elsayed, A. Zaggia, L. Conte, H. Li, P. Colombo, J. Mater. Res. 32 (2017) 3251–3259.

[29] I. Balczár, T. Korim, A. Dobrádi, Constr. Build. Mater. 93 (2015) 983–988.

IDA BALCZÁR
ADRIENN BOROS
ANDRÁS KOVÁCS
TAMÁS KORIM

Department of Materials Engineering, Faculty of Engineering, University of Pannonia, Veszprém, Hungary

NAUČNI RAD

PENASTI GEOPOLIMER SA PODEŠENOM STRUKTUROM PORA

Zbog svojih povoljnih uslova proizvodnje i svojstava (npr. nisko skupljanje nakon formiranja pene, mehanička i hemijska stabilnost, otpornost na visoke temperature), geopolimerne pene su pogodne za toplotno i zvučno izolacione vatrostalne građevinske materijale. Još jedno obećavajuće polje primene može biti njihova upotreba kao nosača katalizatora u obradi vode. Pene na bazi metakaolina pripremljene su postupkom direktnog formiranja pene sa visokom ukupnom poroznošću (> 75% v/v), malom zapreminskom gustinom (< 500 kg/m^3), kompresivnom čvrstoćom od približno 1 MPa i niskom toplotnom provodljivošću (0,095 W/mK). Promenom koncentracije sredstva za formiranje pene (rastvor H_2O_2) i stabilizatora (natrijum oleat), moguće je proizvesti pene sa projektovanom poroznošću i distribucijom veličine pora. Pene sa uglavnom zatvorenim porama su pogodne za toplotnu izolaciju, dok one sa znatno otvorenim porama mogu koristiti kao nosači katalizatora. Snimci kompjuterizovane tomografije su pokazali da je koncentracija stabilizacionog agensa ključni parametar u formiranju homogene strukture pora i otvorenih pora; do 24% v/v otvorene poroznosti može se postići bez značajnog uticaja na druga svojstva. Na fizička svojstva pena podjednako utiču i debljina ćelijskih zidova i veličina samih ćelija.

Ključne reči: nosač katalizatora, geopolimer, toplotni izolator, mehanička svojstva, porozni materijal, toplotna provodljivost.

CI&CEQ
Chemical Industry & Chemical Engineering Quarterly

Available online at
Association of the Chemical Engineers of Serbia AChE
www.ache.org.rs/CICEQ

Chem. Ind. Chem. Eng. Q. 28 (4) 297–304 (2022) CI&CEQ

FADIME BEGÜM TEPE[1]
TOLGA KAĞAN TEPE[1]
AYTEN EKINCI[2]

[1]Department of Food Technology, Şebinkarahisar Vocational School of Technical Science, Giresun University, Giresun, Turkey

[2]Department of Food Technology, Denizli Vocational School of Technical Science, Pamukkale University, Denizli, Turkey

SCIENTIFIC PAPER

UDC 634.33:66.047.3.085

DRYING KINETICS AND ENERGY EFFICIENCY OF MICROWAVE-DRIED LEMON SLICES

Article Highlights

- Microwave lemon drying at various microwave powers fitted to Page model
- The drying rate increased, and drying time decreased with the increase of microwave power
- Effective moisture diffusivity increased with the increase of microwave power
- The higher the cumulative energy efficiency, the lower the specific energy consumption

Abstract

In the current study, lemon slices were dried at various microwave powers (120, 350, 460, 600, and 700 W) to determine drying characteristics and energy efficiency. Drying rate and time were significantly affected by the increase in microwave power. The lowest and highest drying times were 8 and 54 minutes at 700 and 120 W, respectively. As microwave power increased, drying rate increased, and drying time decreased. Besides, the most suitable model to describe microwave drying curves of the lemon slice was obtained as the Page model. The values of D_{eff} of the dried lemon slices were calculated between $3.61x10^{-9}$ and $3.41x10^{-8}$ m^2s^{-1}. The E_a of the lemon slices drying, calculated using D_{eff}, and the rate constant obtained from the Page model were 4.39 Wg^{-1} and 6.04 Wg^{-1}, respectively. Additionally, the higher the cumulative energy efficiency, the lower the specific energy consumption. The lowest specific energy consumption and the highest energy efficiency were calculated at 460 W. The 460 W drying power was the best power with 11 min of drying time, the highest energy efficiency, and the lowest specific energy consumption.

Keywords: lemon slices, drying characteristics, microwave drying, effective diffusion, energy efficiency.

Lemon (*Citrus limon* L.) is a fruit that contains high water content and is rich in nutritional compounds such as flavonoids and ascorbic acid. On the other hand, lemon is quite attractive due to its flavor and color [1–3]. Therefore, lemon is generally consumed as a beverage following fresh fruit consumption; however, the drying process improves novel products such as dried-lemon slices or flakes [2,4,5]. On the other hand, Darvishi *et al.* [1] have also stated high relative metabolic activity of lemon, resulting from increased water content and proceed after harvest and cause deterioration and economic loss.

Many factors associated with food spoilage result from high water content since high water content is one of the main requirements for microbiological activity, chemical reactions, and physical alterations in a pre- or post-harvest period of many plant-based foods [3, 5, 6]. The drying process, one of the most preferred conservation methods, aims to prevent microbiological activity, provide long shelf-life, and reduce undesirable physical and chemical changes by removing water content and activity [7–11]. In addition to benefits in terms of food quality, drying provides lower packing, transportation, and storage costs because of a reduction in weight and volume [6].

The main drying mechanisms are surface diffusion

Correspondence: T.K. Tepe, Department of Food Technology, Şebinkarahisar Vocational School of Technical Science, Giresun University, Giresun, Turkey.
E-mail: tolga.kagan.tepe@gmail.com
Paper received: 25 January, 2021
Paper revised: 11 November, 2022
Paper accepted: 19 April, 2022

https://doi.org/10.2298/CICEQ210125004T

or liquid diffusion on porous surfaces, liquid or vapor diffusion due to moisture concentration differences in granular and porous foods, and capillary movements due to surface forces. The primary diffusion mechanism, which determines the drying rate, is a function of moisture content and the structure of the foods [12]. Drying could generally be divided into constant- and falling-rate periods [13]. A constant rate period is associated with a saturated surface, which means adequate moisture transfer from interior parts of foods to the surface. On the contrary, insufficient moisture transfer from the interior to the surface begins to be observed in the falling rate period when a critical moisture level is reached after the constant rate period. It indicates that the moisture transfer rate to the surface is less than the evaporation rate, decreasing the drying rate [12,13].

Convective or hot air drying is the most frequently used method despite high energy consumption, long drying time, and nutritional losses based on drying temperature and time [10,14–16]. Due to these disadvantages, improving novel applicable techniques, which enable to shorten drying time, consume low energy, and preserve nutritional composition, have become a requirement. Microwave drying is of many advantages in comparison to convective drying. In microwave drying, a water vapor pressure gradient occurs between the surface of the food and its interior due to microwave-induced volumetric heating [17]. Thus, the drying rate increases with the increment in evaporation rate. Additionally, higher microwave powers enable more water vapor pressure gradient and an evaporation rate because more energy is supplied [18]. Furthermore, microwave application during the drying process can be an alternative method to reduce falling rate time [19]. Besides, it was stated that the microwave heating process provided desirable structural modifications, such as lower shrinkage [12]. On the other hand, recent developments in low-cost microwave sources have made microwave drying more attractive [15,20].

The drying kinetics of foods are generally determined by using thin-layer drying models. Thin-layer drying models are mathematical modeling that predicts drying behavior and appropriate drying conditions. Thus, the drying process can be designed and optimized [21].

Although many papers on drying various foods are current in the literature, the drying kinetics of microwave-dried lemon slices are limited. On the other hand, no data on the energy efficiency of microwave drying of lemon slices was published to the best of our knowledge. Therefore, it is hard to claim that microwave energy efficiency shows similar behavior in foods. Therefore, microwave energy efficiency must be investigated in trend foods such as lemon in terms of drying technology. Thus, processes may be efficient in an energy-saving-food quality preserving combination. Therefore, this study aims a) to determine the best fitting equation for microwave drying of lemon slices, b) to compare the impact of different microwave powers on drying time, drying rate, and adequate moisture diffusivity, and c) to calculate energy efficiency in terms of cumulative energy efficiency and specific energy consumption.

MATERIAL AND METHODS

Sample preparation

Fresh lemons were provided from a local market in İstanbul, a province in Turkey. Initially, fresh lemons were washed to remove foreign materials and cut into 6±0.5 mm slice thickness. Then, the initial moisture content of fresh lemons was determined at 105 °C in a drying oven until the sample weight achieved a constant value (%86.89±0.31).

Drying experiment

A microwave oven (Arçelik MD 574, Turkey), with 700 W output at 2450 GHz, was used for drying experiments. Microwave drying was performed at 700, 600, 460, 350, and 120 W levels. For each drying experiment, 70 g of samples were weighted on a glass plate and placed in the microwave oven. The intermittent on/off timing drying process was carried out 20 s on/10 s off [16,22,23]. Glass plate was weighted at the end of each 30 s for determination of moisture loss during drying. The weight measurement was carried out with a digital weight measure with 0.01 g precision. The drying experiments continued until the moisture content of samples achieved 7% on a wet basis. All drying experiments were performed in triplicate.

Mathematical modeling of drying data

Thin-layer drying modeling of drying is a necessary procedure to design the best drying conditions. Therefore, the thin-layer drying models, the most used mathematical equations in the drying process, are listed in Table 1. These equations provide essential information about drying temperature and time [16].

Eq. (1) was used for the calculation of the moisture ratio (MR) of lemon slices;

$$MR = (M_t - M_e) / (M_i - M_e) \quad (1)$$

where MR represents moisture ratio (dimensionless), M_i, M_t, and M_e are the initial moisture content, moisture content at any time, and equilibrium

moisture content of samples, respectively. Compared to M_t and M_i, M_e was ignored due to its very small value, according to those reports by researchers [15,24]. All moisture content was indicated on dry matter (g g^{-1} dry matter).

Eq. (2) was used for the determination of drying rate (DR);

$$DR = (M_{t+\Delta t} - M_t) / \Delta t \quad (2)$$

where $M_{t+\Delta t}$ represents the moisture content at time difference, Δt is the difference of time between two measuring points.

Root mean square error (RMSE), determination coefficient (R^2), and reduced chi-square (χ^2) were the statistical parameters that explain the relationship between predicted and experimental data of lemon slices dried at various microwave powers. It is required to be the lower values of χ^2 and RMSE together with a high value of R^2 for the determination of the best equation predicting experimental data. The RMSE (Eq. 3) and Chi-Square (χ^2) (Eq. 4) values were calculated as follows;

$$RMSE = \left[\frac{1}{N}\sum_{i=0}^{N}\left(MR_{pre,i} - MR_{\exp,i}\right)^2\right]^{1/2} \quad (3)$$

$$\chi^2 = \frac{\sum_{i=0}^{N}\left(MR_{pre,i} - MR_{\exp,i}\right)^2}{N-n} \quad (4)$$

$MR_{pre,i}$ is the predicted MR of mathematical models, $MR_{exp,i}$ is the experimental MR, N and n are the number of observation data and constants of thin-layer drying models [16,25]. All calculations of statistical parameters were determined with SPSS (ver. 22), and the lemon slices drying process modeling was determined using MATLAB (ver. 8.6) curve fitting toolbox.

Determination of the effective moisture diffusivity and activation energy in microwave drying

Fick's second law was used to determine the effective moisture diffusivity as suggested by papers on drying foods [1, 8, 16]. Crank [26] proposed Fick's second law for infinite slab objects with constant moisture diffusivity as Eq. (5).

$$MR = \frac{8}{\pi^2}\sum_{n=1}^{\infty}\frac{1}{(2n-1)^2}\exp\left(-(2n-1)\pi^2\frac{D_{eff}t}{4L^2}\right) \quad (5)$$

The effective moisture diffusivity (D_{eff}) was calculated with Eq. (5), as lemon slices were assumed to be infinite slab material. In Eq. (5), D_{eff} represents the effective moisture diffusivity (m^2 s^{-1}), and L is the half-thickness of the initial size of the sample before drying (m). For simplicity, Eq. (5) can be further simplified to only the first term of the series; thus, Eq. (5) is written in a logarithmic form as given below Eq.(6) [1,16];

$$\ln(MR) = \ln\left(\frac{8}{\pi^2}\right) - \left(\frac{\pi^2}{4L^2}D_{eff}t\right) \quad (6)$$

After the natural logarithm of MR versus drying time (Eq. 6), the plot gives a straight line with a slope as follows Eq. (7) [16,24];

$$Slope = -\frac{\pi^2}{4L^2}D_{eff} \quad (7)$$

Temperature cannot be precisely measured in the microwave dryer, and the reason for this Arrhenius equation was modified as suggested by Özbek and Dadali [27] as given below Eq. (8);

$$D_{eff} = D_0\exp\left(-\frac{E_a m}{P}\right) \quad (8)$$

where m is the initial sample weight, P represents microwave output power, E_a is the activation energy (W g^{-1}), and D_0 is the pre-exponential constant (m^2 s^{-1}) [15,16]. After the transformation of Eq. (8), the new equation is obtained:

$$\ln D_{eff} = \ln D_0 - \frac{E_a m}{P} \quad (9)$$

Natural logarithm of D_{eff} versus the ratio of microwave power to sample weight gives a straight line with a slope representing the E_a.

The second equation for calculation of the E_a is given in Eq. (10) as used by Darvishi *et al.* [1] and Demiray *et al.* [16]. Following the data evaluation, the kinetic rate constant (k) dependence on the ratio of microwave output power to sample weight was represented with an exponential Eq. (10).

$$k = k_0\exp(-\frac{E_a m}{P}) \quad (10)$$

If the natural logarithm of k versus the ratio of microwave output power to sample weight gives a straight line with a slope representing the E_a.

$$\ln k = \ln k_0 - \frac{E_a m}{P} \quad (11)$$

Determination of energy efficiency of microwave drying

To calculate the drying efficiency of microwave (η_d), the required energy to evaporate water from the lemon slices to the energy supplied by the microwave dryer was used [22]. In this context, Eq. (12) was used for calculation;

$$\eta_d = \frac{m_w\lambda_w}{Pt_{on}}100 \quad (12)$$

where m_w is the amount of evaporated water from the lemon samples in kg, P (W) is the power supplied by the microwave dryer, λ_w is the latent heat for vaporiza-

tion of water (2257 kJ kg^{-1}), and t_{on} (s) is the time when the microwave irradiation is on.

Soysal *et al.* [22] and Beaudry *et al.* [23] proposed specific energy consumption as another equation to calculate the energy efficiency of the microwave dryer. Specific energy consumption was determined by using Eq. (13)

$$Q_s = \frac{t_{on}\ P\ 10^{-6}}{m_w} 100 \quad (13)$$

where Q_s is the specific energy consumption required to evaporate a unit mass of water from the product in MJ kg^{-1} water.

RESULTS AND DISCUSSION

Effect of the microwave power on drying rate and time

The variations of moisture content, *MR*, and *DR* of lemon slices dried at various microwave power were presented in Fig. 1.

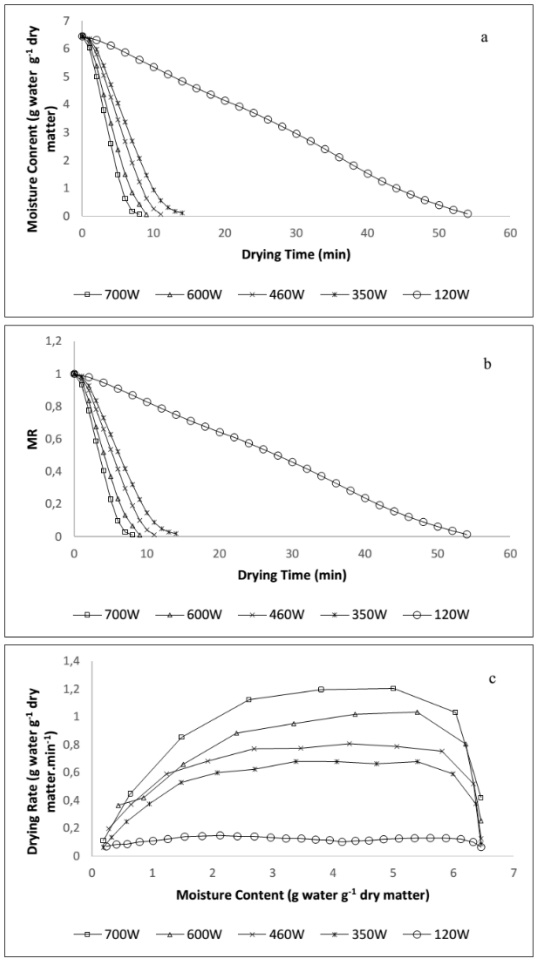

Figure 1. Variation of moisture content (a), MR (b), and DR (c) of lemon slices at various microwave powers.

As seen in Fig. 1, the drying rate increased with microwave power increment. It is a fact that microwave output power has a crucial effect on drying time and drying rate. It was determined that the moisture content of lemon slices reached 7% moisture content (*WB*) at the end of 8, 9, 11, 14, and 54 min at 700, 600, 460, 350, and 120 W, respectively. Likewise, Yogurtcu [28], Demiray *et al.* [16], Zarein *et al.* [15], Polatcı and Taşova [29] have reported increment in the drying rate of various foods based on increasing microwave power which results in a reduction in drying time. In conclusion, more drying rate and lower drying time can be obtained at higher microwave powers due to more heat generation in the sample leading higher evaporation rate [12]. In the initial period of the drying process, a higher drying rate was observed because of high moisture content, which leads to higher microwave absorption. However, despite a higher drying rate at the beginning of the drying process, a falling drying rate period was observed based on the decrement in the moisture content oncoming period. This result was in good accordance with those reported by Aghilinategh *et al.* [30], Çelen *et al.* [31], Azimi-Nejadian and Hoseini [32], and Tepe and Tepe [12]. As presented in Fig. 1, microwave drying consists of three stages. The first is the warming-up stage at the beginning of the drying process. After warming up, rapid drying and falling rate stages follow the first one.

Fitting of microwave drying curves

The thin layer drying models (Table 1) fit the *MR* data of lemon slices dried at various microwave powers.

Table 1. Thin-Layer drying models for microwave drying of lemon slices

Model name	Model	References
Logarithmic	$a\exp(-k\,t) + c$	[12]
Lewis	$\exp(-k\,t)$	
Henderson and Pabis	$a\exp(-k\,t)$	
Page	$\exp(-k\,t^n)$	
Parabolic	$a + b\,t + c\,t^2$	
Wang and Sing	$1 + a\,t + b\,t^2$	

* *a*, *k*, *n*, *b*, and *c* are constants of mathematical models.

The statistical parameters and determination coefficient are given in Table 2. To select the best equation for microwave drying curves of lemon slices, RMSE, χ^2, and R^2 were compared. Among the thin layer models, the highest values of R^2 and the lowest values of RMSE and χ^2 were obtained from the Page model, meaning the Page model gave the best fitting to microwave dried lemon slices. This result showed similarity with findings reported for microwave drying of onion slices, lemon slices, apple slices, and okra [16,28,33,34]. On the other hand, Darvishi *et al.* [1]

Table 2. The values of the thin-layer drying model's constants, RMSE, chi-square, and R^2 for microwave drying of lemon slices

Model	Drying Method, W	Model Constants			χ^2	RMSE	R^2
Lewis	120	k= 0.0303			0.003129	0.0969	0.9058
	350	k= 0.1372			0.009568	0.1220	0.8900
	460	k= 0.1591			0.013300	0.1275	0.8808
	600	k= 0.2035			0.014208	0.1192	0.8978
	700	k= 0.2511			0.017325	0.1241	0.8980
Page	120	k= 0.0024	n= 1.742		0.000517	0.0387	0.9856
	350	k= 0.0174	n= 2.032		0.000099	0.0120	0.9990
	460	k= 0.0221	n= 2.087		0.000276	0.0175	0.9979
	600	k= 0.0428	n= 1.978		0.000171	0.0124	0.9990
	700	k= 0.0564	n= 2.044		0.000294	0.0151	0.9987
Henderson and Pabis	120	k= 0.0349	a= 1.130		0.002459	0.0843	0.9313
	350	k= 0.1607	a= 1.172		0.007531	0.1043	0.9254
	460	k= 0.1855	a= 1.160		0.011451	0.1128	0.9151
	600	k= 0.2323	a= 1.141		0.013195	0.1083	0.9251
	700	k= 0.2823	a= 1.132		0.017600	0.1170	0.9207
Logaritmic	120	k= 0.0357	a= 1.117	c= 0.0143	0.002676	0.0862	0.9281
	350	k= 0.1658	a= 1.155	c= 0.0189	0.008731	0.1079	0.9201
	460	k= 0.1890	a= 1.149	c= 0.0116	0.013174	0.1148	0.9120
	600	k= 0.2362	a= 1.131	c= 0.0103	0.015613	0.1102	0.9224
	700	k= 0.2876	a= 1.121	c= 0.0111	0.021348	0.1193	0.9175
Wang and Singh	120	a= -0.01748	b= -0.000027		0.000069	0.0141	0.9981
	350	a= -0.08424	b= 0.000571		0.002529	0.0605	0.9749
	460	a= -0.08865	b= -0.000719		0.002542	0.0532	0.9812
	600	a= -0.12250	b= 0.000722		0.003336	0.0545	0.9811
	700	a= -0.15810	b= 0.003239		0.005412	0.0649	0.9756
Parabolic	120	a= 1.017	b= -0.01874	c= -0.000008	0.000059	0.0128	0.9985
	350	a= 1.093	b= -0.10990	c= 0.002044	0.001803	0.0490	0.9848
	460	a= 1.073	b= -0.11400	c= 0.001121	0.002049	0.0453	0.9877
	600	a= 1.069	b= -0.15160	c= 0.003272	0.002927	0.0477	0.9873
	700	a= 1.073	b= -0.19250	c= 0.006580	0.005358	0.0598	0.9823

have reported that the Midilli *et al.* model was the best model for describing *MR* of microwave drying of lemon slices. Contrary to these studies, Mosa [35] has recommended the Lewis model as the best describing model of microwave drying of split lemons. Therefore, a comparison of predicted (Page model) and experimental *MR* of lemon slices at various microwave powers were presented in Fig. 2. The predicted and experimental *MR* values showed the straight line, meaning the suitability of the Page model in describing.

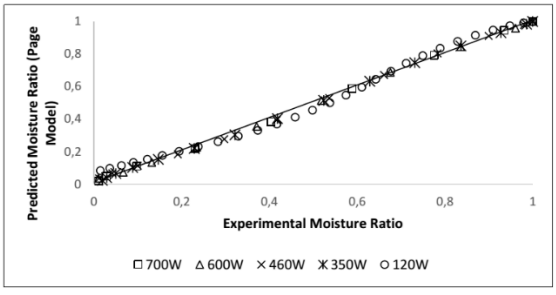

Figure 2. Comparison of predicted MR and experimental MR of lemon slices at different microwave powers.

The effective moisture diffusivity and the activation energy

The values of effective moisture diffusivity and E_a were presented in Table 3. Effective moisture diffusivity of lemon slices ranged from 3.61 10^{-9} to 3.41 10^{-8} m^2 s^{-1}. Increment in microwave power resulted in an increment in effective diffusivity of moisture content of lemon slices. The increment of supplied energy could explain by the microwave dryer. Absorption of higher energy by water molecules at higher microwave powers increases the evaporation rate of water. Similar to this study, Darvishi *et al.* [1] have reported an increment in effective moisture diffusivity with the increasing microwave power during microwave drying of lemon slices. It was also stated that the D_{eff} values of lemon slices ranged from 1.87 10^{-8} to 3.95 10^{-8} m^2 s^{-1} by Darvishi *et al.* [1]. Likewise, effective moisture diffusivity has also been reported for drying apples and *Eriobotrya japonica* L. with different microwave powers [15,29].

The E_a of lemon slices was found in two different equations. The natural logarithm of the values of D_{eff} versus the ratio of microwave power to sample weight (Eq. 9) gives a straight line with a slope, and the slope represents the E_a. The E_a of lemon slices calculated by Eq. (9) was 4.39 W g^{-1}. The Arrhenius relation between the D_{eff} and the sample weight/microwave power is given in Fig. 3.

Drying rate constants of the best fitting Page model were used to calculate the E_a. The E_a of lemon slices was estimated by using Eq. (11). The values of E_a were calculated at 6.04 W g^{-1}. The Arrhenius type relation of k versus sample weight/microwave power is presented in Fig. 4.

Energy efficiency and specific energy consumption of microwave drying

Cumulative energy efficiency and specific energy consumption values for microwave drying of lemon slices were given in Table 3. While the highest cumulative energy efficiency value of 46.14% was calculated at the 460 W microwave, the lowest value of cumulative energy efficiency of 34.53% was obtained at 120 W microwave power. No mean differences were found between the cumulative energy efficiency values of 700 and 600 W ($p>0.05$). This result shows that the highest microwave power may not be selected as the correct drying power when investigating energy efficiency. As addressed above, drying time at 460 W was nearly the same as those at 600 W and 700 W.

However, the energy efficiency at 460 W was higher than those at 600 and 700 W. In that study, 460 W may be the best power option in light of this result.

Table 3. Effective moisture diffusivity, activation energy, pre-exponential constants, specific energy consumption and cumulative drying efficiency of microwave dried-lemon slices

Microwave Power, W	D_{eff} (m^2 s^{-1})	E_a (W g^{-1})	E_a (W g^{-1})	Q_s (MJ kg^{-1})	η_d (%)
120	3.61x10^{-9}	6.04^t	4.39^r	6.53^a (±0.05)	34.53^a (±0.02)
350	1.74x10^{-8}			5.57^b (±0.03)	40.48^b (±0.02)
460	2.18x10^{-8}			4.89^c (±0.03)	46.14^c (±0.02)
600	2.68x10^{-8}			5.44^d (±0.04)	41.46^d (±0.04)
700	3.41x10^{-8}			5.45^d (±0.04)	41.40^d (±0.02)

* *The same letters within the same row are not significantly different at a probability ($p<0.05$). Values in parenthesis indicate standard deviation.* ^{t} *- the activation energy calculated using the equation* $k=k_0 \exp(-E_a\ m\ P^{-1})$, *where k values were obtained from Page model.* ^{r} *- the activation energy calculated by* $D_{eff}=D_0 \exp(-E_a\ m\ P^{-1})$.

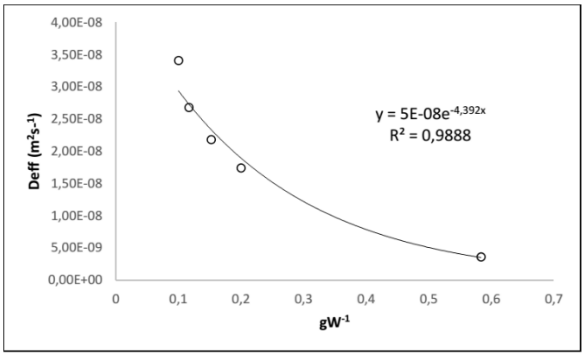

Figure 3. Arrhenius-type relation between D_{eff} and sample weight/microwave power

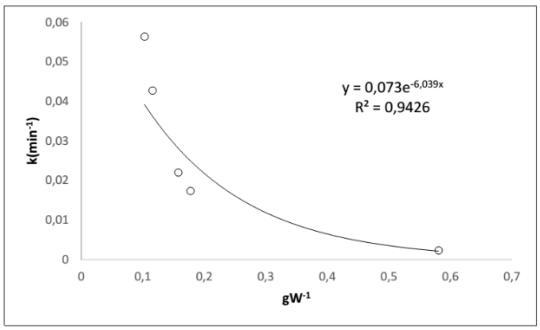

Figure 4. Arrhenius-type relation between the values of k (Page model) versus sample weight/microwave power.

Soysal *et al.* [22] have reported that the value of cumulative energy efficiency of 75 g parsley sample dried at 900 W microwave power was 46.48%. On the other hand, the highest specific energy consumption was determined at 120 W microwave power as 6.53 MJ kg^{-1} water. On the contrary, the lowest value of specific energy consumption was obtained at 460 W microwave power as 4.89 MJ kg^{-1} water. Therefore, it can be seen that energy efficiency increased as specific energy consumption statistically decreased ($p<0.05$).

CONCLUSION

The effect of microwave powers on drying characteristics, energy efficiency, and specific energy consumption in microwave-dried lemon slices was investigated. The lemon slices' drying time and drying rate were significantly affected by the increment in microwave power. Higher microwave power reduces drying time and increment in drying rate. On the other hand, effective moisture diffusivity increased with microwave power. Effective moisture diffusivity of lemon slices ranged from $3.61x10^{-9}$ to $3.41x10^{-8}$ m^2 s^{-1}. The E_a of lemon slices was calculated with the exponential Arrhenius equation with D_{eff} and rate constant (k) obtained from the Page model as 4.39 W g^{-1} and 6.04 W g^{-1}, respectively. Page model suitably describes the curve of microwave drying of lemon slices. Additionally, energy efficiency is related to specific energy consumption. Energy efficiency increased as specific energy consumption decreased. Nowadays, food processes requiring energy, such as drying, should be designed by considering energy efficiency. In this study, 460 W was the best power with 11 min of drying time, the highest energy efficiency, and the lowest specific energy consumption. However, the highest microwave power may not always be the best option for the drying process.

REFERENCES

[1] H. Darvishi, M. H. Khoshtaghaza, S. Minaei, Int. Agrophys. 281 (2014) 1–6.

[2] O. M. Kesbi, M. Sadeghi, S. A. Mireei, Eng. Agric. Environ. Food 93 (2016) 216–223.

[3] J. Wang, C. L. Law, P. K. Nema, J. H. Zhao, Z. L. Liu, L. Z. Deng, Z.J. Gao, H. W. Xiao, J. Food Eng. 224 (2018) 129–138.

[4] M. Sadeghi, O.M. Kesbi, S. A. Mireei, J. Sci. Food Agric. 933 (2013) 471–478.

[5] M. Torki-Harchegani, M. Ghasemi-Varnamkhasti, D. Ghanbarian, M. Sadeghi, M. Tohidi, Heat Mass Transf. 522 (2016) 281–289.

[6] P. K. Wankhade, R. S. Sapkal, V. S. Sapkal, Procedia Eng. 51 (2013) 371–374.

[7] M. Zhang, J. Tang, A. S. Mujumdar, S. Wang, Trends Food Sci. Technol. 1710 (2006) 524–534.

[8] A. O. Omolola, A. I. Jideani, P. F. Kapila, Int. J. Agric. Biol. Eng. 76 (2014) 107–113.

[9] A. Fijalkowska, M. Nowacka, A. Wiktor, M. Sledz, D. Witrowa-Rajchert, J. Food Process Eng. 393 (2016) 256–265.

[10] C. Ricce, M. L. Rojas, A. C. Miano, R. Siche, P. E. D. Augusto, Food Res. Int. 89 (2016) 701–708.

[11] R. L. Monteiro, B. A. Carciofi, J. B. Laurindo, J. Food Eng. 178 (2016) 1–11.

[12] T. K. Tepe, B. Tepe, Heat Mass Transf. 56(11) (2020) 3047–3057.

[13] J. Srikiatden, J. S. Roberts, Int. J. Food Prop. 10(4) (2007) 739–777.

[14] X. D. Chen, A. S. Mujumdar, X. D. Chen, A. S. Mujumdar (Eds.) Drying technologies in food processing. Blackwell, Oxford (2008).

[15] M. Zarein, S. H. Samadi, B. Ghobadian, J. Saud Soc. Agric. Sci. 141 (2015) 41–47.

[16] E. Demiray, A. Seker, Y. Tulek, Heat Mass Transf. 535 (2017) 1817–1827.

[17] J. R. D. J. Junqueira, J. L. G. Corrêa, D. B. Ernesto, J. Food Process. Preserv. 41 (2017) e13250.

[18] C. Kumar, M. U. H. Joardder, T. W. Farrell, G. J. Millar, M. A. Karim, Drying Technol. 34(8) (2016) 962–973.

[19] S. Chandrasekaran, S. Ramanathan, T. Basak, Food Res. Int. 52(1) (2013) 243–261.

[20] H. Darvishi, M. Azadbakht, A. Rezaeiasl, A. Farhang, J. Saud Soc. Agric. Sci. 122 (2013) 121–127.

[21] D. I. Onwude, N. Hashim, R. B. Janius, N. M. Nawi, K. Abdan, Compr. Rev. Food Sci. Food Saf. 15 (2016) 599–618.

[22] Y. Soysal, S. Öztekin, Ö. Eren, Biosystems Eng. 934 (2006) 403–413.

[23] C. Beaudry, G. S. V. Raghavan, T. J. Rennie, Drying Technol. 219 (2003) 1797–1810.

[24] J. Bi, A. Yang, X. Liu, X. Wu, Q. Chen, Q. Wang, X. Wang, LWT-Food Sci. Technol. 602 (2015) 1136–1142.

[25] M. Śledź, M. Nowacka, A. Wiktor, D. Witrowa-Rajchert, Food Bioprod. Process. 914 (2013) 421–428.

[26] J. Crank, Mathematics of Diffusion, Clarendon Press, Oxford (1975).

[27] B. Özbek, G, Dadali J. Food Eng. 83(4) (2007) 541–549.

[28] H. Yoğurtçu, Fırat Üniv. Eng. Sci. J. 261 (2014) 27–33.

[29] H. Polatci, M. Taşova, Anadolu Agric. Sci. J. 332 (2018) 124–130.

[30] N. Aghilinategh, S. Rafiee, A. Gholikhani, S. Hosseinpur, M. Omid, S.S. Mohtasebi, N. Maleki, Food Sci. Nutr. 3(6) (2015) 519–526.

[31] S. Çelen, A. Haksever, A. Moralar, Karaelmas Sci. Eng. J. 7(1) (2017) 228–236.

[32] H. Azimi-Nejadian, S.S. Hoseini, Heat Mass Transf. 55(10) (2019) 2921–2930.

[33] G. Dadali, E. Demirhan, B. Özbek, Food Bioprod. Process. 86(4) (2008) 235–241.

[34] Z. Wang, J. Sun, X. Liao, F. Chen, G. Zhao, J. Wu, X. Hu, Food Res. Int. 40(1) (2007) 39–46.

[35] M. Mosa, J. Soil Sci. Agric. Eng.10(4) (2019) 259–265.

FADIME BEGÜM TEPE[1]
TOLGA KAĞAN TEPE[1]
AYTEN EKINCI[2]

[1]Department of Food Technology, Şebinkarahisar Vocational School of Technical Science, Giresun University, Giresun, Turkey

[2]Department of Food Technology, Denizli Vocational School of Technical Science, Pamukkale University, Denizli, Turkey

NAUČNI RAD

KINETIKA I ENERGETSKA EFIKASNOST MIKROTALASNOG SUŠENJA KRIŠKI LIMUNA

U ovoj studiji, kriške limuna su sušene u mikrotalasnoj pećnici pri različitim snagama (120, 350, 460, 600 i 700 W) da bi se utvrdile karakteristike sušenja i energetska efikasnost. Na brzinu i vreme sušenja značajno je uticalo povećanje snage mikrotalasne pećnice. Najniže i najveće vreme sušenja bilo je 8 min i 54 min na 700 W i 120 W, redom. Brzina sušenja se povećava, a vreme sušenja skraćuje sa povećanjem snage mikrotalasne pećnice. Najpogodniji model za opisivanje krivih mikrotalasnog sušenja kriški limuna je model Pejdža. Vrednosti D_{eff} za kriške limuna su između $3{,}61\times10^{-9}$ and $3{,}41\times10^{-8}$ m^2s^{-1}. E_a sušenja kriški limuna, izračunata korišćenjem D_{eff}, i konstanta brzine iz modela Pejdža su 4.39 Wg^{1} and 6.04 Wg^{1}, redom. Pored toga, što je veća kumulativna energetska efikasnost, to je niža specifična potrošnja energije. Najmanja specifična potrošnja energije i najveća energetska efikasnost izračunate su za 460 W. Pri snazi od 460 W vreme sušenja je 11 min, energetska efikasnost je najveća, a specifična potrošnja energije najmanja.

Ključne reči: kriške limuna, karakteristike sušenja, mikrotalasno sušenje, efektivna difuzija, energetska efikasnost.

CI&CEQ
Chemical Industry & Chemical Engineering Quarterly

Available online at
Association of the Chemical Engineers of Serbia AChE
www.ache.org.rs/CICEQ

Chem. Ind. Chem. Eng. Q. 28 (4) 305–317 (2022) CI&CEQ

H. BATUHAN OZTEMEL
INCI SALT
YAVUZ SALT

Department of Chemical Engineering, Faculty of Chemical and Metallurgical, Yildiz Technical University, Istanbul, Turkey

SCIENTIFIC PAPER

UDC 502/504:546.2.264-31:662

CARBON DIOXIDE UTILIZATION: PROCESS SIMULATION OF SYNTHETIC FUEL PRODUCTION FROM FLUE GASES

Article Highlights

- Capacities were assumed regarding the emissions and number of industrial power plants worldwide
- Asymmetric polyethersulfone hollow fiber membrane separates CO_2 and N_2 gases from flue gas
- Sulfurization, reverse water-gas shift, and Fischer-Tropsch reactions separate the flue gas
- The synthetic fuel produced is mainly composed of hydrocarbons such as methane, ethane, and butane
- Each cost of equipment is calculated in the profitability analysis

Abstract

Environmental problems are on the rise and nowadays more climate-related, caused primarily by greenhouse gas emissions. Also, worldwide industrial emissions from power plants will cause 50% of the carbon dioxide concentration in the atmosphere by 2035. The simulation study of the synthetic fuel production from flue gas emitted by industrial power plants uses the ChemCAD Software. The study aims to reproduce all flue gas constituents into valuable products to reduce the effects of harmful gases on the environment. The synthetic fuel produced consists of 94.75% hydrocarbons with carbon numbers ranging from 1 to 4 with a 6.59% overall conversion rate. 95% of the sulfur content in flue gas is collected by desulfurizing the fuel mixture. The membrane process also recovers 90.3% of the nitrogen gas in the flue gas. Sulfurization, Reverse Water Gas-Shift, and Fischer-Tropsch syntheses have 95%, 79%, and 98.4% single-pass conversions, respectively, with appropriate catalysts. Economic analysis is also performed, and the payback period of the project is 6.1 years, while the return-on-investment rate is 16.64%.

Keywords: carbon dioxide, Fischer-Tropsch synthesis, flue gas, process simulation, synthetic fuel.

Especially in recent decades, the world has been facing critical environmental problems, such as global warming and depletion of the ozone layer, according to the UN Environment Annual Report 2019 [1]. Besides, acidification in oceans has increased and already affects many ocean species [2]. These environmental issues typically result from carbon dioxide, a well-known greenhouse gas.

Global warming is the continuous increments in the average temperature of the Earth's climate system due to anthropogenic impacts, for instance, the emission of greenhouse gases such as CO_2, CH_4, NO_x, CF_4, etc. [3,4]. Besides, the global temperature continuously increased after the 1880s. The CO_2 increase mainly caused this growth trend. The usage of heavy-duty machines during the industrial revolution was the key point of these rises. Nonetheless, CO_2 has no direct pay-off on the ozone layer, unlike CFCs (Chlorofluorocarbons) and HFCs (Hydrofluorocarbons). However, higher levels of CO_2 have an indirect pay-off on the ozone layer, as said by the Minnesota Pollution Control Agency [5]. The objective of the ozone layer is

Correspondence: Y. Salt, Department of Chemical Engineering, Faculty of Chemical and Metallurgical, Yildiz Technical University, Davutpasa Campus, 34220 Esenler-Istanbul, Turkey.
E-mail: salt@yildiz.edu.tr
Paper received: 25 October, 2021
Paper revised: 13 March, 2022
Paper accepted: 21 April, 2022

https://doi.org/10.2298/CICEQ211025005B

the filtration of the sunlight. According to the measurements, large holes in the ozone layer critically affect living creatures and nature, glaciers, and oceans by Gunduz [6]. Severe forest fires in the last decade, such as the Australian wildfires in 2020, are also the drawbacks of these anthropogenic applications. Furthermore, oceans perform a vital role in transferring CO_2 into the atmosphere. Over the past 200 years, the oceans have absorbed about half of the CO_2 emitted by anthropogenic applications, as reported by Kolieb and Herr [7].

Emission growth and past solutions

According to Bereiter *et al.* [8], CO_2 concentrations in the atmosphere did not exceed 300 ppm for the last 800,000 years. However, it is well over 400 ppm today and keeps increasing. Hence, today's concentrations are the highest for at least 800,000 years. Since the beginning of the industrial revolution, global CO_2 concentration in the atmosphere has increased. The primary reason for the increment was the growth of heavy-duty machines. These industrial machines were notably beneficial during the industrial revolution. However, they were discharging a high amount of CO_2. The prediction of the CO_2 concentration of each region between 2000 and 2035, using the statistical approach conducted for the input assumption, is shown in Fig. 1. Asia region has had the highest emission rate since the 2000s. The exponential smoothing technique was used for all forecasts in this study to predict possible CO_2 concentrations in different segments. The predictions show these emission rates will consistently increase. Therefore, the CO_2 increment must be solved globally since it threatens the whole ecology. This trend is mainly caused by the increasing energy demand and global fossil fuel consumption. Natural gas, which meets one-third of total energy demand, is the fastest-forming fossil fuel and generates the highest carbon emissions worldwide, as Ozturk and Dincer [9] said. As IEA (International Energy Agency) Statistics [10] reported, a major part of the CO_2 discharge comes from flue (or stack) gases released excessively from industrial power plants.

A few principal areas contribute to worldwide CO_2 emission: agriculture, buildings, industrial power plants, transportation, land use, and forestry. For example, the emissions caused by only industrial power plants at the beginning of the 2000s were 22% of all kinds of CO_2 emissions.

However, this percentage will be approximately 41% by 2035. Besides, G20 countries were responsible for around 80% of these emissions [11]. The highest CO_2 industrial emissions from power plants (excluding

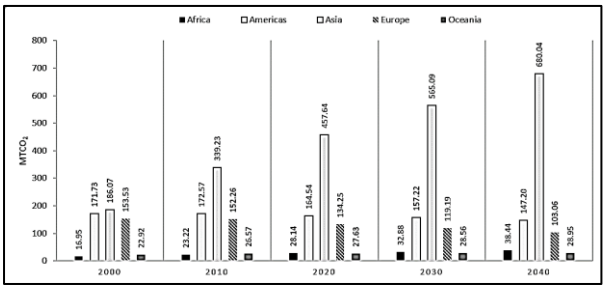

Figure 1. Prediction of CO_2 concentration by region ($MtCO_2e$/year). (Reproduced from IEA Statistics [10]).

buildings, transportation, and other fugitive emissions) of all G20 countries were recorded by China. It was followed by the United States and the EU [12].

Flue gas (or exhaust gas) is the gas that emits from power plants and includes the reaction outputs of combustion air and residual substances such as particulate matter (dust), sulfur oxides, nitrogen, and carbon monoxide [13]. Facilities that operate with high energy duties and emit excessive flue gas will be the focal point of this study since the CO_2 percentage in typical flue gas is relatively high. Many studies have treated flue gas as a waste of mist at high temperatures, such as oxyfuel combustion and chemical looping, namely carbon capture techniques. There are different techniques to reduce CO_2 emissions, such as boosting renewable energies, applying regulations on CO_2 emission, treating CO_2 as raw material, enhancing plant efficiency to be more energy-saving, or applying carbon capture and storage (CCS) technology. Renewable energies still need to be developed to compete economically with fossil fuels. Novel implementations and usages of sustainable fossil fuels require an integration of the CCS technologies regarding the increasing global energy demand [14]. CCS involves catching the CO_2 at its emission sources, such as coal, petroleum, or natural gas, and transporting it to storage. Oxyfuel combustion is one of those techniques. In this technology, fuel is burned utilizing an oxidizer mixture of pure oxygen and recycled flue gases, comprised mainly of CO_2 and H_2O. The process results in high CO_2-concentrated exhaust gas, which facilitates the capture process of CO_2 after H_2O condensation [15]. Therefore, flue gas can be used as the oxyfuel propagator, as Liang *et al.* [16] stated. The distinguished CO_2 and H_2O gases from the recycled flue gas were used as a diluent to control the temperature in the oxyfuel system. In this regard, the objective is to achieve high-efficiency power generation with low-cost carbon capture. Another common technique is chemical looping which has the same working principle as the oxyfuel method. Chemical looping or chemical looping combustion has no direct contact with air or fuel. It is a method that provides the CCS without vital efficiency or cost penalties. Oxygen

is extracted from the air and then reacts with the hydrocarbon fuel, producing exhaust gases mainly composed of CO_2 and H_2O gases. The water vapor condenses from the gas resulting in a near 100% CO_2 stream [17]. Osman *et al.* [18] have reviewed three aspects of the pressurized operation of chemical looping processes, which create the basis for power and chemical production with integrated CO_2 capture. Pressurized operation of the chemical looping process is essential to maximize thermodynamic and economic performance.

Besides these techniques, biochemical solutions provide the world with a more sustainable future, such as microalgae technology to capture CO_2 from flue gases. Vuppaladadiyam *et al.* [19] suggest that using microalgae cultivation systems to fix CO_2 from industrial flue gases shows favorable results, owing to its potential for producing value-added products, for instance, biodiesel and bioethanol. Also, Kothari *et al.* [20] focus on the algal biomass production techniques and how to accomplish algal biofuel production in an integrated system provided with CO_2 from power plants and wastewater treatment by suitable microalgal species. However, practical applications of these technologies at an industrial scale require significant research and involve high capital costs, although the long-term benefits cut down these prices.

Negligence and lack of use of byproducts (such as flue gas) lead to the techno-economical failure of the process and cause environmental problems [21]. Therefore, the objective of this study is not only to reduce CO_2 emissions but also to create a sustainable fuel model. In other words, the focal point is to reduce both environmental problems and fuel scarcity.

Flue gas emitted from power plant A (other power plants near our process) is supplied to power plant B (the process in this study) to produce synthetic fuel. Flue gas is then cooled and condensed to distinguish the excess water in power plant B. Most nitrogen separated from the mixture after flowing through the parallel-linked membrane system. The remained mixture was treated with the sulfurization reaction to eliminate sulfur content. Then, the CO_2-rich mixture flowed into the reverse water gas-shift (RWGS) and Fischer-Tropsch (F-T) reactors with hydrogen feed. End-products, such as synthetic fuel, nitrogen, elemental sulfur, and excess water, were obtained at the reactor outlet (preliminary economic analysis was performed to emphasize the feasibility of the design). The produced synthetic fuel is recycled back to power plant A.

Consequently, power plant A does not emit CO_2 to the atmosphere since all flue gases are absorbed by power plant B (the process in this study). Furthermore, power plant A will require fewer external fuels, such as natural gas or coal, since there is a continuous flow of synthetic fuel to power plant A.

METHODOLOGY AND SIMULATION DETAILS

Facility considerations

Site construction and operations should be installed alongside other industrial power plants. The requirement of being closer to those plants is to reduce the transportation cost. There are two reasons: 1) The flue gas of other industrial facilities must be continuously fed into the process. 2) The synthetic fuel produced should be efficiently delivered to other power plants. The continuous recirculation occurs in the zero-emission, as shown in Fig. 2. In this regard, power plants use an environmental-friendly fuel source with sufficient calorific value. In the meantime, other value-added products will be produced and marketed.

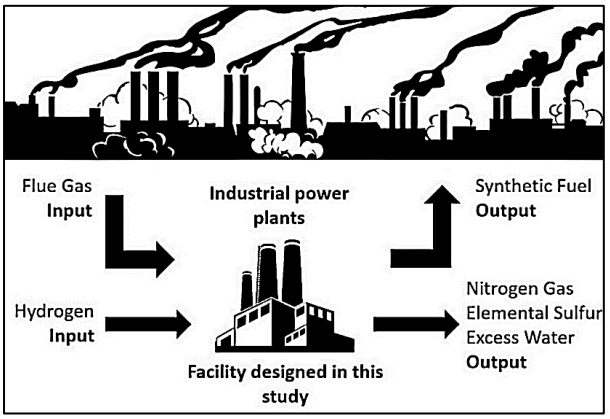

Figure 2. Representation of general perspective.

The inlet flue-gas-flow rater can be estimated by several methods. The mathematical formula of the flow rate by taking the parameters of chimney dimensions was introduced by Ortega [22]. Eq. (1) assumes the flue gas rate in natural ventilation by using a typical chimney's differences in inlet and outlet temperatures. Eq. (1) gives the flue gas flow rate emitted by a chimney, q, in which C_d is the discharge coefficient that is ordinarily taken as 0.65, T_i and T_o are the inlet and outlet temperatures. A is the cross-sectional area of the chimney, and H is the height of the chimney, which were assumed through dimensions of moderate chimney according to Simonovic *et al.* [23].

$$q = C_d A \sqrt{2gH \frac{T_i - T_0}{T_i}} \quad (1)$$

However, the input assumption was achieved using the statistical approach. Based on the CO_2 emission rate of each country and the number of factories in that country, the average amount of flue gas emitted from a typical factory was calculated as approximately 56.46 kilograms per second. According

to the energy type used (gas, coal, renewables, biomass, etc.) by power plants, the CO_2 amount emitted by those factories also changes, and this is also taken into consideration. Since this study aims to encourage environmental-friendly production and consumption, only the gases emitted by coal- and gas-fired plants are involved in the statistical approach. Besides, inlet conditions of flue gases by post-combustion fossil fuel-fired power plants are given in Table 1 [24].

Table 1. Inlet conditions of flue gases (Reproduced from Arachchige and Melaaen [24], with permission from Elsevier)

Flue gas type	Coal-Fired	Gas-Fired
Temperature (°C)	40	40
Pressure (kPa)	110	110
Flow rate (kg/s)	56.46	
Composition	w/w (%)	
H_2O	5.08	5.09
N_2	70.4	75.1
CO_2	20.6	6.21
O_2	3.90	13.5
H_2S	0.06	0

Process design

The overall process flow diagram is shown in Fig. 3. The excess water in flue gas is first distinguished by flash distillation to provide a non-aqueous mixture for membrane separation. The hollow fiber membranes separated about 95% of the nitrogen, and then the mainstream, which mainly contains CO_2, treated with sulfurization reaction occurred in R-201. Desulfurized CO_2-rich stream combined with hydrogen gas before the reverse water gas shift reactor (R-202). The syngas containing CO and H_2 gases were separated from the unreacted CO_2. The unreacted CO_2 gas was recycled back to combine with the R-202 inlet. Then, highly reactive syngas with 600 °C was involved in the Fischer-Tropsch synthesis in R-203 to produce the synthetic fuel. Throughout the process, the excess water was distinguished and directly bypassed. The process simulated is constituted mainly by hydrocarbon systems, and the pressure of the system is higher than 100 kPa. Thus, Soave-Redlich-Kwong (SRK) equilibrium is used because it is an appropriate thermodynamic equation of state (EOS) for this process [25].

Membrane separation process

Aaron and Tsouris [26] indicate that around 7 gigatons of carbon spread every year. Therefore, the CCS and reduction of CO_2 emissions is an important area of research. There are several methods for CCS: Liquid absorption with a monoethanolamine (MEA) such as amine scrubbing process, cryogenic distillation, membrane process, pressure- or temperature swing adsorption using various solid sorbents, algae-based uptake, etc. In liquid absorption, CO_2 is obtained and collected in the regeneration column after a solvent is utilized that dissolves CO_2, but not nitrogen gas or any other components in the flue gas. Aaron and Tsouris [26] also concluded that liquid absorption using MEA is a promising technology among these methods; however, the recent developments of membrane technologies produce significant efficiency in the separation of CO_2.

Regarding the complexity, energy consumption, and high capital costs of these technologies, membrane separation is an appropriate capture process due to its high efficiency, easy scale-up, and low energy consumption. Common membranes for CO_2 capture can be summarized as polymeric, inorganic, carbon, and mixed matrix membranes [27]. CO_2 separation using biopolymer-based membranes is one of the new studies in sustainable membrane technologies within the scope of green process engineering [28]. Song *et al.* [29] reported that the polyethersulfone (PES) membranes have excellent stability and high separation performance for CO_2 separation from a gas mixture. Therefore, the membrane module formed by the asymmetric PES hollow fibers is suitable for CO_2 separation. The hollow fiber membrane type was also preferred due to its high membrane surface area and packing density. Due to the CO_2, N_2, and O_2 separation challenge, Song *et al.* [29] used a multiple membrane stage process with four membrane modules linked in a parallel structure to distinguish the components efficiently. However, two membrane modules were combined in the same manner, as shown in Fig. 4.

The general properties of each stream that flowed through both membranes, M-101 and M-102, were summarized in Table 2. In addition, CO_2/N_2 ratio by weight compositions was also given to indicate the performance of the membrane process.

Apart from the membranes, flash separators were used for equilibrium separations. Equilibrium flash separation is typical equipment used in industries, especially in the petroleum industry. A feed stream is separated into liquid and vapor streams in an equilibrium flash vaporization or flash distillation. According to Towler and Sinnott [30], the feed stream to the flash vessel must be in neither liquid nor gas state but in both states. The separation of feed liquid droplets and mists from the gas component is feasible whenever the temperature of the vapor is reduced below the dew point. Thus, the necessary heat must be given to the mainstream or removed from it to bring the stream to

C-101 Feed Compr.	E-101/2 Flue Gas Coolers	V-101 L/V Separator	M-101/2 Membranes	C-102/3 Membrane Compr.	E-103/4 Heaters	V-102/3 L/V Separators	H-101/2/3 Pre-Reactor Furnaces	R-201 Sulfurization Reactor	E-201 Post-Reactor Heater	V-201 Sulfur Separator
R-202 RWGS Reactor	E-202/3 Heaters	R-203 F-T Reactor						V-202/3 L/V Separators	V-204/5 L/V Separators	E-204/5 Coolers

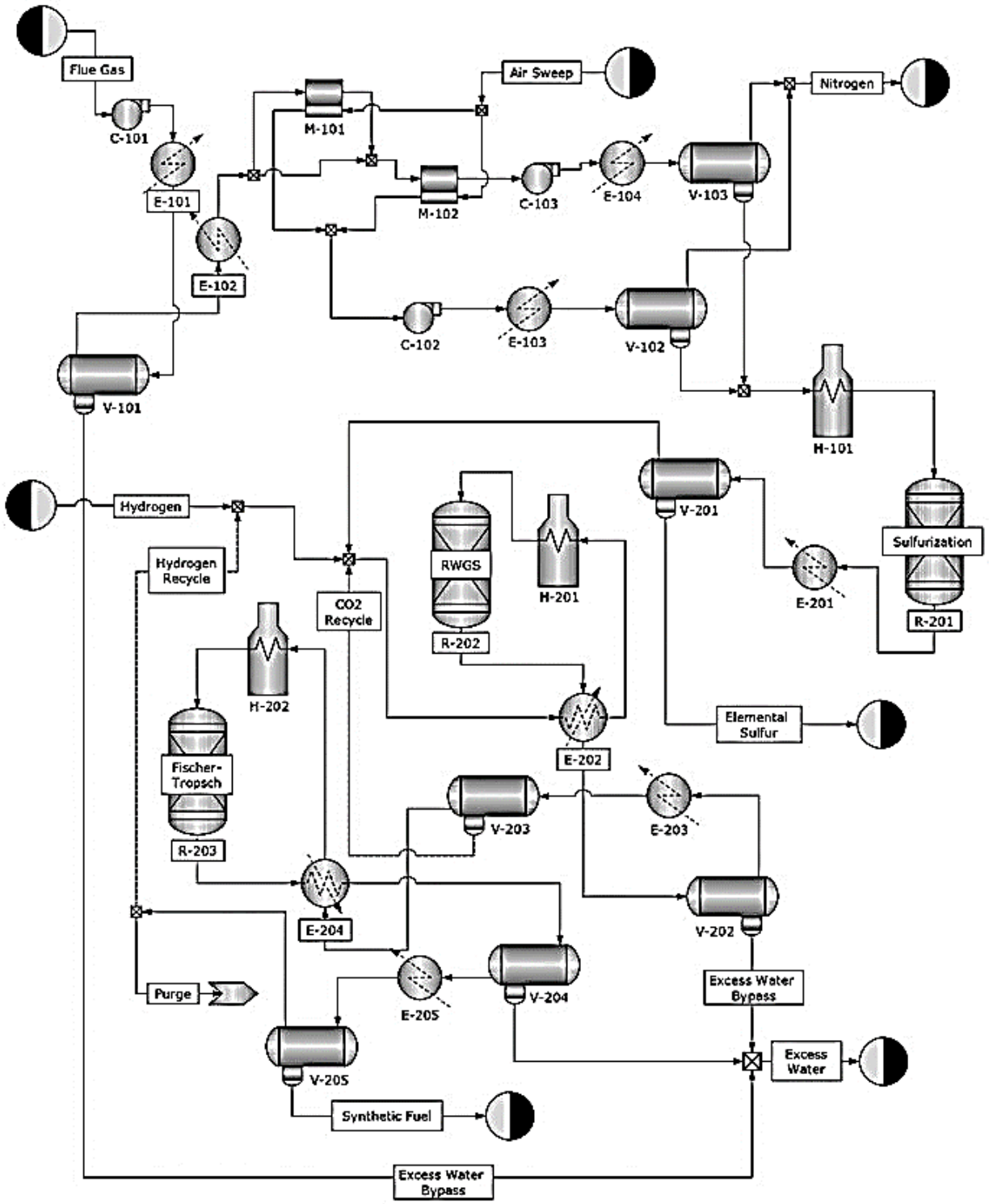

Figure 3. Process flow diagram of the proposed solution.

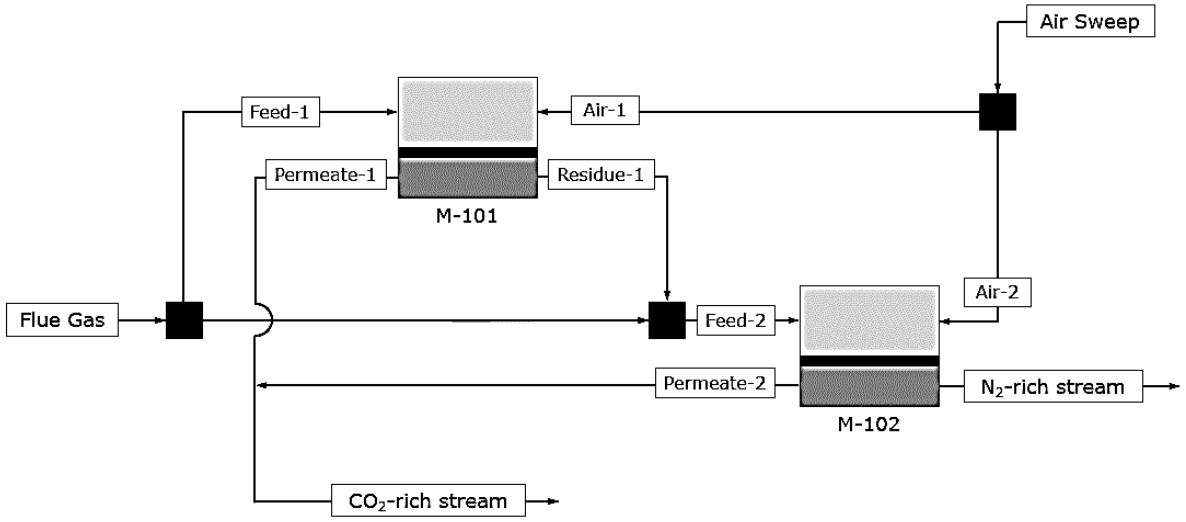

Figure 4. Diagram of the multiple-stage membrane system.

Table 2. Stream properties of the membrane process

	Flue Gas	Feed-1	Permeate-1	Air-1	CO_2-rich stream
Flow Rate (kg/s)	53.6	26.8	7.6	0.99	13.8
Temperature (°C)	27	27	17.1	25	17.7
Pressure (kPa)	2000	2000	102.6	202.6	102.6
CO_2/N_2 (w/w)	0.29	0.29	1.74	0	1.58
	Residue-1	Feed-2	Permeate-2	Air-2	N_2-rich stream
Flow Rate (kg/s)	20.2	47	6.2	0.99	41.8
Temperature (°C)	26.5	26.4	18.4	25	25.9
Pressure (kPa)	1800	1800	102.6	202.6	1600
CO_2/N_2 (w/w)	0.06	0.18	1.40	0	0.10

suitable "gas-liquid" separation conditions. The composition of the final streams depends on the quantity of the feed vaporized (flashed).

Equilibrium separations require low-temperature levels, whereas the reaction conditions need to be relatively high. As a result, there are increased energy requirements and heat transactions throughout the process. Therefore, heat exchanger selection is essential. Shell and tube heat exchangers are widely used in oil refineries and the petrochemical industry. The fixed tube and type BEM heat exchanger is relatively cost-effective in the petrochemical industry. The operation mechanism of the fixed tube and BEM type exchangers is simple. The setup and repair of these exchangers are also easier [31]. Besides, liquid nitrogen was preferred as a coolant component of coolers, whose working principle is assumed to be a cryogenic operation. Medium-pressure (MP) steam was used as a heater fluid in E-102. Rhine and Truelove indicated the maximum heat duty allowance for heaters should be between 3 MW and 100 MW. However, the heaters used in the petroleum industry can be around 300 MW or more with 20 MPa maximal pressure [32].

On the other hand, there are three reactors in the process. These reactors were used for sulfurization, the reverse water gas shift, and Fischer-Tropsch synthesis. Simulation and design parameters for each reactor, such as type of reactors, volumes occupied, reaction phase, thermal (or operation) mode and the catalysts used in reactors, and equipment properties in the simulation, are shown in Table 3.

Sulfurization reaction

Sulfur-containing components have destructive impacts on the environment. Hence, the International Organization for Standardization has limited the maximum sulfur content from 3 mg/kg to 500 mg/kg in typical fuels [33].

Table 3. Equipment properties in the simulation

Exchangers	Inlet Temp. ℃	Pressure, kPa	ΔT, ℃	Type	Heat Duty, MW	Calc. Area, m^2
E-101	707	2000	-702	Fixed-Tube, BEM	-52.32	366.2
E-102	5	2000	22	Fixed-Tube, BEM	1.23	4.3
E-103	276	1000	-406	Fixed-Tube, BEM	-8.9	90
E-104	4	1000	-126	Fixed-Tube, BEM	-7	279.6
E-105	-130	1000	-830	Fixed-Tube, BEM	14.80	103.58
E-201	690	1000	-540	Fixed-Tube, BEM	-7	9.4
E-202	892	1000	-882	Fixed-Tube, BEM	-889.5	1773
E-203	10	1000	-180	Fixed-Tube, BEM	-171.5	1167.3
E-204	600	1000	-595	Fixed-Tube, BEM	-584.7	1569.3
E-205	5	1000	-205	Fixed-Tube, BEM	-190.7	2068
Reactors	Temp. ℃	Pressure, kPa	Reaction(s)	Type	Mode	Calc. Volume, m^3
R-201	691	1000	Sulfurization	Equilibrium	Adiabatic	1.5
R-202	892	1000	RWGS	Shift	Adiabatic	20.2
R-203	600	1000	Fischer-Tropsch	Equilibrium	Isothermal	389.4
Membranes	Press, kPa	Flow Pattern	Fiber Length, m	Type	No. of Fibers	Surface Area, m^2
M-101	2000	Counter Current	1.5	Hollow Fiber	10000	21.99
M-102	1800	Counter Current	1.5	Hollow Fiber	10000	21.99
Compressors	Temp,℃	Efficiency, %	ΔP, kPa	Type	Actual Power, MW	
C-101	150	80	1890	Reciprocating	36.23	
C-102	18	80	897	Reciprocating	3.52	
C-103	26	80	600	Reciprocating	-1.25	
Furnaces	Inlet Temp. ℃	Pressure, kPa	ΔT, ℃	Type	Heat Duty, MW	
H-101	-130	1000	830	Process Heater	14.81	
H-201	-169	1000	1069	Process Heater	1066	
H-202	-170	1000	770	Process Heater	741.4	
Separators	Temp,℃	Pressure, kPa	Product Separated	Type		
V-101	5	2000	Excess H_2O	Flash Distillation		
V-102	-130	1000	Liquid N_2	Flash Distillation		
V-103	-130	1000	Liquid N_2	Flash Distillation		
V-201	150	1000	Elemental S_2	Flash Distillation		
V-202	10	1000	Excess H_2O	Flash Distillation		
V-203	-170	1000	Excess CO_2	Flash Distillation		
V-204	5	1000	Excess H_2O	Flash Distillation		
V-205	-200	1000	Synthetic Fuel	Flash Distillation		

On the other hand, hydrogen sulfide content in typical flue gas (Table 1) was substantial at 0.1%. Thus, the elemental sulfur was produced in R-201 to distinguish sulfur from the stream. The formation of sulfur from hydrogen sulfide is an essential industrial method to dispose of H_2S. The reaction was shown in Eq. (2).

$$2H_2S \rightleftarrows 2H_{2(g)} + S_{2(g)} \quad (2)$$

Eventually, a high amount of H_2S was converted into solid-state sulfur. However, Mashapa *et al.* [34] indicate the selectivity of the H_2S was highly consider-

able in a mixture. On this basis, the reaction can occur at about 95% single-pass conversion at 700 °C in the presence of molybdenum disulfide (MoS_2) and tungsten disulfide (WS_2) catalysts. Furthermore, the conversion at higher temperatures was correlated with a reaction rate equation, as shown in Eq. (3) [35].

$$r_{H_2} = k_{H_2S,1} c_{H_2S} - k_{H_2S,2} c_{H_2}^2 \quad (3)$$

The equilibrium constant for H_2S decomposition, k_{H2S}, was given in Table 4 and modeled in the simulation reactor R-201.

Reverse water gas-shift reaction (RWGS)

The selection of the catalyst in RWGS is important because carbon monoxide is an active molecule. It may directly react back to CO_2 since RWGS is a typical equilibrium reaction shown in Eq. (4).

$$CO_{2(g)} + H_{2(g)} \rightleftarrows CO_{(g)} + H_2O_{(g)} \quad (4)$$

Wolf *et al.* investigated that the reverse water gas shift reaction (RWGS) occurred in the R-202 via a commercial Ni-Al_2O_3 steam reforming catalyst which was produced with 11% Ni (w/w) and a BET (Brunauer-Emmett-Teller) surface area of 7 m^2g^{-1} [36]. Their work shows the catalyst can catalyze the RWGS reaction effectively, and the conversion of 79% at 900 °C is achieved in a short residence time of less than 100 ms. Experiments at varying temperatures and concentrations of CO_2 and H_2 indicate that the power-law rate shown in Eq. (5) for the RWGS was derived. *c* in which the *f* letter denotes the forward reaction. The conversion of CO_2 to CO with rate $r_{CO2,f}$ was shown in Eq. (5), in which f indicates the forward reaction [36].

$$r_{CO_2,f} = K_{RWGS,f}(T) c_{CO_2} c_{H_2}^{0.3} \quad (5)$$

The equilibrium constant for RWGS reaction, K_{RWGS}, was given in Table 4 and modeled in the simulation reactor R-202.

Fischer-Tropsch Synthesis

Syngas, namely carbon monoxide and hydrogen, flowed out from the RWGS reaction and were treated in the Fischer-Tropsch reactor, namely R-203. Fischer-Tropsch synthesis is the fundamental operation in the process where all carbon monoxide and hydrogen react to form hydrocarbon molecules via FeCuK/Al_2O_3 catalyst [37,38]. The Fischer-Tropsch synthesis that involves the catalytic conversion of synthesis gas into a mixture of hydrocarbons (i.e., paraffins, olefins) is shown in Eqs. (6), (7) [39].

Paraffins: $$nCO + (2n+1) H_2 \rightarrow C_nH_{2n+1} + nH_2 \quad (6)$$

Olefins: $$nCO + 2nH_2 \rightarrow C_nH_{2n} + nH_2O \quad (7)$$

The *n* value stated in Eq. (6) and (7) may be between 1 and 12 (The hydrocarbons produced vary from C1 to C12+) over FeCuK/Al_2O_3 catalyst during F-T synthesis in the simulation. However, the cetane number and the fuel quality decrease as the number of carbon atoms in the hydrocarbon chain increases. Therefore, the production of hydrocarbons with high carbon numbers is undesired.

Kang *et al.* [37] pointed out that the number of carbon atoms in hydrocarbon molecules can be limited with C4 as long as the reactor temperature increases to 600 °C. Thus, the *n* value stated in Eq. (6) and (7) can be altered between 1 and 4 in the simulation model. Wang *et al.* [40] carried out a set of kinetic experiments of Fischer-Tropsch synthesis over industrial Fe-Cu-K catalysts. The simplified forms of reaction rates were given in Eq. (8), (9), and (10), where α is the chain growth factor for the carbon number of *n*, *P* is the partial pressure of a component, and β is the re-adsorption factor of 1-olefin with a carbon number of *n* [40].

$$r_{CH_4} = \frac{K_{FT} P_{H_2} \alpha_1}{1 + \left(\frac{1 \cdot P_{H_2O}}{K_{FT}^3 \cdot P_{H_2}^2} + \frac{1}{K_{FT}^2 \cdot P_{H_2}} + \frac{1}{K_{FT}} \right) \sum_{i=1}^{N} \left(\prod_{j=1}^{j} \alpha_j \right)} \quad (8)$$

$$r_{C_nH_{2n+1}} = \frac{K_{FT} P_{H_2} \prod_{j=1}^{j} \alpha_j}{1 + \left(\frac{1 \cdot P_{H_2O}}{K_{FT}^3 \cdot P_{H_2}^2} + \frac{1}{K_{FT}^2 \cdot P_{H_2}} + \frac{1}{K_{FT}} \right) \sum_{i=1}^{N} \left(\prod_{j=1}^{j} \alpha_j \right)} \quad (9)$$

where n ≥ 2

$$r_{C_nH_{2n}} = \frac{K_{FT} (1-\beta_n) \prod_{j=1}^{j} \alpha_j}{1 + \left(\frac{1 \cdot P_{H_2O}}{K_{FT}^3 \cdot P_{H_2}^2} + \frac{1}{K_{FT}^2 \cdot P_{H_2}} + \frac{1}{K_{FT}} \right) \sum_{i=1}^{N} \left(\prod_{j=1}^{j} \alpha_j \right)} \quad (10)$$

where n ≥ 2.

Eq. (8) is the reaction rate equation of CH_4, in which *n* is 1. In Eqs. (9) and (10), reaction rates of paraffins and olefins were given for *n*-values equal to or greater than 2. The equilibrium constant for Fischer-Tropsch synthesis, K_{FT}, was shown in Table 4 and modeled in the simulation reactor R-203.

RESULTS AND DISCUSSION

Simulation analysis

Capacity distributions of the process are given in Table 5. Hence, 7.3 kg of synthetic fuel, 78 kg of nitrogen gas, and 53 grams of solid-state sulfur were produced, and 21 liters of excess water were separated from every 100 kg of flue gas emitted. The nitrogen stream has approximately 95% purity. The other 5% is oxygen. Besides, the excess water stream had 99.98% purity of H_2O, and the elemental sulfur was separated with 99.9% purity.

The *n* value stated in Eq. (6) and (7) alters between

Table 4. Equilibrium data of chemical reactions [35,36-38]

R-201	$K_{H_2S} = \exp\left[5.677 - 0.072T + 1.108 \cdot 10^{-4}T^2 + \frac{1549.159}{T} - 0.144\ln(T)\right]$	(11)
R-202	$K_{RWGS} = \frac{1}{\exp\left(-0.294Z^3 + 0.635Z^2 + 4.178Z + 0.317\right)}$, with $Z = \frac{1000}{T[K]}$	(12)
R-203	$K_{WGS} = \frac{5078.005}{T} + 5.897 - 13.959 \cdot 10^{-4}T - 27.593 \cdot 10^{-8}T^2$	(13)

1 and 4 in the simulation model. Hence, the produced fuel mixture at the end of R-203 includes methane, ethane, propane, propylene, butane, and butene. Conversion rates of hydrocarbons are shown in Table 6.

Table 5. Flow rates of mainstreams

Components	Mass Flow Rate (kg/s)
Synthetic Fuel	4.05
Rich-Nitrogen	44.0
Excess Water	11.9
Elemental Sulfur	0.03
Inlet Flue Gas	56.46
Hydrogen Gas Feed	5.0

Table 6. Selectivity distribution over $FeCuK/Al_2O_3$ catalyst

Catalyst	$FeCuK/Al_2O_3$
Temperature (°C)	600
CO conversion (%)	98.4
Selectivity (C-mol %)	
CO_2	12.0
Hydrocarbons	88.0
Hydrocarbon selectivity (%)	
C_1	29.3
C_2	15.5
C_3	23.8
$C_{3=}$	0.10
C_4	16.9
$C_{4=}$	2.40

Natural gas has a great gross heating value compared with other fossil fuels, and it is a widespread fuel type regarding its great amount of light hydrocarbon content [41]. Light hydrocarbons release more energy because they contain more hydrogen atoms than heavier hydrocarbons. Also, natural gas is a non-toxic fuel type since it contains sulfur in small quantities. Since the synthetic fuel produced during this study is an alternative energy source to fossil fuels, the compositional benchmark of synthetic fuel and natural gas is shown in Table 7. Desulfurized energy utilization is important for the environment. The produced synthetic fuel does not contain any sulfur composition, whereas a typical natural gas may contain hydrogen sulfide. However, synthetic fuel contains relatively low methane compounds, which lowers the calorific value compared to natural gas.

Table 7. Compositional benchmark of synthetic fuel and natural gas

Symbol	Compound	Compositions (%)	
		This study	Natural Gas [13]
CH_4	Methane	32.9	70-98
C_2H_6	Ethane	16.5	1-10
C_3H_8	Propane	24.7	0-5
C_3H_6	Propylene	0.99	-
C_4H_{10}	Butane	17.4	0-2
C_4H_8	Butene	2.37	-
CO_2	Carbon dioxide	3.81	0-1
O_2	Oxygen	1.07	0-0.2
N_2	Nitrogen	0.36	0-15
H_2S	Hydrogen sulfide	-	Trace occasionally
H_2O, H_2, He	Rare gases	0.01	Trace occasionally

Fuel quality is another key point to concentrate on. The calorific value is an essential characteristic used to evaluate fuel quality. The calorific value of a fuel can be measured using the bomb calorimetry and the standard methods such as ASTM-D201. In addition, some estimation equations were suggested to determine the heating value based on the elemental compositions of hydrocarbons [43]. As a result of the evaluation, gross and net calorific values of the produced synthetic fuel and comparison with other common fuel types are illustrated in Fig. 5 [13–42]. The gross calorific value of a fuel is equal to the net calorific value with the addition of the heat of vaporization of the water content in the fuel. The synthetic fuel produced was found to be a fuel

type, an immensely qualified fuel, compared with other types of fossil fuels.

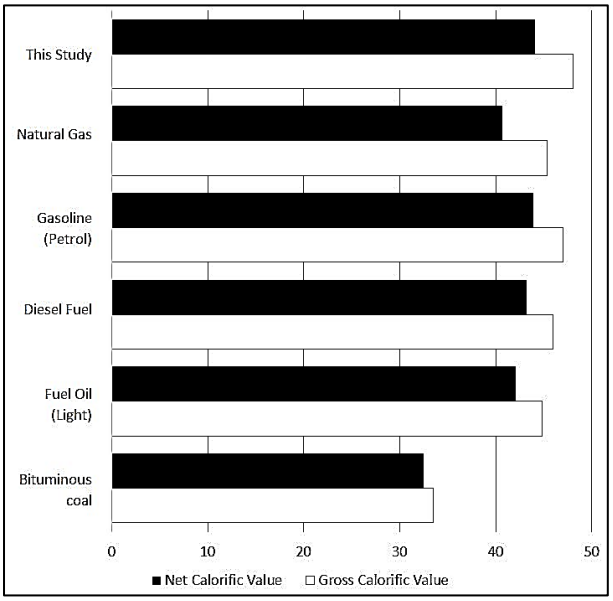

Figure 5. Calorific values of various fuels (MJ/kg) [13, 42].

Economic analysis

A preliminary economic analysis was calculated based on the engineering economic analysis of Turton *et al.* [44]. The detailed equipment purchased and production costs were calculated by assuming Chemical Engineering Plant Cost Index (CEPCI) as 500. Land cost and working capital were assumed as 1% and 15% of the fixed capital investment, respectively [45]. The cost of nitrogen gas was taken as $0.08/kg [46], and the price of synthetic fuel was assumed to be the same as the price of natural gas. The capital cost of each piece of equipment was calculated as $63,790,535, and it was used to determine the fixed capital investment, FCI, of the project. FCI refers to an entirely new facility in which the construction was started on an essentially undeveloped area, a grass field. Besides, working capital is required to start up the plant and finance the first few months of operation. The total operating cost of the process is shown in Table 8. The cost of manufacturing is the sum of costs of all resources consumed in making products, and the result of COM is $95,980,622. There are four categories to achieve theoretical manufacturing cost, COM. These were shown in Eq. (14).

$$COM = 0.18FCI + 2.73C_{OL} + 1.23(C_{UT} + C_{WT} + C_{RM}) \quad (14)$$

Table 8. Total operating cost

	Expenses	Percentage %	Calculated Values ($M)
CTM	Equipment Costs		63.3
	Coolers	2.09 of FCI_L	1.64
	Heaters	2.47 of FCI_L	1.94
	Compressors	48.1 of FCI_L	37.7
	Reactors	2.88 of FCI_L	2.26
	Furnaces	26.0 of FCI_L	19.7
WC	Working Capital	15.0 of FCI_L	11.8
L	Land Cost	1.00 of FCI_L	0.79
FCI	Fixed Capital Investment		78.5
C_{OL}	Operating Labor	1.43 of COM_d	1.42
C_{UT}	Utility Costs		18.1
	Coolers	0.64 of COM_d	0.61
	Heaters	1.33 of COM_d	1.27
	Compressors	0.03 of COM_d	0.03
	Furnaces	16.8 of COM_d	16.1
C_{RM}	Raw Materials		45.2
	Flue Gas	-	-
	Hydrogen	47.2 of COM_d	45.2
COM	Total Manufacturing Cost		95.8

The first category is the cost of operating labor, C_{OL}, calculated from the amount of equipment in the plant. Hence, 15 operating laborers were determined, and C_{OL} is $1,134,137. Then, the second category is the utility expenses, C_{UT}. Those utilities are low-pressure steam, nitrogen refrigerator, natural gas, and electric power consumed throughout the process. The third category is the cost of raw materials (C_{RM}). Since the purchase price of flue gas was assumed to be zero, only hydrogen was included in raw material expenses. Finally, C_{WT} stands for the cost of waste treatments. However, there is no waste material in the stream. The purge stream was composed of hydrogen-rich gases. Therefore, it can be incinerated or used as process fuel.

There are three bases used for the profitability analysis of plant design. These are time, cash, and interest rate criteria. Considering Europe's average corporate income tax rate (22.5 percent) [47], which is slightly higher than the global average (21.4 percent) and a discount rate (10 percent), the time and interest rate criteria were only considered in this study. The term used for the time criterion is the payback period (PBP). It is the time required to recover the capital investment. The project's PBP and discounted payback period (DPBP) were calculated as 6.1 and 7.5 years, respectively. The rate of return on investment (ROROI) was also used as an interest rate criterion in this economic estimation, and it was calculated as 16.64%.

Sustainable development goals

The Sustainable Development Goals (SDGs) or Global Goals are a collection of 17 interlinked goals designed to be a "blueprint for achieving a better and more sustainable future for all" by the United Nations Development Programme (UNDP) [48]. The excess water can be sold to industrial production facilities to avoid using natural water sources. Thus, clean water and sanitation (goal 6) can be provided. Also, synthetic fuel was produced, an affordable and clean energy source (goal 7, aimed to be achieved by 2030 by UNDP). Supporting sustainable industries and investing in R&D are significant ways to provide sustainable growth; thus, goal 9 (industry, innovation, and infrastructure) was also fulfilled. The study's objective is to protect natural resources related to goal 12 (responsible consumption and production). Since CO_2 emission serves climate change, climate action (goal 13) was provided. Finally, ocean acidification will be reduced by reducing CO_2 emissions. Hence, the aquatic living beings will be protected.

CONCLUSION

Fossil energies (FE) will remain the mainstay of global energy consumption for the future based on their current superiority [49]. 41% of all anthropogenic CO_2 emissions will derive from industrial power plants by 2035. Environmental problems caused by GHG emissions are directly associated with nonrenewable energy production and utilization. Hence, studying potential energy systems is fundamental for preventing future climate change caused by humankind. For instance, carbon pricing is one of the most effective ways to reduce emissions, which manages GHG emissions by placing a fee on emitting and offering an incentive for emitting less by 2025. This action shifts in consumption and investment patterns, making economic development compatible with climate protection [50].

Substituting FEs with renewable energy has an essential role in developing a sustainable and carbon-free economy. Thus, this study aims to develop an alternative sustainable flue gas-to-fuel recycle system to cut down the dependence on FEs. Fischer-Tropsch synthesis is used to produce the hydrocarbon mixture from syngas. Since CO_2 has a negative impact on the Fischer-Tropsch process due to reducing the selectivity of hydrocarbons with carbon numbers above 5 [51], the excess CO_2 gas is distinguished after the reverse water gas shift reaction and before the Fischer-Tropsch synthesis. $FeCuK/Al_2O_3$ catalyst is 600 °C for the Fischer-Tropsch synthesis in R-203 to produce hydrocarbons whose carbon number is up to 4. $FeCuK/ Al_2O_3$ catalyst also provided a high CO conversion rate (98.4%) and high hydrocarbon selectivity (88%). The produced synthetic fuel has a gross calorific value of 48 MJ/kg, which is effective compared with other FEs. About 6.59% of the input components are converted into synthetic fuel, while other parts are distinguished as 90.3% pure nitrogen gas (71.6%), excess industrial water (19.4%), and elemental sulfur (0.05%). The remained part (about 2.4%) of the input streams is disposed of as the purge stream (Fig. 3).

Equipment and utility costs are calculated regarding the types and properties of equipment operating in the simulation. The raw material H_2 occupies a major part of the cost of manufacturing. Thus, this process may be combined with H_2 production technologies. The electrochemical methods for H_2 production, such as electrolysis or photoelectrochemical, may be adapted to convert excess water distinguished from the system to H_2. Although these technologies may be the cleanest ones, they cost around 80% of the operating cost and are highly expensive. Besides, photosynthetic processes (including algae) which use CO_2 and H_2O for H_2 production are also sustainable technologies [52].

The payback period is calculated as 6.1 years, while discounted payback period is about 7.5 years, concerning the discount rate of 10%. Therefore, ROROI is also measured as 16.64%, which can be considered a good ROROI for an investment [53].

REFERENCES

[1] UN Environmental Programme, UN Environment Annual Report 2019, https://www.unep.org/annualreport/2019/index.php [accessed 16 September 2020].

[2] National Oceanic and Atmospheric Administration, Ocean acidification, https://www.noaa.gov/education/resource-collections/ocean-coasts/ocean-acidification [accessed 16 September 2020].

[3] F. Stocker, K. Qin, M. Plattner, K. Tignor, J. Allen, A. Boschung, V. Xia, Climate Change: The Physical Science Basis, in Intergovernmental Panel on Climate Change, Geneva, Switzerland (2013), p. 190–196.

[4] Global Climate Change – Facts (FAQ). NASA - Climate Change: Vital Signs of the Planet. Retrieved February 20, 2021, from https://climate.nasa.gov/faq/.

[5] Minnesota Pollution Control Agency, Chlorofluorocarbons (CFCs) and hydrofluorocarbons (HFCs), https://www.pca.state.mn.us/air/ chlorofluorocarbons-cfcs-and-hydrofluorocarbons-hfcs [accessed 20 November 2020].

[6] T. Gunduz, Environmental Chemistry, Gazi Publishers, Ankara (2012), p. 90–170.

[7] R. Kolieb, D. Herr, Clim. Policy, 12 (2011) 378–389.

[8] B. Bereiter, S. Eggleston, J. Schmitt, C. Ahles, F. Stocker, H. Fischer, S. Kipfstuhl, J. Chapellaz, Geophys. Res. Lett. 42 (2015) 542–549.

[9] M. Ozturk, I. Dincer, Nat. Gas Sci. Eng. 83 (2020) p. 103–111.

[10] International Energy Agency Statistics, CO2 emissions statistics, https://www.iea.org/data-and-statistics/data-product/co2-emissions-from-fuel-combustion-highlights#overview [accessed 16 July 2021].

[11] United Nations Environment Programme, Lagging in climate action, G20 nations have huge opportunities to increase ambition, https://www.unep.org/news-and-stories/press-release/lagging-climate-action-g20-nations-have-huge-oportunities-increase [accessed 17 April 2021].

[12] J. Olivier, W. Peters, Trends in Global CO2 and Total Greenhouse Gas Emissions, https://www.pbl.nl/sites/default/files/downloads/pbl-2020-trends-in-global-co2-and-total-greenhouse-gas-emissions-2019-report_4068.pdf [accessed 18 April 2020].

[13] G. Speight, Natural Gas: A Basic Handbook, Gulf Professional Publishing, London (2019), p. 59–98.

[14] E. Koohestanian, F. Shahraki. J. Environ. Chem. Eng. 9(4) (2021), 105–125.

[15] M. A. Nemitallah, M. A. Habib, H. M. Badr, S. A. Said, A. Jamal, R. Ben-Mansour, E. M. A. Mokheimer, K. Mezghani. Int. J. Energy Res. 41(12) (2017), 1670–1708.

[16] X. Liang, Q. Wang, Z. Luo, H. Zhang, K. Li, Y. Feng, R. Shaikh, J. Cen, RSC Adv. 8 (2018) 35690–35699.

[17] S. Abuelgasim, W. Wang, A. Abdalazeez, Sci. Total Environ. 764 (2021) 142–892.

[18] M. Osman, N. Khan, A. Zaabout, S. Cloete, S. Amini. Fuel Process. Technol. 214 (2021) 106–684.

[19] A. K. Vuppaladadiyam, J. G. Yao, N. Florin, A. George, X. Wang, L. Labeeuw, Y. Jiang, R. W. Davis, A. Abbas, P. Ralph, P. S. Fennell, M. Zhao. ChemSusChem. 11(2) (2018), 334–355.

[20] R. Kothari, S. Ahmad, V. V. Pathak, A. Pandey, A. Kumar, R. Shankarayan, P. N. Black, V. V. Tyagi. Biomass Convers. Biorefin. 11(4) (2019) 1419–1442.

[21] E. Koohestanian, J. Sadeghi, D. Mohebbi-Kalhori, F. Shahraki, A. Samimi. Energy, 144 (2018) 279–285.

[22] P. Ortega, Analyzes of Solar Chimney Design, Trondheim, Norway (2011), p. 78.

[23] A. Simonovic, N. Stupar, P. Pekovic, FFME Trans. 36 (2008) 119–125.

[24] R. Arachchige, C. Melaaen, Energy Procedia. 23 (2012) 391–399.

[25] Process Instrumentation Consultancy & Design, & Edwards, J. E. Process Modelling Selection of Thermodynamic Methods. Chemstations. (2018) https://www.chemstations.com/content/documents/Technical_Articles/thermo.pdf.

[26] D. Aaron, C. Tsouris, Sep Sci Technol. 40 (2005) 321–348.

[27] J. Mustafa, M. Farhan, M. Hussain, J. Membr. Sci. 6 (2016) 221–238.

[28] F. Russo, F. Galiano, A. Iulianelli, A. Basile, A. Figoli, Fuel Process. Technol. 213 (2021) 106–643.

[29] I. Song, H. Ahn, H. Jeon, K. Jeong, Y. Lee, H. Choi, H. Kim, B. Lee, Desalination, 234 (2008) 307–315.

[30] G. Towler, R. Sinnott, Chemical Engineering Design: Principles, Practice and Economics of Plant and Process Design, Elseiver, Amsterdam (2012) p. 811–816.

[31] D. Kundnaney, K. Kushwaha, 2015, A Critical Review on Heat Exchangers used in Oil Refinery, in 3rd Afro-Asian International Conference on Science, Engineering and Technology, Bharuch, India (2015), p. 1–5.

[32] M. Rhine, S. Truelove, HEDH Multimedia-Heat Exchanger Design Handbook, Begell House Inc. Connecticut (2014) p. 24.

[33] International Organization for Standardization, Petroleum Product-Determination of sulfur content of automotive fuels–Ultraviolet fluorescence method (ISO 20846:2019), https://www.iso.org/standard/74313.html [accessed 17 April 2020].

[34] N. Mashapa, D. Rademan, J. Vuuren, Ind. Eng. Chem. Res. 46 (2007) 6338–6344.

[35] J. Zaman, A. Chakma, Fuel Process. Technol. 41 (1995) 159–198.

[36] A. Wolf, A. Jess, C. Kern, Chem. Eng. Technol. 39 (2016) 1040–1048.

[37] H. Kang, W. Bae, Y. Cheon, J. Lee, S. Ha, W. Jun, H. Lee, W. Kim, Appl. Catal. B. 103 (2011) 169–180.

[38] J. Chang, L. Bai, T. Teng, L. Zhang, J. Yang, Y. Xu, W. Xiang, W. Li, Chem. Eng. Sci. 62 (2007) 4983–4991.

[39] A. Delparish, A. K. Avci. Fuel Process. Technol. 151 (2016) 72–100.

[40] Y. N. Wang, W. P. Ma, Y. J. Lu, J. Yang, Y. Xu, H. W. Xiang, Y. Li, Y. L. Zhao, B. J. Zhang. Fuel, 82 (2021) 195–213.

[41] H. Brauers, I. Braunger, J. Jewell, Energy Res. Soc. 76 (2021) 102–120.

[42] J. Carvill, Mechanical Engineers Data Handbook, M. Kutz Ed., Elseiver, Amsterdam (2005), 102–145.

[43] S. Hosokai, K. Matsuoka, K. Kuramoto, Y. Suzuki, Fuel. Process. Technol. 152 (2016) 399–405.

[44] R. Turton, J. Shaeiwitz, D. Bhattacharyya, W. Whiting, Analysis, Synthesis, and Design of Chemical Processes (International Series in the Physical and Chemical

Engineering Sciences), Pearson, London (2018), 156–213.
[45] R. Woods, Rules of Thumb in Engineering Practice, Wiley, New York (2007).
[46] J. Kim, Y. Seo, D. Chang, Apl. Energy. 182 (2016) 154–163.
[47] E. Asen, Corporate Income Tax Rates in Europe, https://taxfoundation.org/2020-corporate-tax-rates-in-europe [accessed 16 April 2020].
[48] United Nations Development Programme, Sustainable Development Goals, https://sdgs.un.org/goals [accessed 16 September 2020].
[49] M. Höök, X. Tang. Depletion of fossil fuels and anthropogenic climate change–A review. Energy Policy, 52 (2013) 797–809.
[50] United Nations Framework Convention on Climate Change. About Carbon Pricing, https://unfccc.int/about-us/regional-collaboration-centres/the-ci-aca-initiative/about-carbon-pricing#eq-1 [accessed 8 February 2022].
[51] W. C. Wang, Y. C. Liu, R. A. A. Nugroho, R. A. A. Energy, 239 (2022) 121970.
[52] R. Chaubey, S. Sahu, O. James, S. Maity. Renew. Sust. Energy. Rev. 23 (2013) 443–462.
[53] Birken, E. G. Understanding Return on Investment (ROI). Forbes Advisor, https://www.forbes.com/advisor/investing/roi-return-on-investment/ [accessed 9 February 2022].

H. BATUHAN OZTEMEL
INCI SALT
YAVUZ SALT

Department of Chemical Engineering, Faculty of Chemical and Metallurgical, Yildiz Technical University, Istanbul, Turkey

NAUČNI RAD

KORIŠĆENJE UGLJEN-DIOKSIDA: SIMULACIJA PROCESA PROIZVODNJE SINTETIČKOG GORIVA IZ DIMNIH GASOVA

Problemi životne sredine su u porastu i danas više povezani sa klimom, prvenstveno uzrokovani emisijom gasova sa efektom staklene bašte. Takođe, industrijske emisije širom sveta iz elektrana će prouzrokovati 50% koncentracije ugljen-dioksida u atmosferi do 2035. godine. Za simulaciju proizvodnje sintetičkog goriva iz dimnih gasova koje emituju industrijske elektrane korišćen je softver ChemCAD. Ona je imala za cilj da sve sastojke dimnih gasova konvertuje u vredne proizvode kako bi se smanjio uticaj štetnih gasova na životnu sredinu. Proizvedeno sintetičko gorivo sastoji se od 94,75% ugljovodonika sa brojem ugljenika do četiri sa ukupnom stepenom konverzije od 6,59%. Oko 95% sumpora u dimnom gasu se izdvaja odsumporavanjem smeše goriva. Membranski process, takođe, izdvaja 90,3% azota iz dimnog gasa. Sumporizacijom, povratnom reakcijom vod-gas i Fišer-Tropšovom sintezom u prisustvu sa odgovarajućih katalizatora postižu se stepeni konverzije od 95%, 79% i 98,4% u jednom prolazu, reodm. Urađena je i ekonomska analiza, a period otplate projekta je 6,1 godina, dok je zarada na investirano 16,64%.

Ključne reči: ugljen-dioksid, Fišer-Tropšova sinteza, dimni gas, simulacija procesa, sintetičko gorivo.

CI&CEQ
Chemical Industry & Chemical Engineering Quarterly

Available online at
Association of the Chemical Engineers of Serbia AChE
www.ache.org.rs/CICEQ

Chem. Ind. Chem. Eng. Q. 28 (4) 319–327 (2022) CI&CEQ

SHUAI ZOU[1,3]
KANGCHUN LI[2,3]
MINGYUAN DOU[1,3]
JING YANG[1,3]
QING FENG[1,3]
FUCHUAN HUANG[1,3]
LIN CHEN[1]

[1]School of Mechanical Engineering, Guangxi University, Nanning, Guangxi, China

[2]School of Chemistry & Chemical Engineering of Guangxi University, Nanning, Guangxi, China

[3]Guangxi Key Laboratory of Petrochemical Resource Processing and Process Intensification Technology, Guangxi University

SCIENTIFIC PAPER

UDC 662.767.2:004

EXERGY ANALYSIS OF THE BIOGAS MULTISTAGE COMPRESSION PROCESS BASED ON ASPEN PLUS SIMULATION

Article Highlights

- It simulated and analyzed the exergy changes of the biogas multistage compression process by Aspen Plus
- The interstage cooling temperature affects the energy consumption of the whole compression process
- The exergy efficiency increased with the increase in the number of compression stages

Abstract

In this study, by taking the compression separation process of a biogas project as a research subject, a multistage compression process was simulated using Aspen Plus software. The exergy analysis of the biogas project under multistage compression and adiabatic or isothermal conditions was performed employing the thermodynamic principle. The results showed that the biogas exergy increased with pressure during the compression process and correspondently decreased in the interstage cooling process. Further, the compression series increased with the increase in efficiency, but the increase was gradual. The results of the example study of the four-stage compression process are as follows: the process exergy increased by ~83.07 kW, the process exergy efficiency was ~75.56%, and the recovery exergy potential was ~12.6 kW. In this study, the allocation of compression ratios and the selection of compression stages within the multistage compression process were analyzed by Aspen Plus was used to analyze., This analysis can ultimately help others design efficient multistage compression systems that reduce energy losses.

Keywords: Aspen Plus, biogas, exergy analysis, multistage compression.

As a part of clean energy, biogas is inexhaustible renewable energy. Biogas projects can solve the daily energy problems in rural areas, effectively deal with all kinds of organic waste, and produce efficient and harmless organic fertilizers [1]. Moreover, they play an active role in environmental protection, ecological improvements, energy security, etc. Thus, the Chinese government has significantly supported the biogas industry [2]. By the end of 2018, 108,059 biogas projects had been completed, more than 7,900 being large-scale biogas projects [3]. Moreover, under carbon neutrality, the supply of biomass gas energy has significantly increased [4]. As a form of high-quality renewable biomass energy, biogas is mainly composed of CH_4 (60%-70%) and CO_2 (28%-40%), and the remaining components are H_2S, N_2, NH_3, etc. [5,6]. Despite the efficiency of using biogas, the considerable amount of CO_2 in biogas decreases its calorific value and energy density and leads to the corrosion of its transportation pipelines. Therefore, biogas must be purified to remove CO_2 and other impurities and improve its use value [7]. Generally speaking, the sepa-

Correspondence: F. Huang, L. Chen, School of Mechanical Engineering, Guangxi University, Nanning, 533004, Guangxi, China.
E-mail: huangfuchuan@gxu.edu.cn; gxdxcl@163.com
Paper received: 22 August, 2021
Paper revised: 13 April, 2022
Paper accepted: 21 April, 2022

https://doi.org/10.2298/CICEQ210822006Z

ration methods of CO_2 are the absorption method [8], membrane separation method [9,10], pressure swing adsorption method [11], and cryogenic separation method [12]. Cryogenic separation is a common method for CO_2 capture and separation. The principle is to use the liquefaction characteristics of CO_2 at 31 °C and 7.39 MPa or -59–30 °C and 0.47–7.22 MPa. The multistage compression and cooling of biogas make CO_2 liquefied, thus realizing the separation of CO_2 and CH_4. The technological process is as follows: dedusting, desulphurization, drying, multistage compression, CO_2 liquefaction separation, and storage. Biogas is treated by dedusting, desulphurization, and dehydration to prevent the impurities in the gas from corroding and damaging the compression equipment, pipes, and accessories [13]. The purified biogas enters multistage compression equipment when the temperature is lower than 31 °C. Then, the compressed biogas is cooled and liquefied by a condenser, and the CO_2 in the biogas is separated. The cryogenic separation method produces high-purity biological methane, and the separated high-purity liquid CO_2 can be used in other fields [14].

Xu *et al*. [15] proposed a new integrated method for CO_2 compression separation. Their research showed that the higher the initial pressure and initial CO_2 concentration in the mixture, the better the refrigeration cycle performance and the lower the energy consumption of the new integrated method. Using Aspen Hysys, Zhou *et al*. [16] simulated the low-temperature liquefaction process separating CO_2 gas from biogas. By changing the volume fractions of CH_4 and CO_2, the dew point and separation pressure ranges of biogas were obtained. At the same time, through experimental verification and simulation, a method for the industrial separation of CO_2 and purification of biogas was obtained. Li *et al*. [12] simulated a low-temperature biogas purification process using the Aspen Plus software. They analyzed the influences of pressure and temperature on the effect of the low-temperature purification process. Ahmed *et al*. [17] proposed an improved cryogenic separation for CO_2/CH_4 gas mixtures, and it could significantly reduce methane losses, energy consumption, and investment costs while ensuring the purity of methane and CO_2. These researches studied the whole process, but there is still no research on the compression step in the biogas purification process. Since the energy consumption in the compression process accounts for a large proportion of the total energy consumption, effectively improving the efficiency of the compression process is of great significance for reducing the energy consumption of the compression device. The efficiency of the isothermal and adiabatic compression process can be estimated using thermodynamic principles. The efficiency of the actual compression process is usually between isothermal and adiabatic compression. Aspen Plus [18] is a process simulation software integrating chemical engineering designs, dynamic simulations, and other calculations. It comprises a physical property database, a unit operation module, and a system implementation strategy. Generally, it can simulate various operation processes and single operation units. This study is based on an Aspen Plus simulation. The energy-saving potential of biogas' multistage compression separation process was analyzed using the exergy analysis method. A p-V diagram visually demonstrated the difference between the ideal isothermal and adiabatic compression. In addition, the effect of the number of compression stages on energy consumption was quantitatively revealed. Moreover, based on simulation data, the exergy change of biogas was analyzed, and its exergy recovery potential was discussed.

Exergy analysis of the biogas compression process

Simulation model of the polytropic compression process

Regarding the polytropic centrifugal compression process of biogas, Aspen Plus provides two thermodynamic calculation methods: the GPSA and ASME methods [19]. The ASME algorithm is aimed at real gas, so the condition of the ASME algorithm is more stringent than that of the GPSA algorithm. For a real gas, the polytropic coefficient (n) value of the polytropic compression process is uncertain, so a correction factor is introduced into the isentropic compression equation.

The calculation formula of the enthalpy change is as follows:

$$\Delta H = \frac{HEAD}{\eta_p} \tag{1}$$

$$HEAD = f\frac{np_1V_1}{n-1}\left[\left(\frac{p_2}{p_1}\right)^{\frac{n-1}{n}} - 1\right] \tag{2}$$

$$\eta_p\left(\frac{n-1}{n}\right) = \frac{k-1}{k} \tag{3}$$

$$f = \frac{n-1}{n}\frac{H_2 - H_1}{p_2V_2 - p_1V_1} \tag{4}$$

$$n = \ln\left(\frac{p_2}{p_1}\right) / \ln\left(\frac{V_1}{V_2}\right) \tag{5}$$

where ΔH is the molar enthalpy change, $HEAD$ is the polytropic energy head, η_p is the polytropic efficiency, n is the polytropic coefficient, k is the specific heat capacity ratio of gas, f is the correction factor of the polytropic energy head, H_1 and H_2 are enthalpies of the initial and final states of the compression process, respectively, P_1 and P_2 are the gas pressures in the

initial and final states respectively, and V_1 and V_2 are the molar volume flow rates of the initial and final states, respectively.

Exergy analysis of the compression process

According to the first and second laws of thermodynamics [20], energy is conserved during energy conversion and transmission, and the energy level decreases. Exergy (E_x) is the energy that can theoretically be converted into work to the maximum extent under certain conditions. When the system changes from any state (P, T) to the benchmark state (P_0, T_0) :

$$E_x = H - H_0 - T_0(S - S_0) \tag{6}$$

where H and S are the enthalpy and entropy of the fluid in a specific state, respectively, H_0 and S_0 are the enthalpy and entropy of the fluid in the reference state, and T_0 is the benchmark state temperature.

The enthalpy of the gas compression process is changed into:

$$dH = C_p dT + \left[V - T\left(\frac{\partial V}{\partial T}\right)_p\right] dp \tag{7}$$

The process entropy is changed into:

$$dS = C_p \frac{dT}{T} - \left(\frac{\partial V}{\partial T}\right)_p dp \tag{8}$$

It should be noted that:

$$S = C_p \ln T - R_g \ln p + C \tag{9}$$

When the initial state is isothermal in the final state, the gas entropy is changed into:

$$\Delta S = S_2 - S_1 = \Delta C_p \ln T + R_g \ln\left(\frac{p_1}{p_2}\right) \tag{10}$$

where C is the integral constant, and ΔC_p is the difference between the specific heat capacities of the final and initial states at constant pressure. When the gas is compressed and cooled, the initial and final states are isothermal, where $\Delta S<0$ is the entropy reduction, the compressed gas works to the environment, and R_g is the gas constant.

According to the second law of thermodynamics, the exergy difference between the compressed gas in the initial and final states is taken as a target, and the exergy efficiency (η_x) is used to evaluate the effectiveness of the energy process. That is,

$$\eta_x = \frac{\Delta E_x}{W} = \frac{H_2 - H_1 - T_0(S_2 - S_1)}{W} \tag{11}$$

where W is the compression power of the multistage compressor.

Analysis of the biogas multistage compression process

Multistage compression process simulation

Taking the biogas project that the raw biogas is passed already through the pre-conditioning step with some non-major elements (traces) of nitrogen (N_2), water (H_2O), hydrogen sulfide (H_2S), and volatile organic gases (VOCs) have been removed. Therefore, a typical composition of 60% (mol) CH_4 and 40% (mol) CO_2 for the raw biogas fed to the proposed process is adopted in this work.

The four-stage compression separation process of purified biogas was chosen as a research subject, and the process diagram is shown in Fig. 1. First, the biogas is compressed to 525 kPa by the first-stage compressor and cooled to 25 °C by the first-stage intercooler. Then, it enters the second-stage compressor to be compressed to 1105 kPa, and the compressed biogas enters the second-stage intercooler to cool down to 25 °C. Then, the biogas is compressed in the third-stage compressor to 2320 kPa, and the compressed biogas is cooled to 25 °C by the third-stage intercooler. Finally, the biogas is compressed and pressurized to 4908 kPa by the fourth-stage compressor. After the compression, the biogas enters the fourth-stage intercooler and is cooled to 25 °C. The main characteristics of the principal streams numbered in the process (from S1 to S12, as shown in Fig. 1) are listed in Table 1 in terms of flow rate, pressure, temperature, vapor fraction, and composition.

The compression process was simulated and analyzed using the Pressure Changers/Compr module and the Heat Exchangers/Heater module in Aspen Plus. The analysis of the simulation results of the actual centrifugal multistage compression process shows that the ASME polytropic model is more rigorous than the GPSA polytropic model and can be closer to the actual working conditions [18]. Therefore, the compressor model should choose the ASME polytropic model in the actual engineering simulation. After purification, biogas mainly contains CH_4 and CO_2, both of which are composed of nonpolar molecules. For this case, the PR-BM physical property method is usually selected, suitable for nonpolar or weak polarity systems under all temperatures and pressures, and its simulation results are more accurate [21]. Table 2 shows the Aspen Plus simulation parameters of the biogas compression process.

RESULTS AND DISCUSSION

Table 3 shows the Aspen Plus simulation results of the four-stage compression process. Also, Table 4

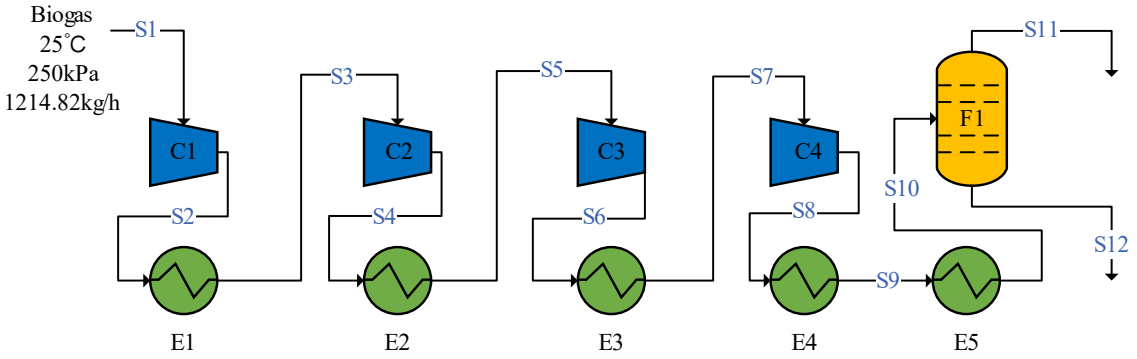

Figure 1. Four-stage compression process diagram.

Table 1. Streams characteristics of the compression process

Stream no.	Composition (% mole base)		Vapor fraction	Temperature (K)	Pressure (MPa)	Molar flow (kmol/h)
	CH_4	CO_2				
S1	60.00	40.00	1	298.15	0.25	44.615
S2	60.00	40.00	1	361.87	0.525	44.615
S3	60.00	40.00	1	298.15	0.525	44.615
S4	60.00	40.00	1	362.51	1.105	44.615
S5	60.00	40.00	1	298.15	1.105	44.615
S6	60.00	40.00	1	363.13	2.32	44.615
S7	60.00	40.00	1	298.15	2.32	44.615
S8	60.00	40.00	1	365.29	4.908	44.615
S9	60.00	40.00	1	298.15	4.908	44.615
S10	60.00	40.00	0.776	233.15	4.908	44.615
S11	5.51	94.49	0	190.86	3.750	26.795
S12	91.86	8.14	1	265.01	4.906	17.820

Table 2. Simulation parameters of the biogas compression

Items	Data
Polytropic Compression efficiency	0.85
Quantity of flow/ $kg \cdot h^{-1}$	1214.82
Temperature / C	25
Pressure / kPa	250

compares the volume flow rates of the ideal isothermal and polytropic compression of biogas under different pressures. Fig. 2 shows the p-V relationship when biogas is compressed to 4.908 MPa under different compression conditions.

As shown in Fig. 2, the actual compression process of biogas after the four-stage compression process is close to ideal isothermal compression, and its efficiency is higher than that of the one-stage compression. According to the work calculation formula $W = pV$, the area enclosed by the multistage compression curve and first-stage compression curve in Fig. 2 is the work saved by the multistage compression of the compressor compared with the first-stage adiabatic compression. Under the premise of choosing a reasonable compression ratio, the more the stages of the compressor, the larger the enclosed area. That is, energy-saving increases with the increase in saved work. However, in actual projects, investment accordingly increases. Therefore, we need to make comprehensive considerations need to be made before making choices.

Table 3. Simulation results of the four-stage compression

Compression Stage	Quantity of Flow / kg·h^{-1}	Outlet Pressure / kPa	Inlet Temperature / ℃	Outlet Temperature / ℃	Interstage Compression Power / kW	Interstage Cooling Load / kW
1	1214.85	525	25	88.72	29.38	-30.25
2	1214.85	1105	25	89.36	29.23	-31.09
3	1214.85	2320	25	89.98	28.63	-32.62
4	1214.85	4908	25	92.14	27.93	-36.88

Table 4. Comparison of volume flow rates between ideal isothermal compression and polytropic compression of biogas under different pressures

Pressure / kPa	Ideal isothermal compressed volume flow rate (25 ℃) / (m^3/h)	Polytropic compression	
		Temperature / ℃	Volume flow rate / (m^3/h)
250	438.93	25	438.93
525	209.01	88.72	253.59
1105	99.31	159.81	144.26
2320	47.30	237.25	81.25
4908	22.36	321.84	45.15

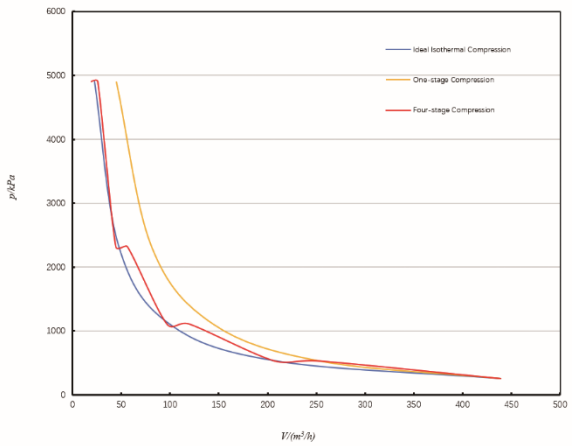

Figure 2. Analysis of energy-saving potential in biogas four-stage compression process.

Analysis of the main factors influencing the energy consumption of the compressors

The compression ratio is one of the most important parameters affecting energy consumption in multistage compression processes [22]. Therefore, four operating conditions were set up to discuss the compression ratio influence. Operating condition 1: the average distribution of the compression ratio in the multistage compression process, i.e., ε_1 = 2.105. Operating condition 2: the compression ratio of the multistage compression process gradually decreases, i.e., $\varepsilon_{2\text{-}1}$ = 2.5, $\varepsilon_{2\text{-}2}$ = 2.112, $\varepsilon_{2\text{-}3}$ = 2, $\varepsilon_{2\text{-}4}$ = 1.859. Operating condition 3: the compression ratio gradually increases in the multistage compression process, i.e., $\varepsilon_{3\text{-}1}$ = 1.859, $\varepsilon_{3\text{-}2}$ = 2, $\varepsilon_{3\text{-}3}$ = 2.112, $\varepsilon_{3\text{-}4}$ = 2.5. Working condition 4: the compression ratios of the first and fourth stages in the multistage compression process are slightly lower than those of the middle stages, i.e., $\varepsilon_{4\text{-}1}$ = 2, $\varepsilon_{4\text{-}2}$ = 2.216, $\varepsilon_{4\text{-}3}$ = 2.215, $\varepsilon_{4\text{-}4}$ = 2. The Pressure Changers/Compr and Heat Exchangers/Heater modules in Aspen Plus were used to simulate the compression process of biogas under four operating conditions, respectively, and the simulation results are shown in Table 5 and Fig. 3.

It can be seen from Table 5 and Fig. 3 that under operating condition 1, the compressor power and heat exchanger load in the multistage compression process are the lowest: 115.170 kW and 130.842 kW, respectively. The simulation results are also consistent with the theoretical optimal compression ratio of multistage compression [23].

The number of compression stages is also one of the important parameters that affect the energy consumption of the multistage compression process. When gas is compressed to a certain pressure, the more the compression stages, the smaller the corresponding compression ratio, reducing the multistage compressor energy consumption.

Based on the above simulation results, the average distribution method of the multistage compression ratio was considered, so the number of compression stages (m) can be expressed as follows:

$$m = \ln\frac{p_2}{p_1} / \ln\varepsilon \tag{12}$$

Table 5. Simulation results of biogas compression under four operating conditions

	Interstage Compression Power / kW				Interstage Compression Power / kW			
	1	2	3	4	1	2	3	4
Condition 1	29.377	29.233	28.627	27.934	30.248	31.091	32.619	36.884
Condition 2	37.120	29.293	26.406	22.479	38.309	31.530	30.776	30.355
Condition 3	24.180	27.093	29.025	35.317	24.861	28.578	32.397	45.451
Condition 4	27.269	31.494	30.910	25.534	28.060	33.442	35.341	34.035

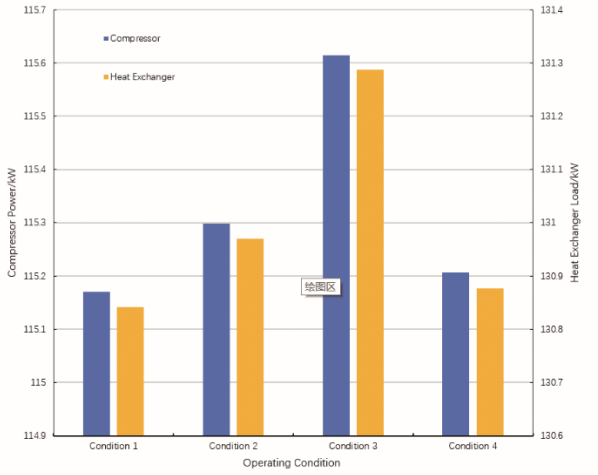

Figure 3. Compressor power and heat exchanger load under four operating conditions.

where p_1 and p_2 are imported pressure and outlet pressure MPa, respectively.

Based on the above conditions, the biogas compression process with the mass flow rate of 1214.85 kg/h and final pressure of 4.908 MPa was simulated. The one-stage to five-stage compression conditions were set for analysis, respectively. The Pressure Changers/Compr and Heat Exchangers/Heater modules in Aspen Plus were used to simulate the biogas compression process, and the simulation results are shown in Table 6.

As shown in Table 6, the power of the one-stage compressor is ~156.302 kW, and the power of the five-stage compressor is ~112.560 kW, which was reduced by ~44 kW. As a result, the outlet temperature of the

Table 6. Simulation results of biogas compression under different compression stages

Number of stages	Interstage compression ratio	Compressor power / kW	Average outlet temperature between compressor stages / ℃	Interstage cooling outlet temperature / ℃	Heat exchanger load / kW
1	19.632	156.302	321.84	25	-171.974
2	4.431	128.475	161.70	25	-144.147
3	2.698	119.550	113.25	25	-135.222
4	2.105	115.170	90.05	25	-130.842
5	1.814	112.560	76.47	25	-128.232

compressor stage decreased from 321.84 °C to 76.47 °C, and the heat exchanger load decreased from 171.974 kW to 128.232 kW. Therefore, in practical engineering, the multistage compression method is often used to reduce the outlet temperature of compressors. In addition, the compressor power, interstage cooling outlet temperature, and heat exchanger load all decrease with the increase in the number of compression stages, and the decreasing trend gradually slows down, as shown in Fig. 4.

Besides the number of compression stages, the outlet temperature of the interstage cooler is one of the main factors affecting energy consumption in the multistage compression process. In the simulation, the outlet temperatures of the interstage coolers with three stages, four stages, and five stages of compression were set to 15°C, 20°C, 25°C, 30°C, and 35°C, respectively.

The simulation results show that the power of the three-stage compressor is 116.648, 118.102, 119.550, 120.990, and 122.419 kW, respectively. Under the same working conditions, the power of the four-stage compressor is 111.948, 113.563, 115.170, 116.768, and 118.354 kW, respectively. The power of the five-stage compressor is 109.161, 110.865, 112.560, 114.245, and 115.920 kW, respectively. The power of the compressors with different compression stages varies with the outlet temperature of the interstage cooler, as shown in Fig. 5. As seen in Fig. 5, the compressor power increases with the increase in the

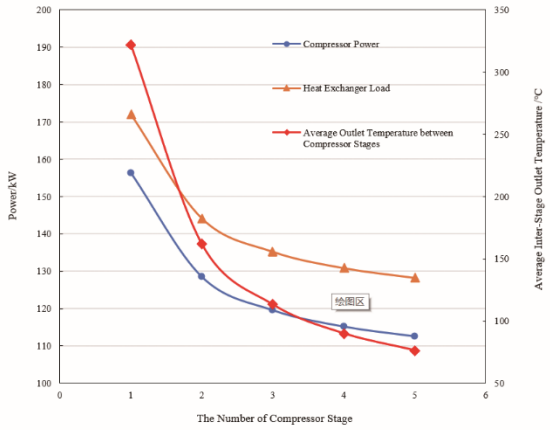

Figure 4. Variation of heat exchanger load, compressor power, and average interstage outlet temperature with a compression stage.

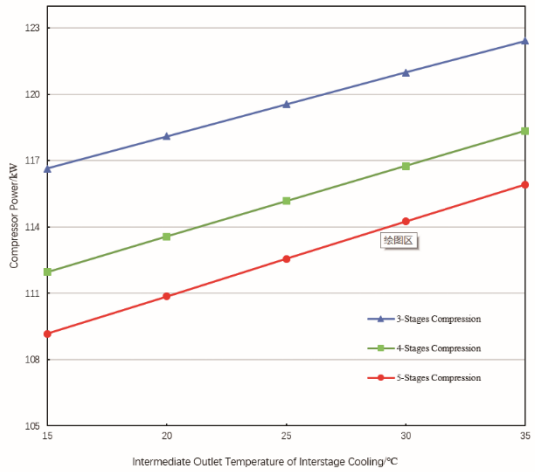

Figure 5. Variation of compression power with the outlet temperature of the interstage cooler.

outlet temperature of the interstage cooler. The simulation results show that in the biogas four-stage compression process, when the interstage cooling temperature decreases by 5 °C on average, the energy consumption in the whole compression process is reduced by ~1.5 kW.

Since equipment cost increases with increasing the number of compression stages, and the outlet temperature of the interstage cooler of compressed gas is usually higher than that of the circulating cooling water, it is necessary to comprehensively evaluate the factors, such as the equipment and energy consumption costs, in practical engineering applications.

Exergy analysis of multistage compression process

When the benchmark state is fixed, meaning that the pressure and temperature of the compressed gas are determined, the energy and exergy of the gas are determined [24]. The benchmark pressure was set to 101.3 kPa. The benchmark temperature was set to 298.15 K. The relevant thermodynamic parameters of the beginning and end states of biogas were simulated by Aspen Plus, as shown in Table 7.

Table 7. Thermodynamic parameters of the initial and final states of the biogas

Items	Unit	Initial state	Final state
Pressure	kPa	250	4908
Temperature	K	298.15	298.15
Enthalpy	kJ/mol	-202.179	-203.444
Entropy	kJ/mol·K	-0.0482	-0.0771
Flow Rate	kmol/hr	44.615	44.615

As seen in Table 7, under the isothermal condition, when the gas is compressed, the enthalpy when the final pressure of the gas is high is lower than that when the initial pressure is low. It results from the decrease of the gas enthalpy due to the exothermic isothermal compression. In addition, the final gas entropy is lower than the initial gas entropy because with the increase in gas pressure, the molecular arrangement tends to be ordered, and the entropy decreases.

The Aspen Plus software was used to simulate the thermodynamic parameters related to the four-stage compression process of biogas, and the exergy changes in the four-stage compression process were calculated through the exergy definition formula. The results are shown in Table 8.

Table 8. Exergy changes in four-stage compression process

Compression stage	Interstage exergy /kW	Exergy after interstage cooling /kW	Exergy loss after interstage cooling /kW	Interstage exergy efficiency /%
1	53.007	50.141	2.865	76.68
2	75.415	72.448	2.967	76.50
3	97.201	94.072	3.128	76.18
4	118.239	114.637	3.602	75.56

According to the exergy analysis of the compression process in Table 8, the interstage cooling loss of the four-stage compression process is 12.6 kW, accounting for 10.9% of the total compression power. If this thermal energy part can be recovered, the exergy efficiency of the whole compression process can be significantly improved. The exergy value of biogas increased with the increase in pressure. Also, the exergy value increased by ~87.03 kW after the fourth-stage compression process was completed, and the exergy of the biogas decreased after interstage cooling. The cooling water took away the exergy of the compressed biogas due to the increase in the gas

temperature after the interstage cooling process. The relationship between the compression exergy efficiency and the number of compression stages is shown in Fig. 6.

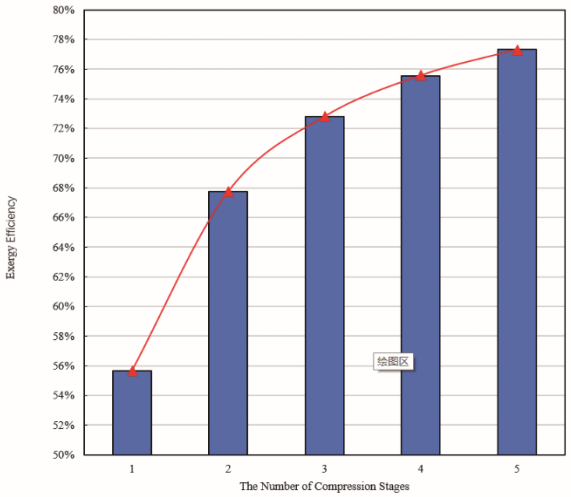

Figure 6. Exergy efficiency changes under different compression stages.

As shown in Fig. 6, the exergy efficiency values of the one-stage compression, two-stage compression, three-stage compression, four-stage compression, and five-stage compression processes are 55.68%, 67.74%, 72.79%, 75.56%, and 77.31%, respectively. Also, the growth rates are 21.66%, 7.47%, 3.80%, and 2.32%, respectively. In the biogas compression process, the exergy efficiency in the compression process increased with the increase in the number of compression stages, but this increase tended to be gradual. Therefore, it is very important to choose appropriate compression stages for application in practical engineering. Based on determining factors, such as the gas flow rate and final pressure conditions, a comprehensive analysis of the exergy efficiency increase, water-saving rate, and equipment costs of different compression stages, a more reasonable compression stage of biogas under the above-mentioned working conditions can be determined.

In the biogas project of an agricultural livestock and poultry breeding farm, it was measured that the exergy increase of final biogas was about 80.60 kW, exergy efficiency was 72.12%, and exergy recovery potential was about 10.88 kW. These simulated results are close to those measured in practical engineering.

CONCLUSION

In this study, a biogas multistage compression process was simulated by the Aspen Plus software. The simulation calculations found that the selection of the number of stages and the compression ratio distribution significantly influenced the simulation results. Overall, the four-stage compression process simulation results and average distribution compression ratio were the best without considering equipment investments.

According to the simulation calculations, in the four-stage biogas compression process, the exergy increase of the final biogas was about 83.07 kW. Its exergy efficiency was 75.56%, and the recovery exergy potential was ~12.6 kW. These results are close to those measured in practical engineering.

The simulation results showed that in the multistage biogas compression process, the total energy consumption decreased by 1.5 kW for every 5 °C decrease in the interstage cooling temperature, where the biogas exergy increases with the increase in pressure. In addition, the exergy efficiency increased with the increase in the number of compression stages, but the increase tended to be slow.

Acknowledgment

This work was supported by the National Natural Science Foundation of China (grant number 52063003) and the Guangxi Innovation-Driven Development Specific Funding Project (grant number GK AA19254010).

REFERENCES

[1] Y. Yuan, Z. Liu, L. Zhao, J. Luo, S. Tang, Y. Zhang, Jiangsu Nong Ye Ke Xue (China) 49 (2021) 28–33.
[2] J. Li, B. Li, W. Xu, Zhongguo Zhao Qi (China) 36 (2018) 3–10.
[3] J. Li, W. Xu, B. Li, D. Zhang, Renewable Energy Resour. 38 (2020) 1563–1568.
[4] X. Xing, R. Wang, N. Bauer, P. Ciais, S. Xu, Nat. Commun. 12 (2021) 31591.
[5] H. Wang, F. Huang, K. Ma, Y. Zhang, Z. Zeng, Zhongguo Zhao Qi 27 (2009) 24–26.
[6] J. Zhao, X. Fan, C. Qiu, C. Wang, N. Liu, D. Wang, S. Wang, L. Sun, Environ. Eng. (Beijing, China)38 (2020) 143–148.
[7] I. Khan, M. Othman, Dzarfan, H. Hashim, T. Matsuura, A Ismail, M. Rezaei-Dasht Arzhandi, I. Azelee, Energy Convers. Manage. 150 (2017) 277–294.
[8] O. Maakoul, R. Beaulanda, H. Omari, E. Essabri, A. Abid, E3S Web Conf. (2021) p. 234.
[9] Y. Han, H. Winston, J. Membr. Sci. (2021). 628.
[10] P. Sutrisna, E. Savitri, J. Polym. Eng. 40 (2020) 459–467.
[11] S. García, L. Rodríguez, D. Martínez, F. Córdova, N. Guzmán, J. Cleaner Prod. 286 (2020) 124940.
[12] K. Li, F. Deng, K. Wei, X. Ma, F. Huang, Contemp. Chem. Ind. 45 (2016) 1159–1162.
[13] G. Tang, X. Hu, J. Zhao, Y. Chen, F. Huang, Contemp.

Chem. Ind. 46 (2017) 983–986, 990.

[14] K. Nachtmann, J. Hofmann, J. Paetzold, S. Baum, H. Bernhardt, Mod. Agri. Sci. Technol. 1 (2015) 1–7.

[15] G. Xu, Y. Yang, L. Duan, N. Wang, L. Tian, PaoJ. Eng. Thermophys. (Beijing, China) 31 (2010) 1643–1646.

[16] S. Zhou, Y. Dong, Y. Zhang, H. Sun, Trans. Chin. Soc. Agric. Mach.42 (2011) 111–116.

[17] A.Yousef, W. Maghlany, Y. Eldrainy, A. Attia, Fuel, 251 (2019) 611–628.

[18] L. Sun, Chemical Process Simulation Training, Chem. Ind. Press, Beijing (2012), p. 2–5.

[19] W. Mao, Study on Recovery and Utilization of Waste Heat between Compressor Stages, 2015, Zhengzhou Univ.

[20] Z. Chen, Advanced engineering thermodynamics, Univ. of Sci. Technol. of China Press, Hefei(2014), p. 31–70.

[21] C. Li, Y. Gao, S. Xia, Q. Shang, P. Ma, Trans. Tianjin Univ.25 (2019) 540–548.

[22] Y. Zhang, Q. Zhang, Comput. Appl. Chem. (China), 35 (2018) 711–718.

[23] Y. Zhang, X. Xu, Xinjiang Hua Gong.(China) 3(2001) 47-49. http://qikan.cqvip.com/Qikan/Article/ReadIndex?id=5477078&info=5vrDCRzniLBCtGqX9kJposoAfxjfRfntka7QR0E5IqY%3d.

[24] W. Guo, H. Lu, X. Wang, B. Zhang, Q. Chen, Pet. Process. Petrochem, 50 (2019) 69–74.

SHUAI ZOU[1,3]
KANGCHUN LI[2,3]
MINGYUAN DOU[1,3]
JING YANG[1,3]
QING FENG[1,3]
FUCHUAN HUANG[1,3]
LIN CHEN[1]

[1]School of Mechanical Engineering, Guangxi University, Nanning, Guangxi, China

[2]School of Chemistry & Chemical Engineering of Guangxi University, Nanning, Guangxi, China

[3]Guangxi Key Laboratory of Petrochemical Resource Processing and Process Intensification Technology, Guangxi University

NAUČNI RAD

EKSERGIJSKA ANALIZA PROCESA VIŠESTEPENE KOMPRESIJE BIOGASA SIMULACIJOM KORIŠĆENJEM SOFTVERA ASPEN PLUS

U ovoj studiji, uzimajući proces odvajanja kompresije u projektu biogasa kao predmet istraživanja, simuliran je proces višestepene kompresije korišćenjem softvera Aspen Plus. Eksergijska analiza projekta biogasa u višestepenoj kompresiji i adijabatskim ili izotermnim uslovima izvršena je primenom termodinamičkog principa. Rezultati su pokazali da se eksergija biogasa povećava sa pritiskom tokom procesa kompresije i shodno tome smanjuje u međustepenom procesu hlađenja. Dalje, serija kompresija se povećava sa povećanjem efikasnosti, ali je povećanje postepeno. Rezultati studije procesa četvorostepene kompresije su sledeći: eksergija procesa je porasla za ~83,07 kV, efikasnost eksergije procesa je ~75,56%, a eksergijski potencijal oporavka ~12,6 kV. U ovoj studiji, softverom Aspen Plus je analizirana raspodela odnosa kompresije i izbor stepena kompresije u okviru procesa višestepene kompresije. Ova analiza na kraju može pomoći drugima da dizajniraju efikasne višestepene sisteme kompresije koji smanjuju gubitke energije.

Ključne reči: Aspen Plus, biogas, eksergijska analiza, višestepena kompresija.

CI&CEQ
Chemical Industry & Chemical Engineering Quarterly

Available online at
Association of the Chemical Engineers of Serbia AChE
www.ache.org.rs/CICEQ

Chem. Ind. Chem. Eng. Q. 28 (4) 329–337 (2022) CI&CEQ

JEEVARATHNAM RAVI KUMAR VINOD KUMAAR[1]
RAJASEKARAN THANIGAIVELAN[2]
MADESH SOUNDARRAJAN[2]

[1]Department of Mechanical Engineering, Mahendra Engineering College, Mahendhirapuri, Namakkal, Tamil Nadu, India

[2]Department of Mechanical Engineering, Muthayammal Engineering College, Rasipuram, Namakkal, Tamil Nadu, India

SCIENTIFIC PAPER

UDC 544.6:669.1

EFFECT OF DIFFERENT ELECTROLYTES ON ELECTROCHEMICAL MICRO-MACHINING OF SS 316L

Article Highlights

- This paper aims to fabricate the drilled micro-holes on SS 316L through the ECMM process
- Tartaric acid, citric acid, and mixed electrolyte are used for conducting the experiments
- MRR and overcut are considered to measure the performance of the machining process
- FESEM analysis is conducted to see the influence of the electrolyte on the machining surface
- Mixed electrolyte outperforms MRR and overcut than the other electrolytes

Abstract

The use of stainless steel 316L (SS 316L) in the medical, marine, aerospace, bio-medical, and automobile sectors increases rapidly. Electrochemical micro-machining (ECMM) is the appropriate method for machining SS 316L due to its burr-free machining surface, no residual stress, and high precision. However, some limitations are found in using strong electrolytes, such as HCl, H_2SO_4, KOH, $NaNO_3$, and NaCl, which reportedly face difficulties in disposing to the environment and handling issues. Hence, this paper addresses overcoming the disadvantages encountered in the ECMM process when using strong electrolytes to machine SS 316L. Therefore, different organic electrolytes such as tartaric acid ($C_4H_6O_6$), citric acid ($C_6H_8O_7$), and a combination of tartaric and citric acid (mixed electrolyte) are considered to select the best electrolyte. Process parameters like machining voltage, duty cycle, and electrolyte concentration are included in determining machining performance. The performance of ECMM is evaluated using material removal rate (MRR) and overcut. The overcut of tartaric acid electrolyte is 179% less than mixed electrolyte for the parameter combination of 12 g/l, 11 V, and 85%. On the other hand, the mixed electrolyte shows 114.2% higher MRR than the tartaric acid electrolyte for the parameter solutions of 25%, 11 V, and 20 g/l. Furthermore, the citric acid electrolyte shows the second-lowest overcut and higher MRR in all aspects of machining performance. Field emission scanning electron microscope (FESEM) studies are carried out to realize the effect of electrolytes on the machining surface.

Keywords: micro-machining, weak electrolytes, electrochemical, SS 316L, MRR, overcut.

In non-traditional machining methods, several machining techniques are available for machining SS 316L material, like ultrasonic machining, laser beam machining, electron beam machining process, and electro-discharge machining. Even though those methods are expensive, they have a lower surface quality due to the thermal application on the machining zone [1]. The ECMM process is one of the most prominent and most suitable techniques for machining materials like SS [2]. Since the ECMM method encom-

Correspondence: J.R. Vinod Kumaar, Department of Mechanical Engineering, Mahendra Engineering College (Autonomous), Mahendhirapuri, Namakkal (Dt), Tamil Nadu, India-637 503.
E-mail: jrvinod@gmail.com
Paper received: 4 December, 2021
Paper revised: 21 April, 2022
Paper accepted: 19 May, 2022

https://doi.org/10.2298/CICEQ211204007V

passes characteristics such as burr-free machining surfaces, no heat is produced during the machining process, tool and workpiece wear are less and high accuracy [3,4]. However, because of technological growth and demand for micro products, ECMM needs to be updated in all aspects of machining. Also, every material finds a unique character based on the particles mixed up, demonstrated by its mechanical strength [5,6]. In the same way, materials could be dissolute by electrochemical reactions based on the type of electrolyte used [7]. Therefore, many researchers have carried out experiments with different electrolytes and their modifications in the last decade. Moreover, strong electrolytes contribute to a larger overcut and more material removal from the previous literature. Still, at the same time, it also causes hazards to the environment and operator. Therefore, to compensate for the drawbacks faced in using strong electrolytes, this paper proposes to use weak electrolytes for the machining of SS 316L.

In line with that, Thangamani *et al.* [8] used different electrolytes such as sodium nitrate ($NaNO_3$), plain sodium chloride (NaCl), and NaCl with citric acid as a mixed electrolyte for the ECMM of titanium alloy. They found that plain NaCl and $NaNO_3$ electrolytes had a higher MRR, while mixed NaCl and citric acid electrolytes had a lower overcut and taper angle. Patel *et al.* [9] adopted the novel setup with $NaNO_3$ electrolyte to atomize its molecular mist in the ECMM of SS 304 work material. They mentioned that the atomized flushing technique improves the 52% machining rate and reduces the overcut by about 13% with 6 V machining voltage. Also, the consumption of electrolytes for the ECMM process is reduced significantly. Kumarasamy *et al.* [10] used various electrolytes for the ECMM of haste alloy, including NaCl, $NaNO_3$, and a mixture of these two with citric acid electrolyte. They optimized the process parameters using the Taguchi method with the outcome of surface roughness, MRR, taper angle of the micro-hole and overcut. They also mentioned that the mixed electrolyte shows a significant improvement in the results of the ECMM.

In the ECM process, Zhan *et al.* [11] applied pressurized gas to the surroundings of the tool electrode with varying parameters. They noted that pressurized gas prevents stray current effects on the workpiece, which significantly improves the precision of micro-holes. Also, this gas supply acts as tool insulation and improves the electrolyte localization effect due to the conductivity improvements. As a result, the surface roughness of the micro-hole improved about 52 times higher than the typical electrolyte. Soundarrajan *et al.* [12] mixed the hot and dry air in the citric acid electrolyte for machining copper work material. They reported that hot air energies the electrolyte more, which increases the machining rate by 2 times better than the dry air mixed electrolyte. The dissolution products of copper work material act as an insulation layer for the tool electrode and prevent the stray current effect on the work surface. This phenomenon improves the taper angle of the micro-hole significantly. Mouliprasanth *et al.* [13] attempted to use the ECMM process with passivating and non-passivating electrolytes for shape memory alloys. They optimized the process parameters through the Taguchi technique over the outcomes of MRR, taper angle, and overcut. Subburam *et al.* [14] optimized the process parameters of ECMM with citric acid electrolyte for SS 304 material. They applied the grey relational analysis optimization technique to find the optimal electrolyte solution and process parameters for the ECMM method. It was also suggested that the parameter combination of 20g/l electrolyte concentration, 12 V machining voltage, and 15 ms pulse on-time produces the highest machining rate and less overcut.

Soundarrajan *et al.* [15] mixed hydrochloric acid with $NaNO_3$ electrolyte for machining the aluminum metal matrix composite. First, they compared the results of the acidified electrolyte with those of the non-acidified electrolyte. They found that the acidified electrolyte produces 3.5 times higher MRR than the non-acidified electrolyte for the parameter combination of 15 V, 30 g/l, and 90%. Next, Guo *et al.* [16] tried the ethylene glycol-based $NaNO_3$ electrolyte for machining the zirconium metallic glass in the ECM process. They noted good stray current protection in the machining zone compared to the water-based electrolyte, which causes very little pitting correction on the machining surface. Finally, Ao *et al.* [17] tried a 20% ethanol mixed ethylene glycol-based NaCl electrolyte in the ECMM of a shape memory alloy. They reported that 20% of ethanol mixed with electrolyte reduces the oxide layer formation that causes the smooth machining roughness. At the same time, machining precision is more affected when the ethanol percentage is exceeded.

Vinod Kumaar *et al.* [18] adopted the magnets in the citric acid electrolyte using the ECMM process to machine SS 316L work material. A magnetic field induces the molecules present in the electrolyte, which causes a higher electrical conductance and a twice better machining rate than the plain citric acid electrolyte. Soundarrajan *et al.* [19] heated the $NaNO_3$ electrolyte using ultraviolet rays in the ECMM of copper material. They reported that the 2.56 times higher MRR is achieved due to the heat of the electrolyte workpiece getting softened and the UV rays of short wavelength,

which causes the 2.56 higher MRR than the infrared heated electrolyte. However, there was a significant overcut on the micro-holes due to electrolyte energy. Chen *et al.* [20] created the micro dimples on titanium alloy with the ECMM process using $NaNO_3$ electrolyte. They noted that continuous oxide layer formation causes stray current pitting on the machining surface. They also suggested process parameters for better machining performance, such as 24 V, 100 Hz frequency, and 10% duty cycle. Raj Keerthi *et al.* [21] used the $NaNO_3$ electrolyte for the Co-Ni-Cr-W superalloy in the ECMM process using two different tools: a fabricated hollow tool and a typical cylindrical tool. They compared the results, such as circularity, surface roughness, and MRR, of the hollow tool with those of the usual tool using $NaNO_3$ electrolyte. The results show that 2% MRR increased and 24% overcut was reduced with the hollow tool compared to the standard tool.

Vinod Kumaar *et al.* [22] studied the effects of using the oxalic acid electrolyte for machining SS 316L work material in the ECMM process. They reported that oxalic acid enhances the MRR by 2.5 times and reduces the overcut significantly. Wang *et al.* [23] proposed the inner wall modified nozzle for electrolyte supply in the machining zone. They noted stray current was less in the machining zone due to the turbulated electrolyte, which increases the machining accuracy on the nickel work material. Kunar *et al.* [24] tried various electrolytes such as NaCl and $NaNO_3$ and the combinations of these two electrolytes for SS 304 materials in the ECMM process. They discovered that a combined electrolyte of NaCl and $NaNO_3$ outperforms the plain electrolyte in terms of machining performance. The above literature clarifies that researchers have employed various electrolytes to enhance the machining performance of ECMM. Although different electrolytes are commercially available, the cost of machining on a large scale is prohibitively expensive. Strong electrolytes, such as acid-based and alkaline-based electrolytes, continue to face significant challenges in terms of environmental measures, cost, and human safety [25]. Some research findings explored the results of ECMM process parameters with organic electrolytes, whereas there is no evidence for SS 316L with an organic electrolyte. Hence, in this work, commercially available, natural, weak, and less expensive electrolytes such as citric acid, tartaric acid, and mixed acid are used as electrolytes. The design of experiments is planned, including the machining parameters, such as machining voltage, duty cycle, and electrolyte concentration. FESEM analyses are taken to see the effect of the electrolyte on micro-holes and the surface.

The proposed chemical reaction of the electrolyte

Citric acid is one of the organic acids obtained from natural plants such as lemons and oranges. Usually, citric acids are used in industries like metal polishing, food, paint manufacturing, and chemicals due to their affinity nature. Also, this is one of the best chelating agents to clean the SS work materials [18]. Hence, in this experiment, citric acid is considered the electrolyte. In the ECMM process, materials dissolve on the workpiece by applying electric potentials between the tool and work. Due to these potential changes in the electrolyte, a reaction occurs in the machining process. Citric acid is a triprotic or tricarboxylic acid group of acids that can be subjected to equation (2) and separated by distilled water (1). Hence, the citric acid could be dissolved in distilled water and leave one hydrogen present in the equation (3). This hydrogen forms the hydronium ions when reacted with oxygen in distilled water.

$$(H_2O) \rightarrow (H^+) + (OH^-) \quad (1)$$

$$(C_6H_8O_7) \rightarrow (C_6H_5O_7)^{3-} + 3H^+ \quad (2)$$

$$(C_6H_8O_7) + (H_2O) \rightarrow (C_6H_5O_7)^{3-} + (H_3O^+) \quad (3)$$

Tartaric acid is one of the diprotic or two carboxylic groups of acids and weak organic acids extracted from fruits such as grapes, bananas, tamarinds, etc. The reactions of tartaric acid when mixed with distilled water are present in the following equations. Equations (4) and (3) exhibit the reaction of tartaric acid and distilled water together. As per the equation (5), hydrogen from the tartaric acid joins with oxygen and forms the hydronium ion (H_3O^+):

$$(C_4H_6O_6) \rightarrow (C_4H_4O_6)^{2-} + (2H^+) \quad (4)$$

$$(C_4H_6O_6) + (H_2O) \rightarrow (C_4H_4O_6)^{2-} + (H_3O^+) \quad (5)$$

Mixing citric acid and tartaric acid may undergo the following reaction, represented in equation (6). Citrate anions $(C_4H_4O_6)^{2-}$ and D-tartrate anions $(C_6H_5O_7)^3$ are formed when both acids mix. Also, the hydronium ion is created, which is defined in the equation:

$$(C_6H_8O_7) + (C_4H_6O_6) + (H_2O) \rightarrow (C_6H_5O_7)^{3-} + (C_4H_4O_6)^{2-} + (H_3O^+) \quad (6)$$

Metal oxidation occurs on the SS 316L work piece. In all three acids (citric, tartaric, and combination of citric and tartaric acid), the following reaction may occur, which is presented in equation (8).

$$(Fe) \rightarrow Fe^{2+} + 2e^- \quad (7)$$

$$(C_6H_5O_7)^{3-} + (C_4H_4O_6)^{2-} + Fe^{2+} \rightarrow Fe_3(C_6H_5O_7)_2(C_4H_4O_6) \quad (8)$$

The ferrous metal ion reacts with hydrogen in the electrolyte and forms ferrous citrate $Fe_3(C_6H_5O_7)$ and tartrate. This formation is termed 'sludge' in the electrolyte and acts as a conductive bridge.

In the cathode, hydrogen bubbles are released from the electrode while machining.

$$2H^+ + 2e^- \rightarrow H_2 \uparrow \quad (9)$$

MATERIAL AND METHODS

The ECMM setup is represented in Figure 1, which was developed indigenously for conducting the experiments. The setup comprises various parts like an electrolyte tank, tool feed control system, filter, and pulse rectifier. The experiments were conducted with a SS 316L workpiece with a 500 μm thickness and employed as an anode. The pulse frequency is set at 100 Hz, and the total pulse width is 10 milliseconds. The tool electrode of size φ 460 μm is employed as a cathode and insulated using epoxy resin, preventing stray current in the machining zone. The constant tool feed rate is applied while machining the material. The performance of ECMM has been measured with an assessment of MRR and overcut. Through-hole with respect to the machining time is considered for MRR, and differences in micro-hole diameter and tool diameter are considered for the overcut. An optical microscope is used to find out the diameter of the micro-hole. The natural phenomenon, namely the triprotic property of citric acid, prevents the formation of unwanted sludge (insoluble) in the machining zone, thereby maintaining the electrolyte character until the end of the experiment [12]. Also, the effects of other weak electrolytes such as citric acid, tartaric acid, and the mixing of citric and tartaric acid were considered for the experiments. The experiment plan is based on varying one parameter at a time, keeping all other factors constant. The experimental results are presented in Table 1.

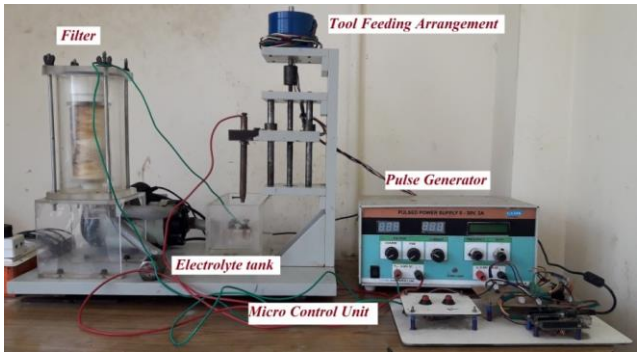

Figure 1. Experimental arrangement of ECMM.

The research on mixed electrolytes for ECMM provided the best solution due to the atom migrations between the electrolytes. Therefore, to obtain the best machining performance on ECMM, citric acid and tartaric acids are mixed in equal proportion and considered an electrolyte for the experiment. The preparation of mixed acid electrolyte combinations is presented in Table 2. In addition, other electrolytes such as tartaric and citric acid are used as they are in their regular form. The conductivity of ions in the electrolyte is initially determined using the following equation: = L/RWt, where L is the distance between the electrodes, R is the resistance of the electrolyte solution offered between the two electrodes at a fixed distance, t is the thickness of the coating, and W is the width of the substrate. While conducting the experiments, we observed that the electrical conductivity in the mixed electrolyte performs best rather than the citric acid electrolyte and tartaric acid due to more inter-ionic interactions taking place between the compounds, and there is also an improvement in the dissociation of the electrolyte.

RESULTS AND DISCUSSION

Influence of machining voltage on overcut and MRR

Figure 2 shows the effect of machining voltage on overcut and MRR with various electrolytes such as citric acid, tartaric acid, and mixed electrolyte. As per the graph, an increase in the machining voltage shows the increasing trend for overcutting and MRR for all electrolytes. The tartaric acid electrolyte produces a 34 μm overcut for 7 V, 85 %, and 20 g/l, and this value is the least overcut among all electrolytes. At the same time, the least material removal was obtained for the same parameter combination. Furthermore, due to the lower conductivity of the tartaric acid electrolyte, the insulation of tool coating withstands for a longer period in the tartaric acid electrolyte, reducing the stray cut in the machining zone and producing 77.9% less overcut than in the mixed electrolyte [26]. It is apparent from Figure 3(a) that the SEM image of the micro-hole shows a smooth machining surface. For the same parameter combination, the citric acid electrolyte produces a 49 μm overcut, 44.1% less than the mixed electrolyte. In the citric acid electrolyte, the cathode releases a moderate amount of gas bubbles, which paves the way for a homogeneous supply of current density in the machining zone. This uniform current distribution of the citric acid electrolyte leads to the second lesser overcut among the electrolytes [27]. Moreover, tartaric acid and citric acid produce a 47 μm (76% improvement) and an 89 μm (24.5% improvement) overcut, respectively, for the parameter level of 8 V, 85%, and 20 g/l. It is apparent from Figure 3(b) that the SEM image shows

Table 1. Experimental results of weak electrolytes

Ex. no	Machining voltage (V)	Duty cycle (%)	Electrolyte concentration (g/l)	Machining time (s)		
				Mixed electrolyte	Citric acid electrolyte	Tartaric acid electrolyte
1	7	85	20	1279.00	1715.56	2435.46
2	8	85	20	1009.01	1242.16	1658.93
3	9	85	20	907.49	992.00	1291.99
4	10	85	20	779.62	825.68	1212.12
5	11	85	20	629.52	795.67	975.04
6	11	25	20	1179.00	1578.00	2525.25
7	11	40	20	1092.53	1288.00	1678.70
8	11	55	20	1002.00	1172.00	1321.35
9	11	70	20	730.46	1023.00	1212.12
10	11	85	20	629.52	795.67	975.04
11	11	85	12	1554.00	1652.00	2304.15
12	11	85	14	1110.77	1379.99	1543.21
13	11	85	16	924.64	1273.03	1370.61
14	11	85	18	813.42	1106.00	1163.33
15	11	85	20	629.52	795.67	975.04

Table 2. Design of experiments for mixed electrolyte

Electrolyte concentration (g/l)	Mixed electrolyte (g/l)
12	6 g/l Tartaric + 6 g/l citric
14	7 g/l Tartaric + 7 g/l citric
16	8 g/l Tartaric + 8 g/l citric
18	9 g/l Tartaric + 9 g/l citric
20	10 g/l Tartaric + 10 g/l citric

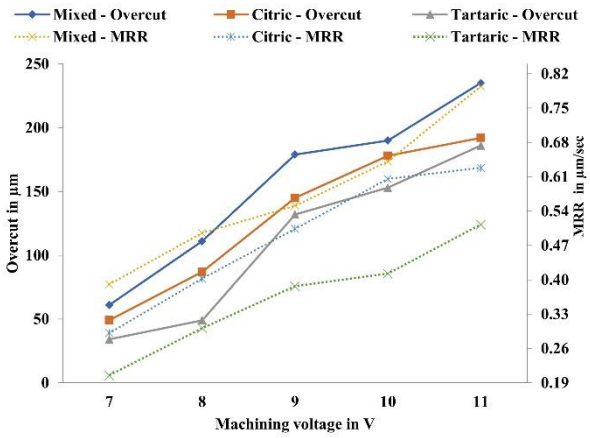

Figure 2. Influence of machining voltage on Overcut and MRR.

the less defected micro-hole on the machined surface. The mixed electrolyte produces the highest overcut, and, as is evident from Figure 3(c), the SEM image of the micro-hole shows over-etched surfaces.

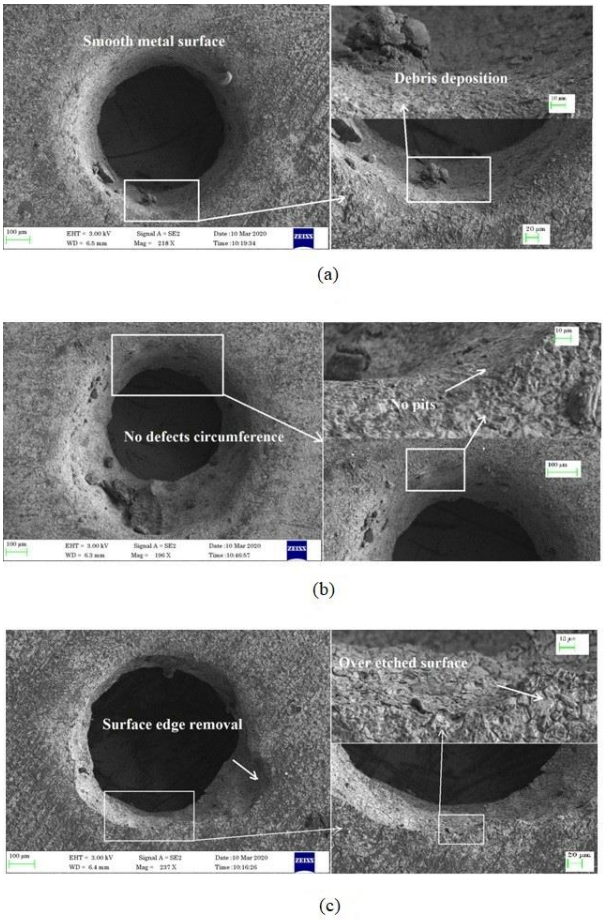

Figure 3. SEM image of the machined micro-hole at 7 V, 85 % and 20 g/l(a) tartaric acid (b) citric acid (c) mixed electrolyte.

The influence of machining voltage on MRR through various electrolytes is presented in the graph. The mixed electrolyte produces the highest MRR of all the electrolytes. In the case of a mixed electrolyte, citric acid and tartaric acid are mixed equally by weight, which accelerates the movement of ions in the electrolyte. It shows a 90.4% higher MRR than the plain citric and tartaric acid electrolytes at the parameter levels of 7 V, 85.0%, and 20 g/l. The graph indicates that the machining voltage from 7 V to 9 V shows the linear increment in MRR. While machining, the higher displacement of ions occurs in the machining zone with the help of hydronium ions. The reaction of citric and tartaric acids liberates hydrogen bubbles, which react with oxygen molecules to form hydronium ions [28]. In a mixed electrolyte, the combination of both acids doubles the formation of hydronium ions due to the citrate and d-tartrate ions [29]. Also, hydronium ions continuously migrate from one atom to another, which causes higher conductivity. The higher conductivity of the electrolyte produces the higher MRR with the mixed electrolyte. Moreover, the MRR is 64.4% and 42.2% for the mixed electrolyte, compared to the plain electrolyte at 8 V and 9 V, respectively. Also, at 11 V, it produces a 54.9% higher MRR than the tartaric acid electrolyte. The citric acid electrolyte shows the second-highest MRR compared to the tartaric acid electrolyte. Commonly, hydronium formation in citric acid is slightly higher than in tartaric acid, which causes higher conductivity when increasing the machining voltage. Citric acid produces a 41.9% higher MRR than tartaric acid electrolyte for parameter solutions of 7 V, 85%, and 20 g/l, respectively; similarly, MRR was found to be 33.5%, 30.2%, 46.8%, and 22.5% higher at machining voltages of 8 V, 9 V, 10 V, and 11 V, respectively.

Influence of duty cycle on overcut and MRR

Figure 4 depicts the effects of the duty cycle on overcut for the different electrolytes used in this experiment. It presents that tartaric acid electrolyte produces 46 μm overcut for the parameter solution of 25%, 11 V, and 20 g/l than the mixed electrolyte of 107 μm overcut for same parameter level combination and provides the enhancement of 132.9%. The production of hydrogen bubbles in the tartaric acid electrolyte at the machining zone contributes to less overcut [30]. Compared with other electrolytes, fewer hydrogen bubbles are formed in tartaric acid. This evolution of bubbles produces less distribution and provides more stable machining [31,32]. Therefore, lower overcut and good circumference were obtained in the tartaric acid electrolyte, as evident from Figure 5 (a).

At 40%, 11 V, and 20 g/l, the tartaric acid and citric acid electrolytes produce 74 μm and 98 μm overcuts, respectively. These overcut values are 94.6% and 32.40% less than the mixed electrolyte overcut of 144 μm. Also, the duty cycle of 55%, 70%, and 85% improves overcut, such as 46.9%, 56.9%, and 18.3%, respectively, with tartaric acid electrolyte than with mixed electrolyte. According to the graph, citric acid electrolyte produces less overcut than the mixed electrolyte. The citric acid electrolyte produces a 77 μm overcut for the parameter level at 25%, 11 V, and 20 g/l, and for the same parameter combination, the mixed electrolyte shows an improvement of 67.4%. Moreover, the duty cycle of 55%, 70%, and 85% improves overcut by 32.1%, 31.2%, and 25.4% with citric acid electrolyte, respectively, than the mixed electrolyte. It is evident from Figure 5 (b) that the micro-hole with an almost circular circumference and slight microcracks were found on the machining surface, and Figure 5 (c) shows the SEM image of the micro-hole with a wavier circumference that was found for the mixed electrolyte.

According to the graph, mixed electrolyte produces a higher MRR than tartaric acid electrolyte, and increasing the duty cycle increases the MRR. In the mixed electrolyte, heat generation at the machining zone is induced due to the double hydrated anions such as tartrate and citrate. Generally, a synergistic effect was developed due to the heat propagation in the electrolyte. The heating of the electrolyte increases the electrolyte density, and this lower density electrolyte conducts electricity faster than the normal electrolyte [33]. This factor is comparatively smaller in the other electrolytes. Hence, the mixed electrolyte produces a 114.2% higher MRR than the tartaric acid electrolyte for the parameter levels of 25%, 11 V, and 20 g/l. As for the citric acid electrolyte, MRR was 60% higher than tartaric acid electrolyte for the same parameter combination. It is a common fact that citrate anions are stronger than tartrate anions. Therefore, stronger acid accelerates the ion movement faster than less strong acid, which results in a higher MRR with citric acid electrolyte. Furthermore, at 55%, 70%, and 85% duty cycles, they produce a 31.9%, 65.9%, and 66.2% higher MRR with the mixed electrolyte than tartaric acid. For the same duty cycle values, citric acid produces a 12.7%, 18.4%, and 2.38% improvement in MRR than the tartaric acid electrolyte.

Influences of electrolyte concentration on overcut and MRR

Figure 6 shows the electrolyte concentration and its influences on overcut and MRR. The tartaric acid electrolyte produces a lower overcut than the mixed electrolyte. It is evident from figure 10 that the overcut for the tartaric acid electrolyte of 53 μm is attained, which is less than the mixed electrolyte for the parameter solution of 12 g/l, 11 V, and 85%. This value is around a 179% improvement and the least overcut

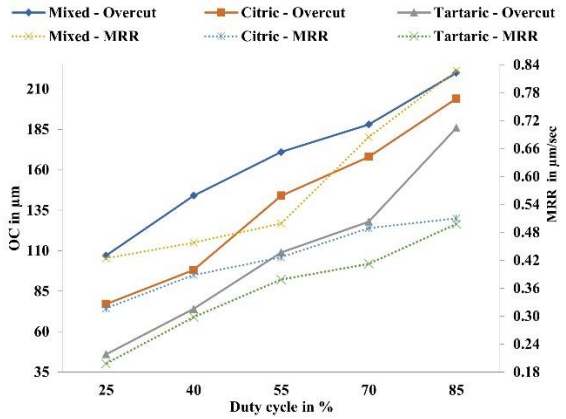

Figure 4. Influence of duty cycle on Overcut and MRR.

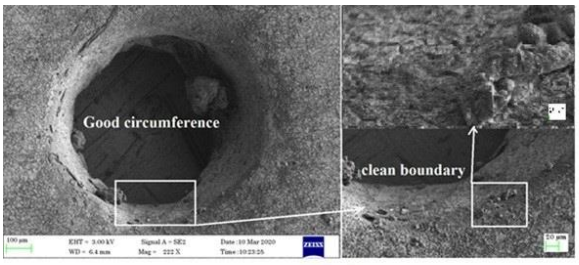

(a)

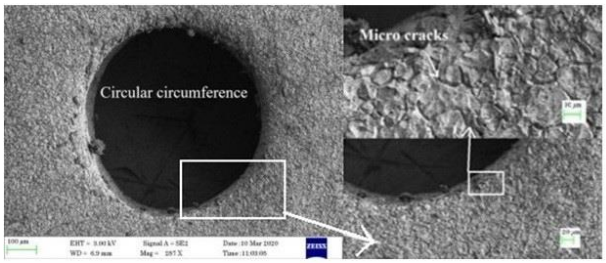

(b)

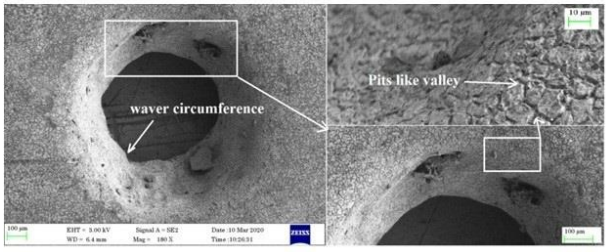

(c)

Figure 5. SEM image of the machined micro-hole at 25%, 11 V, and 20 g/l (a) tartaric acid (b) citric acid (c) mixed electrolyte.

value among the experiments. Also, the overcut is 106.2% lower at 14 g/l and 61.3% lower at 16 g/l electrolyte concentration with the same electrolyte. The causes of electrochemical reactions such as electrolyte softening, heat production, and debris stuck in the machining zone are comparatively very small in the tartaric acid electrolyte.

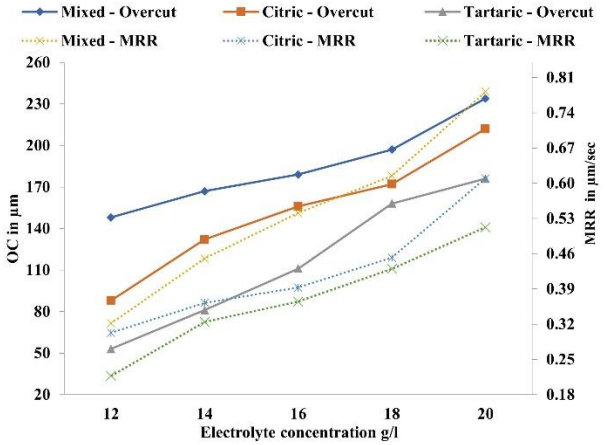

Figure 6. Influence of electrolyte concentration on overcut and MRR.

Therefore, less overcut is obtained for the tartaric acid electrolyte. Figure 7 (a) shows the SEM image of a machined micro-hole for tartaric acid with a neat circular profile. The second lesser overcut is observed for the citric acid electrolyte. It is apparent from the graph that the citric acid electrolyte shows an 88 µm overcut, which is 66% less compared to the mixed acid electrolyte for the parameter level at 20 g/l, 11 V, and 85%.

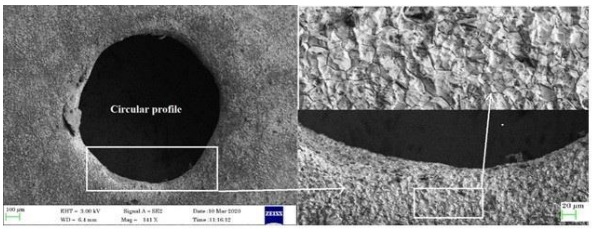

(a)

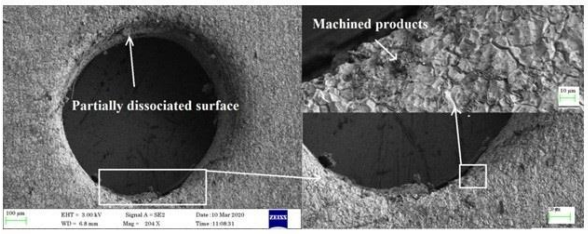

(b)

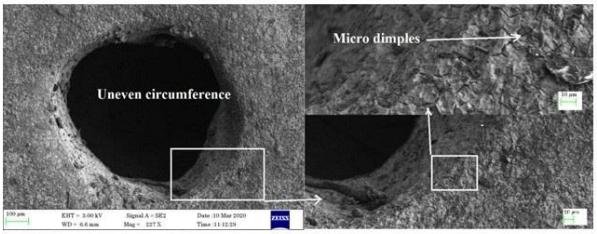

(c)

Figure 7. SEM image of machined micro-hole at 12 g/l, 11 V, and 85% (a) tartaric acid (b) citric acid (c) mixed electrolyte.

With the citric electrolyte, the continuous production of gas bubbles eliminates the machined products from the inter-electrode gap by its pulling force. This factor prevents the stray current effect and maintains a debris-free machining zone. Hence, the citric acid electrolyte produces the least overcut compared to the mixed acid electrolyte. Figure 7(b) presents its micro-hole SEM image with a partially dissociated surface. Again, a mixed electrolyte produces the highest overcut of all electrolytes. It is evident in SEM images, Figure 7(c), which presents the uneven circumference of the micro-hole.

It is apparent from the graph that mixed acid electrolyte gives a higher MRR compared with tartaric acid electrolyte. In the mixed acid electrolyte, the machined products play a major role in the higher MRR. It is a general fact that an increase of ions in the electrolyte solution increases the mobility of electrons. The higher concentrated electrolyte obtained through the mixed electrolyte, i.e., citrate and tartrate ions, accelerates the electrons faster than the individual electrolytes.

This phenomenon increases the conductivity of the electrolyte, resulting in higher sludge formation. As a result, for the parameter level of 12 g/l, 11 V, and 85%, the mixed acid electrolyte produced a 48.3% higher MRR than the tartaric acid electrolyte. Likewise, citric acid shows the next highest, i.e., 39.3% improved MRR than tartaric acid electrolyte for the same parameter combination. Furthermore, at electrolyte concentrations of 16 g/l, 18 g/l, and 20 g/l, the mixed acid electrolyte has a 48.2%, 49.0%, and 39.0% higher MRR than the tartaric acid electrolyte, respectively. In citric acid, for the same electrolyte concentration levels, 7.6%, 5.18%, and 18.9% higher MRR are obtained than the citric acid electrolyte.

CONCLUSION

In this present work, micro-holes are fabricated on SS 316L material using different electrolytes such as tartaric acid, citric acid, and mixed electrolyte to identify the best electrolyte for the ECMM process results compared with each other. According to the performance results, tartaric acid produces a 179% less overcut at 12 g/l, 85%, and 11 V than the mixed electrolyte. At the same time, the citric acid shows a 66% less overcut than the mixed electrolyte for the same parameter solution. At 25%, 11 V, and 20 g/l, the MRR with the mixed and citric acid electrolytes is higher by 114.2% and 60.2%, respectively, than with the tartaric acid electrolyte. Therefore, the mixed electrolyte can be used for better MRR where accuracy is not a significant phenomenon. Compared to other electrolytes, tartaric acid is suitable for machining with smaller overcut, and citric acid produces intermediate results in all aspects. Hence, the citric acid electrolyte can be proposed for better MRR and overcut. So, further experiments can be conducted with an eco-friendly citric acid electrolyte to improve the machining performance.

REFERENCES

[1] R. Thanigaivelan, R.M. Arunachalam, M. Kumar, B.P. Dheeraj, Mater. Manuf. Process. 33 (2018) 383–389.

[2] S. Ayyappan, K. Sivakumar, M. Kalaimathi,Int. J. Mach. Mach. Mater.17 (2015) 79–94.

[3] S. Maniraj, R. Thanigaivelan, Mater. Manuf. Processes. 34 (2019) 1494–1501.

[4] M.Soundarrajan, R. Thanigaivelan, in Advances in Micro and Nano Manufacturing and Surface Engineering, M. Shunmugam, M. Kanthababu (eds), Springer, (2019), pp. 423–434.

[5] F. Zheng, X. Ou, Q. Pan, X. Xiong, C. Yang, M. Liu,J. Power Sources 346 (2017) 31–39.

[6] M.Bester-Rogac, R. Neueder, J. Barthel, A.Apelblat, J. Solution Chem.26 (1997) 537–550.

[7] R.A. Jothi, S. Vetrivel, S. Gopinath, R.U. Mullai, E. Vinoth, Appl. Phys. A: Mater. Sci. Process.127 (2021) 1–8.

[8] G. Thangamani, M. Thangaraj, K. Moiduddin, S.H. Mian, H. Alkhalefah, U. Umer, Metals 11 (2021) 247.

[9] DS. Patel, V. Sharma, V.K. Jain, J. Ramkumar, J. Electrochem. Soc.168 (2021) 043504.

[10] G. Kumarasamy, P. Lakshmanan,G. Thangamani,Arabian J. Sci. Eng. 46 (2021) 2243–2259.

[11] S. Zhan, Y. Zhao, J. Mater. Process. Technol. 291 (2021) 117049.

[12] M. Soundarrajan, R. Thanigaivelan, Russ. J. Electrochem. 57 (2021) 172–182.

[13] B. Mouliprasanth, P. Hariharan, Russ. J. Electrochem.57 (2021) 197–213.

[14] V. Subburam, S. Ramesh, LI. Freitas, in Futuristic Trends in Intelligent Manufacturing: Optimization and Intelligence in Manufacturing, K. Palani Kumar, E. Natarajan, R. Sengottuvelu, J.P. Davim, Springer, (2021), p.33–46.

[15] M. Soundarrajan, R. Thanigaivelan, S. Maniraj, in Advances in Industrial Automation and Smart Manufacturing, A. Arockiarajan, M. Duraiselvam, R. Raju (eds), Springer, (2021), p. 367–376.

[16] C. Guo, B. Wu, B. Xu, S. Wu, J. Shen, X. Wu, J. Electrochem. Soc.168 (2021) 071502.

[17] S. Ao, K. Li, W. Liu, X. Qin, T. Wang, Y. Dai, Z. Luo, J. Manuf.Process. 53 (2020) 223–228.

[18] J.R. Vinod Kumaar, R. Thanigaivelan, Mater. Manuf. Processes.35 (2020) 969–977.

[19] M. Soundarrajan, R. Thanigaivelan, Russ. J. Appl. Chem. 91 (2018) 1805–1813.

[20] X.Chen, N. Qu, Z. Hou, Int. J. Adv. Manuf. Technol. 88 (2017) 565–574.

[21] E. Rajkeerthi, P. Hariharan, N. Pradeep, Mater. Manuf. Process. 36 (2021) 488–500.

[22] J.R. Vinod Kumaar, R. Thanigaivelan, V. Dharmalingam, in Advances in Micro and Nano Manufacturing and Surface Engineering, M. Shunmugam, M. Kanthababu (eds),

Springer, (2019), p. 93–103.

[23] K. Wang, Y. Wang, Q. Shen, Int. J. Electrochem. Sci. 15 (2020) 5430–5439.

[24] S. Kunar, S. Mahata, B. Bhattacharyya, J. Micromanuf. 1 (2018) 124–133.

[25] S.S. Anasane, B. Bhattacharyya, Advanced Manufacturing-I, in Proceeding of the AIMTDR 2014, IIT Guwahati, India (2014) p. 1–6.

[26] B. Amipara, A.D. Galgale, N.G. Shah, Asian J. Water, Environ. Pollut. 18 (2021) 59–65.

[27] A.F. Alkaim, T.A. Kandiel, R. Dillert, D.W. Bahnemann, Environ. Technol. 37 (2016) 2687–2693.

[28] C.W. Cho, T.P.T. Pham, Y. Zhao, S. Stolte, Y.S. Yun, Sci. Total Environ.786 (2021) 147309.

[29] Q.Y. Chen, J.S. Liu, Y. Liu, Y.H. Wang, J. Power Sources 238 (2013) 345–349.

[30] J. Navisa, T. Sravya, M. Swetha, M. Venkatesan,Asian J. Sci. Res.7 (2014) 482–487.

[31] K. Tangphant, K. Sudaprasert, S. Channarong, Russ. J. Electrochem. 50 (2014) 253–259.

[32] D.Deconinck, S. Van Damme, J. Deconinck, Electrochim. Acta 69 (2012) 120–127.

[33] B.M. Kolakowski, Z. Mester, Analyst 132 (2007) 842–864.

JEEVARATHNAM RAVI KUMAR VINOD KUMAAR[1]

RAJASEKARAN THANIGAIVELAN[2]

MADESH SOUNDARRAJAN[2]

[1]Department of Mechanical Engineering, Mahendra Engineering College, Mahendhirapuri, Namakkal, Tamil Nadu, India

[2]Department of Mechanical Engineering, Muthayammal Engineering College, Rasipuram, Namakkal, Tamil Nadu, India

NAUČNI RAD

UTICAJ RAZLIČITIH ELEKTROLITA NA ELEKTROHEMIJSKU MIKRO MAŠINSKU OBRADU SS 316L

Upotreba nerđajućeg čelika 316L (SS 316L) u medicinskom, pomorskom, vazduhoplovnom, biomedicinskom i automobilskom sektoru brzo raste. Elektrohemijska mikro-mašinska obrada (ECMM) je prikladna za obradu SS 316L zbog njegove površine za obradu bez ivica, bez zaostalog naprezanja i visoke preciznosti. Međutim, postoje neka ograničenja u korišćenju jakih elektrolita, kao što su HCl, H_2SO_4, KOH, $NaNO_3$ i NaCl, koji se navodno suočavaju sa poteškoćama u odlaganju u okolinu i problemima rukovanja. Stoga se ovaj rad bavi prevazilaženjem nedostataka koji se sreću u ECMM procesu kada se za obradu SS 316L koriste jaki elektroliti. Zbog toga se različiti organski elektroliti kao što su vinska kiselina ($C_4H_6O_6$), limunska kiselina ($C_6H_8O_7$) i kombinacija vinske i limunske kiseline (mešoviti elektrolit) smatraju se najboljim elektrolitima. Parametri procesa kao što su napon obrade, radni ciklus i koncentracija elektrolita uključeni su u određivanje performansi obrade. Performanse ECMM-a se procenjuju korišćenjem brzine uklanjanja materijala (MRR) i prekoračenja. Presecanje (overcut) uz vinsku kiselinu je 179% manje nego u slučaju mešanog elektrolita za kombinaciju uslova obrade 12 g/l, 11 V i 85%. S druge strane, mešani elektrolit pokazuje 114,2% veći MRR od elektrolita vinske kiseline za parametarske rastvore od 25%, 11 V i 20 g/l. Štaviše, limunska kiselina pokazuje drugi najmanji presek i veći MRR u svim aspektima performansi mašinske obrade. Studije emisionog skenirajućeg elektronskog mikroskopa (FESEM) se sprovode da bi se ostvario efekat elektrolita na površinu obrade.

Ključne reči: mikro-mašinska obrada, slabi elektroliti, elektrohemija, SS 316L, MRR, presek.

Journal of the
Association of Chemical Engineers of
Serbia, Belgrade, Serbia

Chemical Industry & Chemical Engineering Quarterly

CI&CEQ Vol. 28 Contents: Issues 1–4 YEAR 2022

No. 1

No. 2

No. 3

No. 4

Journal of the
Association of Chemical Engineers,
Belgrade, Serbia

Chemical Industry & Chemical Engineering Quarterly

CI&CEQ Vol. 28 Author Index YEAR 2022

Q

R

S

Š

T

V

X

Y